Cenozoic deformation of the Tarim Basin and surrounding ranges (Xinjiang, China): A regional overview

Amandine Laborde, Laurie Barrier, Martine Simoes, Haibing Li, Thomas Coudroy, Jerome van Der Woerd, P Tapponnier

Cenozoic deformation of the Tarim Basin and surrounding ranges (Xinjiang, China): A regional overview

A. Laborde[1], L. Barrier[1*], M. Simoes[1], H. Li[2], T. Coudroy[1,3], J. Van Der Woerd[4] and P. Tapponnier[1,5]

[1]Université de Paris, Institut de physique du globe de Paris, CNRS, F-75005 Paris, France.
[2]Institute of Geology, Chinese Academy of Geological Sciences, Beinjing, China.
[3]Now at Technosol, Ballainvilliers, France.
[4]Institut de Physique du Globe de Strasbourg - Université de Strasbourg, CNRS, UMR 7516, Strasbourg, France.
[5]Now at Institute of Crustal Dynamics, China Earthquake Administration, Beijing, China.
*Corresponding author: Laurie Barrier (barrier@ipgp.fr)

Abstract

With its central position between the Tibetan Plateau and the Tian Shan Range, the Tarim Basin is a key element of the Cenozoic Asian orogenic system. However, a comprehensive regional study, and more particularly the quantification of shortening through this basin and its margins, are still needed to understand its role in the Cenozoic deformation of Asia. From a compilation of previous works, together with an extensive dataset of satellite, field, seismic and well data, we provide a tectonic map of the Cenozoic structures and four balanced geological transects of the Tarim Basin and its surrounding ranges. Based on this map and these cross-sections, we characterize the Cenozoic deformation of the original Proterozoic Tarim block. From structural restorations and crustal budgets, we also quantify the compressive component of this deformation. Most of the Cenozoic compressive deformation (from ~94% to 100%) is concentrated in the ranges along the block margins. To the west, up to 78 ± 23 km and 54 +24/-18 km of crustal shortening are accommodated across the compressive Western Kunlun and Southwestern Tian Shan ranges, while to the east, up to 38.6 ± 18 km and 15 +20/-15 km are accommodated across the transpressive Altyn Tagh and Southeastern Tian Shan ranges. A non-

negligible amount of compressive deformation (up to ~6%) is also accommodated within the Tarim Basin by large basement-cored uplifts with a vergence synthetic to the deformation of the Tibetan Plateau edge. To the west, the Bachu uplift absorbs ~5 km of the total crustal shortening of the Western Kunlun thrust system, while to the south, the Tanan uplift accumulates ~0.6 km of the Altyn Tagh strike-slip system. Structural inheritance has a major influence on the Cenozoic deformation since ~33.3% to 100% of the total shortening is accommodated by reactivated basement structures inherited from the Protero-Paleozoic history of the Tarim block. Finally, we argue that the basement-cored uplifts in the centre of the basin imply a deformation transfer from the Tibetan Plateau to the Tian Shan, above a deep crustal decollement decoupling the deforming crust from an underlying rigid mantle.

Keywords

Asian Cenozoic deformation, Tarim Basin, Western Kunlun, Altyn Tagh, Tian Shan, shortening, balanced geological cross-sections

1. Introduction

With the Himalaya-Tibetan Plateau orogenic system and active deformation as far as 3000 km north of the India-Asia collision zone (including the Tian Shan, Altai Range and Baikal rift system) (Fig. 1), Asia is an outstanding natural laboratory to study continental deformation. Following the pioneering studies of the late 1970s and early 1980s (e.g., Molnar and Tapponnier, 1975, 1977; Tapponnier and Molnar, 1979; Molnar, 1984; England and Houseman, 1985), multiple investigations on the Cenozoic Asian mountain ranges, but also on the associated sedimentary basins, which are key recorders of their tectonic and climatic evolution, have been conducted to decipher the modalities of this deformation (e.g., Avouac et al., 1993; Matte et al., 1996; Métivier et al., 1998; Lavé and Avouac, 2001; Tapponnier et al., 2001; Yang and Liu, 2002; Yin et al., 2002; Guillot et al., 2003; Clark et al., 2006; DeCelles et al., 2007; Liu-Zeng et al., 2008; Charreau et al., 2009; Lu et al., 2010; Cheng et al., 2015, 2016a; Coutand et al., 2016; Gourbet et al., 2017; Jolivet et al., 2018). Among these basins, the Tarim Basin occupies a remarkable central position within the orogenic system, between the Tibetan Plateau and the

Tian Shan Range (Fig. 1). With a continuous Proterozoic to Present sedimentation, this wide basin is thus a first-class repository for the geological history of the Asian continent (e.g., Li et al., 1996; Métivier et al., 1999; Yin et al., 2002; Kent-Corson et al., 2009; Sun et al., 2009b; Lin et al., 2012c; Bosboom et al., 2014a; Tang et al., 2014; Lin et al., 2015a; Liu et al., 2015a; He et al., 2016; Zhu et al., 2017; Morin et al., 2018; Wu et al., 2018; Jiang et al., 2018). Furthermore, the Tarim Basin seems to be a key element in the Cenozoic Asian deformation. Indeed, it is usually considered as an undeformed rigid block, playing the role of an heterogeneity in the strain field and/or of a secondary indenter that transmits the compressive stresses at the continental scale far to the north of the India-Asia collision zone (e.g., England and Houseman, 1985; Avouac and Tapponnier 1993; Neil and Houseman, 1997; Mattauer et al., 1999; Wang et al., 2007; Dayem et al., 2009; Craig et al., 2012; Calignano et al., 2015).

For these reasons, numerous studies have been performed on the Cenozoic deformation and sedimentation along the margins or within the centre of this basin (e.g., Avouac et al., 1993; Matte et al., 1996; Wittlinger et al., 1998, 2004; Allen et al., 1999; Burchfield et al., 1999; Yin et al., 2002; Scharer et al., 2004; Sun et al., 2005, 2009b; Heermance et al., 2007; Hubert-Ferrari et al., 2007; Fu et al., 2010; Turner et al., 2010; Li et al., 2012a; Jiang et al., 2013; Wei et al., 2013; Chang et al., 2014a; Cheng et al., 2016b; Li et al., 2016b; Li et al., 2016e; Lu et al., 2016; Wang and Wang, 2016; Guilbaud et al., 2017; Thompson et al., 2017; Izquierdo-Llavall et al., 2018; Jiang et al., 2018). However, they were mainly undertaken to characterize tectonic structures and their activity at a local scale. Moreover, the few studies conducted at a regional scale remain schematic or imprecise in terms of hierarchy and relationships between the structures, with sometimes no detail about which ones were activated or not during the Cenozoic (e.g., Wei et al., 2013; Tang et al., 2014; Lin et al., 2015a; Li et al., 2016e; Jiang et al., 2018). Nevertheless, it is clear that the original Proterozoic Tarim block is not totally rigid, with deformation along the margins and even in the center of the Tarim Basin (e.g., Avouac et al., 1993; Matte et al., 1996; Allen et al., 1999; Wittlinger et al., 2004; Guo et al., 2005; Heermance et al., 2007; Li et al., 2012a; Tong et al., 2012; Chang et al., 2014a; Tang et al., 2014; Fig. 15 of Wang et al., 2014a; Li et al., 2016e; Daout et al., 2018; Izquierdo-Llavall et al., 2018; Jiang et al., 2018). Yet, the amount and distribution of this deformation, as well as the type of structures accommodating it, still need to be precisely documented. A comprehensive regional study, and more particularly the quantification of shortening through this area, is therefore necessary to further discuss these

issues, and to understand how the Tarim participates to the propagation of the Cenozoic compressive deformation within Asia.

In this article, we present such a comprehensive study of the Cenozoic deformation at the scale of the whole Tarim Basin and its surrounding ranges. Thanks to a compilation of existing geological maps and of published cross-sections, together with an extensive dataset of surface (satellite images and field constraints) and subsurface (seismic profiles and well data) data, we hereafter propose a tectonic map and four balanced geological transects highlighting the structures activated during the Cenozoic in the Tarim area. On the basis of this map and these transects, we characterize and quantify the Cenozoic deformation across the whole basin and its margins, as well as its relationships with the surrounding ranges.

2. Geological setting

2.1. Tarim Basin

The Tarim Basin is located in Central Asia, in the Xinjiang Province in China (Fig. 1). It corresponds to a ~1500-km-long and ~700-km-wide active sedimentary basin with an average elevation of ~1200 m (Fig. 1). Presently, this basin is an endorheic compressive basin surrounded by mountain ranges: the Western Kunlun Range to the southwest, the Altyn Tagh Range to the southeast, and the Tian Shan to the north.

This region of Central Asia was initially structured during the Proterozoic and Paleozoic by the accretion of several blocks: the Kunlun and Qaidam blocks to the south, the Tarim block in the centre, and the Central/South Tian Shan block to the north (e.g., Windley et al., 1990; Matte et al., 1996; Sobel and Arnaud, 1999; Zhou et al., 2001; Xiao et al., 2004, 2013; Charvet et al., 2011; Lin et al., 2013; Zhang et al., 2013a; Li et al., 2018a). Prior to this accretion, the tectonic evolution of the Tarim block was dominated by extension from Neoproterozoic to Ordovician (e.g., Li et al., 1996; Zhang et al., 2013a; Tang et al., 2014; Liu et al., 2015a; Wang et al., 2015; Dong et al., 2016; Zhu et al., 2017; Ren et al., 2018; Wu et al., 2018). Then, from Ordovician to Permian, compression generalized in the area due to the closures of oceanic domains, followed by collisions between (1) the Tarim and Kunlun blocks to the southwest (from Ordovician to Devonian), (2) the Tarim and Qaidam blocks to the southeast (from Silurian

to Devonian), and (3) the Tarim and Central/South Tian Shan blocks to the north (from Devonian to Permian) (e.g., Windley et al., 1990; Li et al., 1996; Matte et al., 1996; Sobel and Arnaud, 1999; Gehrels et al., 2003; Xiao et al., 2004, 2013; Charvet et al., 2011; Lin et al., 2012c; Lin et al., 2013; Zhang et al., 2013a; Tang et al., 2014; Alexeiev et al., 2015; Liu et al., 2015; Han et al., 2016; He et al., 2016; Li et al., 2018a). Driven by all these oceanic closures and subsequent collisions, Paleozoic ranges comprising ophiolitic sutures (Fig. 1), as well as plutonic and metamorphic rocks, formed around the Tarim block (e.g., Windley et al., 1990; Matte et al., 1996; Gao et al., 1998; Sobel and Arnaud, 1999; Cowgill et al., 2003; Gehrels et al., 2003; Xiao et al., 2005, 2013; Cowgill, 2010; Charvet et al., 2011; Glorie et al., 2011; Cao et al., 2013; Zhang et al., 2014a; Li et al., 2018a). In the contemporaneous Tarim Basin settled in the centre of the block, this Protero-Paleozoic history also induced the development of large structures known as the Bachu, Tanan, Tazhong, Tadong, Tabei, Kalpin, and Kuruk Tagh basement-cored uplifts, which were created in extension at the end of the Proterozoic-beginning of the Paleozoic, before being reactivated in compression (e.g., Li et al., 1996; Allen et al., 1999; Carroll et al., 2001; Turner et al., 2010; Lin et al., 2012b, 2012c; Zhang et al., 2013a; Gao and Fan, 2014; Tang et al., 2014; Lin et al., 2015a; Liu et al., 2015a; He et al., 2016; Zhu et al., 2017; Wu et al., 2018).

At the end of the Paleozoic, the emplacement of a Permian Large Igneous Province (LIP) affected the Tarim block (e.g., Zhang et al., 2008; Zhang et al., 2010; Zhang et al., 2012b; Yang et al., 2013; Li et al., 2014a; Xu et al., 2014; Yang et al., 2016; Loury et al., 2018). Afterwards, during the Mesozoic, other blocks (Qiangtang and Lhassa blocks) were accreted further south, in the palaeo-Tibetan Plateau region (e.g., Matte et al., 1996; Yin and Harrison, 2000; Pan et al., 2012; Jolivet, 2017; and references therein). Within the Tarim region, these events produced a complex zone of deformation, with minor strike-slip, compressive or extensive reactivations of the inherited Protero-Paleozoic structures (e.g., Hendrix et al., 1992; Li et al., 1996; Sobel, 1999, 2001; Dumitru et al., 2001; Arnaud et al., 2003; Chen et al., 2003; De Grave et al., 2007; Jolivet et al., 2010, 2013; Wang et al., 2012; Chang et al., 2014b; Tang et al., 2014; Li et al., 2015a; Morin et al., 2018; Yang et al., 2018b). Finally, during the Cenozoic, India collided into the Asian continent around 55-45 Ma (e.g., Wang et al., 2014a and references therein). This last collision led to a major compressive reactivation of the mountain ranges surrounding the Tarim block, as well as of inherited structures within the Tarim Basin (e.g., Molnar and Tapponnier, 1975; Tapponnier and Molnar, 1977, 1979; Windley et al., 1990; Avouac et al., 1993; Allen et

al., 1994; Hendrix et al., 1994; Matte et al., 1996; Jolivet et al., 1999, 2001, 2010; Dumitru et al., 2001; Yin et al., 2002; De Grave et al., 2007; Turner et al., 2010; Yin, 2010 and references therein; Tong et al., 2012; Tang et al., 2014; Li et al., 2015b and references therein; Li et al., 2016e; Jiang et al., 2018; Yang et al., 2018b). In this study, because these ranges involve parts of the block itself, we refer to the Tarim block as the area comprised in between the various Paleozoic ophiolitic sutures located in the mountain belts (Fig. 1), rather than as the present-day Tarim Basin only.

Resulting from this long geological history, the Tarim Basin stratigraphy is characterized by a Proterozoic basement composed by igneous rocks, overlain by a thick, more or less continuous series of sediments from Neoproterozoic (Sinian) to Quaternary (Fig. 2) (e.g., Li et al., 1996; Carroll et al., 2001; Yin et al., 2002; Guo et al., 2005; Wang et al., 2009; Shu et al., 2011; Lin et al., 2012a, 2012c; Zhang et al., 2013a; Tang et al., 2014; Guo et al., 2015; Lin et al., 2015a; Liu et al., 2015a; He et al., 2016; Li et al., 2016d; Zheng et al., 2015; Tian et al., 2016; Zhu et al., 2017; Wu et al., 2018). During the Sinian and Paleozoic, marine calcareous and terrigenous deposits were dominant until the Carboniferous (Fig. 2) (e.g., Carroll et al., 2001; Chen and Shi, 2003; Shu et al., 2011; Lin et al., 2012c; Zhang et al., 2013a; Gao and Fan, 2014; Li et al., 2015a; Liu et al., 2015a; He et al., 2016; Zhu et al., 2017; Wu et al., 2018). In the western part of the basin, the Paleozoic sediments also contain an upper Cambrian interval of gypsiferous shales (Fig. 2), which is a major decollement level in this area (e.g., Allen et al., 1999; Lin et al., 2012a, 2012c; Li et al., 2016c, 2016e; Lu et al., 2016; Yang et al., 2018b). Within the Neoprotero-Paleozoic series, field observations, seismic profiles and well data document unconformities, together with sedimentary thickness and facies changes at the top of the basement-cored structures in the Tarim. Combined with thermochronological data, this shows that these structures were already active during the early (Sinian to Devonian) stages of the basin evolution (e.g., Allen et al., 1999; Carroll et al., 2001; Dumitru et al., 2001; Chen and Shi, 2003; Tang et al., 2008; Turner et al., 2010, 2011; Chang et al., 2012b; Lin et al., 2012b, 2012c; Gao and Fan, 2014; Lin et al., 2015a; Liu et al., 2015a; He et al., 2016; Zhang et al., 2016; Zhu et al., 2017; WuJ et al., 2018).

During the Permian, a marine to continental transition occurred, with a change from calcareous to terrigenous deposits characterizing most of the Mesozoic sediments (Fig. 2) (e.g., Hendrix et al., 1992; Gao et al., 1998; Sobel, 999; Carroll et al., 2001; Chen and Shi, 2003; Guo

et al., 2015; Li et al., 2015a; Li et al., 2016d; Morin et al., 2018; Peng et al., 2018). A thick (up to ~10 km) and continuous Cenozoic sedimentary series, mainly supplied by the erosion of the surrounding mountain ranges, was then trapped in the contemporaneous compressive Tarim Basin (e.g., Yin et al., 1998, 2002; Métivier and Gaudemer, 1997; Heermance et al., 2007; Wang et al., 2009; Zheng et al., 2015; Tian et al., 2016). From the late Cretaceous to Eocene, the Tarim deposits were mostly continental and terrigenous, except in the western part of the basin where an alternation of marine transgressions/regressions occurred (e.g., Yin et al., 1998; Wei et al., 2013; Bosboom et al., 2014a, 2014b, 2017; Tian et al., 2016; Chen et al., 2018; Zhang et al., 2018; Kaya et al., 2019). In that area, the marine Paleocene-Eocene Kashgar Group is thus composed of gypsum, limestones, siltstones, and sandstones related to these marine incursions (Fig. 2) (e.g., Jin et al., 2003; Bosboom et al., 2011, 2014a, 2014b, 2017; Wei et al., 2013; Wang et al., 2014; Zheng et al., 2015; Zhang et al., 2018; Blayney et al., 2019). This Paleocene-Eocene evaporitic assemblage corresponds to another major decollement level in the southwest of the Tarim (Southwest depression) (e.g., Li et al., 2016e; Lu et al., 2016). At the end of the Eocene, the western marine deposits ended while a continental sedimentation finally developed throughout the basin (e.g., Yin et al., 1998, 2002; Jin et al., 2003; Bosboom et al., 2014a; Zheng et al., 2015; Tian et al., 2016; Zhang et al., 2018). During the Oligocene and early Miocene, the sediments mostly consist in claystones, siltstones, and sandstones (Fig. 2) (e.g., Yin et al., 1998, 2002; Jin et al., 2003; Heermance et al., 2007; Wang et al., 2009; Zheng et al., 2015; Tian et al., 2016; Blayney et al., 2019). In these series however, the lacustrine Eocene-Oligocene Kumugeliemu Group and Suweiyi Formation are made up of gypsum, siltstones, sandstones, and a few conglomerates (Fig. 2) (e.g., Yin et al., 1998; Huang et al., 2006; Wang et al., 2009; Tian et al., 2016). This Eocene-Oligocene evaporitic assemblage is also a major decollement level in the north of the basin (Kuqa depression) (e.g., Chen et al., 2004; Li et al., 2012a; Izquierdo-Llavall et al., 2018; Neng et al., 2018). From Miocene to Quaternary, the gravel content in the sediments progressively increased along the margins of the Tarim until the deposition of the conglomeratic Xiyu Formation, while sandstones and siltstones still deposited in the centre of the basin (Fig. 2) (e.g., Yin et al., 1998, 2002; Jin et al., 2003; Sun et al., 2005, 2009b, 2017; Heermance et al., 2007; Jin et al., 2008; Wang et al., 2009; Chang et al., 2012a; Thompson et al., 2015; Zheng et al., 2015; Tian et al., 2016). In compressive contexts, this kind of long-term coarsening-upward sequence is typically controlled by the growth and erosion of the mountain

ranges and their progressive thrusting over the adjacent basins (e.g., Puigdefabregas et al., 1986; Sinclair and Allen, 1992; Simoes and Avouac, 2006; Heermance et al., 2007; Charreau et al., 2009; Dubille and Lavé, 2015).

2.2. Western Kunlun Range

The Western Kunlun Range bounds the Tarim Basin to the southwest, between the towns of Kashgar and Hotan (Fig.1). It is a ~700-km-long, ~100-130-km-wide and up to ~7600-m-high mountain belt at the northwestern edge of the Tibetan Plateau. Nowadays, this mountain belt corresponds to a northeastward-vergent thrust wedge that developed between the Kongur Shan normal fault and the Karakax left-lateral fault to the west and south, and the Tarim Basin to the northeast (Fig.1) (e.g., Brunel et al., 1994; Matte et al., 1996; Wittlinger et al., 2004; Lu et al., 2016). From its overall orientation, this range can be subdivided into two parts: (1) a NNW-SSE-oriented part from Kashgar to Yecheng to the west, showing a structural and stratigraphic continuity with the northeastern Pamir, and (2) a WNW-ESE-oriented part from Yecheng to Hotan to the east.

Within this mountain belt, the southwestern boundary of the Tarim block is marked by the Oytag-Kudi suture (in red in Fig.1) related to the closure of the Proto-Tethys Ocean and to the associated Paleozoic orogeny spanning from Ordovician to Devonian (e.g., Matte et al., 1996; Mattern and Schneider, 2000; Xiao et al., 2005; Li et al., 2018a). During the Mesozoic, a complex strike-slip to compressive history then followed this orogeny (e.g., Sobel, 1999; Arnaud et al., 2003; Cao et al., 2015). Finally, a major reactivation of the Western Kunlun Range occurred during the Cenozoic in response to the India–Asia collision (e.g., Tapponnier and Molnar, 1977; Matte et al., 1996; Sobel and Dumitru, 1997; Yin et al., 2002; Cao et al., 2015). Based on thermochronological data (e.g., Sobel et al., 1997; Cao et al., 2013, 2015; Cheng et al., 2017; Blayney et al., 2016; Yang et al., 2018a), sediment provenance and growth strata (e.g., Yin et al., 2002; Bershaw et al., 2012; Jiang et al., 2013; Cao et al., 2014; Thompson et al., 2015; Cheng et al., 2016b, 2017; Blayney et al., 2016; Sun et al., 2016b), as well as increasing sediment accommodation and accumulation rates in the southwestern Tarim Basin (Métivier and Gaudemer, 1997; Metivier et al., 1999; Yang and Liu, 2002; Jiang and Li, 2014; Blayney et al., 2019), this reactivation seems to initiate by Eocene with subsequent Oligocene to Miocene

accelerations. The present thrust wedge then formed above an intra-crustal decollement level that progressively shallows from the south to the north. Indeed, the interior of the mountain range results from the imbrication and exhumation of Protero-Paleozoic basement and Paleozoic cover, whereas the foothills are characterized by a fold-and-thrust belt of Paleozoic, Mesozoic and Cenozoic sediments (e.g., XBGMR, 1976, 1985; Brunel et al., 1994; Matte et al., 1996; Wittlinger et al., 2004; Li et al., 2012b, 2016b; Jiang et al., 2013; Cheng et al., 2016b; Wang and Wang, 2016; Lu et al., 2016; Guilbaud et al., 2017; Thompson et al., 2017).

The basement of the Western Kunlun is thus composed of Proterozoic to Paleozoic (Ordovician to Silurian) plutonic and metamorphic rocks that recorded the lower Paleozoic orogeny of the range (e.g., Matte et al., 1996; Mattern and Schneider, 2000; Cowgill et al., 2003; Cowgill, 2010; Cao et al., 2013), while within the Tarim Basin, the contemporaneous sedimentary series have not endured such plutonic and metamorphic events (see section 2.1) (Fig. 2). Over this basement, the Western Kunlun Paleozoic cover consists in Devonian continental conglomerates coming from the erosion of the Paleozoic mountain belt, followed by Carboniferous marine limestones (Fig. 2) (e.g., Matte et al., 1996; Mattern and Schneider, 2000; Cowgill, 2010; Cao et al., 2013). Within the foothills of the range, the stratigraphy above these units then corresponds to a Permian to Cenozoic, mostly continental and terrigenous sedimentary series, containing an upper Cretaceous-Paleogene marine interval of terrigenous, calcareous, and evaporitic deposits (Fig. 2) (e.g., Matte et al., 1996; Sobel, 1999; Yin et al., 2002; Jin et al., 2003; Sun and Jiang, 2013; Bosboom et al., 2014a, 2014b, 2017; Guo et al., 2015; Zheng et al., 2015; Chen et al., 2018). Although coarser-grained, this series is similar to the contemporaneous sediments deposited at the front of the Western Kunlun Range, along the southwestern Tarim Basin margin.

2.3. Altyn Tagh Range

The Altyn Tagh Range bounds the Tarim Basin to the southeast, from the west of Minfeng to the east of Dunhuang (Fig. 1). It is a ~1500-km-long, ~40-80-km-wide and up to ~6200-m-high, WSW-ENE oriented mountain belt at the centre of the Tibetan Plateau northern edge. Presently, this mountain range corresponds to a northwestward-vergent strike-slip wedge that developed between the Altyn Tagh left-lateral fault to the southeast and the Tarim Basin to

the northwest (Fig. 1) (e.g., Wittlinger et al., 1998; Cowgill et al., 2000; Li et al., 2002a; Yin et al., 2002; Tang et al., 2014; Lin et al., 2015b; Zhao et al., 2016).

In this mountain belt, the southeastern boundary of the Tarim block is marked by the Lapeiquan-Hongliugou suture (in red in Fig. 1) related to the closure of the Proto-Tethys Ocean and to the associated Paleozoic orogeny spanning from Silurian to Devonian (e.g., Sobel and Arnaud, 1999; Gehrels et al., 2003; Li et al., 2018a). After a complex deformation history during the Mesozoic (e.g., Sobel, 2001; Chen et al., 2003; Robinson et al., 2003; Liu et al., 2007), the Altyn Tagh Range was then reactivated during the Cenozoic due to the India–Asia collision (e.g., Tapponnier and Molnar, 1977; Yin et al., 2002; Jolivet et al., 2001; Yin, 2010). Based on thermochronological data (e.g., Jolivet et al., 1999, 2001; Sobel, 2001; Yin et al., 2002; Liu et al., 2003, 2007; Ritts et al., 2008), sediment provenance (e.g., Yue et al., 2001; Yin et al., 2002; Sun et al., 2005; Wu et al., 2012; Li et al., 2014b; Lin et al., 2015b; Lu et al., 2014; Cheng et al., 2015, 2016a), growth strata (e.g., Cheng et al., 2015, 2016a; Zhao et al., 2016), and accumulation rates (e.g., Métivier et al., 1998; Sun et al., 2005; Lu et al., 2014), this reactivation seems to initiate by Eocene with subsequent Oligocene to Miocene accelerations. The present strike-slip wedge then formed, presumably, above a deep intra-crustal decollement level. Indeed, the range interior results from the imbrication and exhumation of Protero-Paleozoic basement and Paleo-Mesozoic cover, while in the foothills, compressive structures involve the same basement and cover units overlain by Cenozoic sediments (e.g., XBGMR, 1976, 1985; Jolivet et al., 1999; Chen et al., 2003; Liu et al., 2007; Tang et al., 2014; Lin et al., 2015b).

The basement of the Altyn Tagh is thus composed of Proterozoic to Paleozoic (Silurian to Devonian) plutonic and metamorphic rocks that recorded the middle Paleozoic orogeny of this mountain belt (e.g., Sobel and Arnaud, 1999; Cowgill et al., 2003; Gehrels et al., 2003; Zhang et al., 2014a), whereas the contemporaneous Tarim sedimentary series have not endured such a metamorphic event (see section 2.1), similar to what is observed at the front of the Western Kunlun Range. Over this basement, the Altyn Tagh Paleo-Mesozoic cover consists in Carboniferous marine limestones and Jurassic continental and terrigenous deposits (e.g., Sobel and Arnaud, 1999; Chen et al., 2003). Within the foothills of the range, the stratigraphy above these units corresponds to a continental and terrigenous Cenozoic series in continuity with the contemporaneous sediments deposited in the Tarim Basin (e.g., Yin et al., 2002; Sun et al., 2005; Lu et al., 2014).

2.4. Southern Tian Shan

The Southern Tian Shan bounds the Tarim Basin to the north, between the towns of Kashgar and Dunhuang (Fig. 1). It is a ~2200-km-long, ~100-250-km-wide and up to ~7400-m-high mountain belt corresponding to the southern edge of the Tian Shan Range. From its overall orientation, this belt can be subdivided into two parts: (1) the WSW-ENE-oriented Southwestern Tian Shan from Kashgar to the east of Kuqa, and (2) the WNW-ESE-oriented Southeastern Tian Shan from the east of Kuqa to Dunhuang. Presently, the Southwestern Tian Shan consists in a southeastward-vergent thrust wedge developed between the Nikolaev Line and Narat Fault to the northwest and the Tarim Basin to the southeast (e.g., Poupinet et al., 2002; Heermance et al., 2008; Makarov et al., 2010; Xiao et al., 2013; Alexeiev et al., 2015; Izquierdo-Llavall et al., 2018), whereas the Southeastern Tian Shan corresponds to a southwestward-vergent strike-slip wedge developed between the right-lateral Baluntay Fault to the northeast and the Tarim Basin to the southwest (e.g., Allen et al., 1994; Charvet et al., 2011; Li et al., 2016a) (Fig. 1).

In these mountain belts, the northern boundary of the Tarim block is marked by the South Tian Shan suture (in red in Fig. 1) related to the closure of the South Tian Shan Ocean or back-arc basin and to the associated Paleozoic orogeny spanning from Devonian to Permian (e.g., Windley et al., 1990; Gao et al., 1998; Charvet et al., 2007, 2011; Glorie et al., 2011; Xiao et al., 2013; Alexeiev et al., 2015; Han et al., 2016). During the Mesozoic, a complex compressive to strike-slip history then followed this orogeny (e.g., Hendrix et al., 1992; Sobel, 1999; Dumitru et al., 2001; Wang et al., 2009; Jolivet et al., 2010, 2013; Glorie et al., 2011; Chang et al., 2012b; Li et al., 2015a; Morin et al., 2018; Yang et al., 2018b). Finally, a major reactivation of the Tian Shan occurred during the Cenozoic in response to the India–Asia collision (e.g., Tapponnier and Molnar, 1979; Windley et al., 1990; Avouac et al., 1993; Allen et al., 1994; Hendrix et al., 1994; De Grave et al., 2007; Dumitru et al., 2001; Jolivet et al., 2010). Based on thermochronological data (e.g., Hendrix et al., 1994; Sobel and Dumitru, 1997; Dumitru et al., 2001; Sobel et al., 2006; Jolivet et al., 2010; Glorie et al., 2011; Chang et al., 2012b; Yu et al., 2014; Jia et al., 2015), sediment provenance and growth strata (e.g., Yin et al., 1998; Heermance et al., 2007; Li et al., 2012a; Bande et al., 2017a; Izquierdo-Llavall et al., 2018; Thompson et al., 2018; Li et al., 2019), as well as increasing sediment accommodation and accumulation rates in the northern

342 Tarim Basin (e.g., Métivier and Gaudemer, 1997; Métivier et al., 1999; Yang and Liu, 2002;
343 Huang et al., 2006; Heermance et al., 2007; Zhang et al., 2014b; Li et al., 2019), this reactivation
344 seems to initiate by Oligocene with subsequent Miocene accelerations.

345 Following this reactivation, the Southwestern Tian Shan thrust wedge formed above an
346 intra-crustal decollement level that progressively shallows from the north to the south. The
347 interior of this range thus results from the imbrication and exhumation of Protero-Paleozoic
348 basement and Paleo-Mesozoic cover (e.g., XBGMR, 1976, 1985; Yin et al., 1998; Xiao et al.,
349 2013; Alexeiev et al., 2015; Jourdon et al., 2017; Loury et al., 2017). It also comprises a few
350 compressive intra-mountainous basins filled by Cenozoic sediments (e.g., XBGMR, 1976, 1985;
351 Xiao et al., 2013; Morin et al., 2019). The foothills of the Southwestern Tian Shan then present a
352 deformation style that strongly varies laterally. In the centre, near the town of Aksu, compressive
353 structures involving Proterozoic basement and Paleo-Cenozoic cover developed from a large
354 basement uplift (the Kalpin uplift) inherited from the Protero-Paleozoic history of the Tarim
355 block (e.g., XBGMR, 1976, 1985; Carroll et al., 2001; Turner et al., 2010). In contrast, to the
356 west and to the east, the foothills are characterized by fold-and-thrust belts (the Kashgar-Artux,
357 Kepingtage and Kuqa belts) involving Paleozoic, Mesozoic and Cenozoic sediments (e.g.,
358 XBGMR, 1976, 1985; Allen et al., 1999; Yin et al., 1998; Burchfield et al., 1999; He et al., 2005;
359 Heermance et al., 2008; Turner et al., 2010; Li et al., 2012a; Alexeiev et al., 2015; Li et al.,
360 2016d; Izquierdo-Llavall et al., 2018).

361 Further east, the Southeastern Tian Shan strike-slip wedge could have formed above an
362 intra-crustal or deeper decollement level. As in the Southwestern Tian Shan, the range interior
363 indeed results from the imbrication and exhumation of Protero-Paleozoic basement and Paleo-
364 Mesozoic cover, and it comprises a few compressive intra-mountainous basins filled by
365 Cenozoic sediments (e.g., XBGMR, 1976, 1985; Allen et al., 1994; Charvet et al., 2011; Li et al.,
366 2016a; Morin et al., 2019). The foothills then entirely correspond to compressive and strike-slip
367 structures involving Proterozoic basement and Paleo-Cenozoic cover, which derive from a large
368 inherited Protero-Paleozoic basement uplift of the Tarim (the Kuruk Tagh uplift) (e.g., XBGMR,
369 1976, 1985; Yin et al., 1998; Tang et al., 2008; Lin et al., 2012b).

370 The basement of the Southern Tian Shan interior is thus composed of Proterozoic and
371 Paleozoic (Silurian to Devonian) metamorphic and plutonic rocks that recorded the middle-upper
372 Paleozoic orogeny of the range (Fig. 2) (e.g., Gao et al., 1998; Charvet et al., 2007, 2011; Gao et

al., 2009; Ge et al., 2012; Xiao et al., 2013; Alexeiev et al., 2015). Over this basement, the Paleozoic cover consists in Silurian-Devonian to Permian marine limestones and continental to marine, volcano-sedimentary or terrigenous deposits (Fig. 2) (e.g., Gao et al., 1998; Charvet et al., 2011; Liu et al., 2013; Xiao et al., 2013; Alexeiev et al., 2015; Li et al., 2015a; Jourdon et al., 2017). Both the basement and cover units are intruded by Paleozoic (Devonian to Permian) plutons (Fig. 2) (e.g., Gao et al., 1998; Charvet et al., 2007, 2011; Gao et al., 2009; Glorie et al., 2011; Xiao et al., 2013; Alexeiev et al., 2015). However, in the foothills of the range as in the Tarim Basin, the coeval stratigraphy is characterized by a Proterozoic igneous basement below a thick, more or less continuous series of Sinian to Permian sediments that have not endured the Paleozoic orogeny (e.g., Carroll et al., 1995, 2001; Zhou et al., 2001; Tang et al., 2008; Turner et al., 2010; Shu et al., 2011; Li et al., 2015a; Cai et al., 2018; Wu et al., 2018). Above all these units, the Southern Tian Shan cover is composed of Triassic to Cenozoic, mostly continental and terrigenous sediments containing a Paleogene lacustrine interval of terrigenous and evaporitic deposits (Fig. 2) (e.g., Hendrix et al., 1992; Yin et al., 1998; Heermance et al., 2007; Tang et al., 2008; Wang et al., 2009; Li et al., 2015a; Li et al., 2016d; Tian et al., 2016; Izquierdo-Llavall et al., 2018; Morin et al., 2018). Although coarser-grained, this series is similar to the contemporaneous sediments deposited in the basin at the front of the range.

3. Data and method

3.1. Data

To characterize the Cenozoic deformation of the Tarim Basin, we have constructed a structural map and four balanced regional geological transects. To construct this map and these transects, we first synthesized the studies that were previously published in the area (Fig. 1). Indeed, numerous data and interpretations were already available such as (1) regional and local geological maps (e.g., XBGMR, 1976, 1985; Matte et al., 1996; Burchfield et al., 1999; He et al., 2005; Cowgill, 2010; Fu et al., 2010; Turner et al., 2010; Cao et al., 2013; Cheng et al., 2015; Wang and Wang, 2016; Guilbaud et al., 2017; Thompson et al., 2017), (2) geological cross-sections from field observations and seismic profiles (e.g., Fig. 1 and references therein), and (3) isopach and isobath maps (e.g., Lee, 1985; Li et al., 1996; Yang and Liu, 2002; Chen and Shi,

2003; Li et al., 2016e). Eventually, we also used the previous biostratigraphical and magnetostratigraphical studies in the region to constrain the ages of the sedimentary series (e.g., Yin et al., 1998, 2002; Sobel, 1999; Sun et al., 1999; Chen and Shi, 2003; Sun et al., 2005, 2009a, 2009b, 2016a, 2017; Charreau et al., 2006, 2009; Huang et al., 2006, 2010; Heermance et al., 2007; Wang et al., 2009; Chang et al., 2012a, 2014a; Bosboom et al., 2014a, 2014b, 2017; Lu et al., 2014; Zhang et al., 2014b; Zheng et al., 2015; Peng et al., 2018; Blayney et al., 2019).

In addition to these previously-published data, we used surface observations performed in the field and on satellite images (Landsat, Spot and DigitalGlobe images available through the Google Earth database), as well as on digital elevation models (SRTM30, SRTM3, SRTM1, ASTER GDEM v2, and AW3D30, with a horizontal resolution from ~900 to ~30 m) (e.g., Figs. 4 and 5). Thanks to the Sinopec Group of the China Petrochemical Corporation, we also had access to an extensive subsurface dataset comprising ~31120 km of regional and local seismic profiles covering the entire basin (Figs. 1 and S2), together with the data of 29 wells. In particular, Vertical Seismic Profiles (VSP) of P-waves were available for four of these boreholes (red dots in Fig. 1). From these VSP, seismic velocities can be deduced and a velocity model can be proposed (Fig. 3), in order to convert the travel time of seismic interpretations into depth (see section 3.4).

3.2. Seismic interpretation

To interpret our seismic dataset, we followed a standard procedure (Nester and Padgett, 1992). First, we identified the faults based on offsets of the seismic reflectors. Then, we picked seven horizons along the seismic profiles through the whole seismic grid covering the basin: the base of the (1) Sinian (i.e. the basement-sedimentary cover boundary in the Tarim Basin), (2) upper Cambrian (i.e. the base of the main Paleozoic decollement in the region), (3) Permian, (4) Paleocene, (5) Oligocene, (6) middle Miocene, and (7) Pliocene deposits (Fig. 2). The ages of the pre-Cenozoic horizons were mainly constrained by biostratigraphical dating on outcrops and cores (e.g., Sobel, 1999; Chen and Shi, 2003; Zhang et al., 2014b; Peng et al., 2018), as well as on samples collected in the boreholes of the Sinopec Group dataset. The ages of the Cenozoic horizons were determined on the basis of previous biostratigraphical and magnetostratigraphical studies mainly performed on outcrops. For this, we took advantage of sections sampled along

outcrops that can be correlated with the seismic data (Yin et al., 2002; Charreau et al., 2006, 2009; Huang et al., 2006, 2010; Peng et al., 2006; Sun et al., 2009a, 2009b, 2017; Wang et al., 2009; Bosboom et al., 2014a; Zheng et al., 2015; Blayney et al., 2019). These sections are located to the southwest, in the centre, and to the north of the basin (green dots in Fig. 1).

In order to ensure that our interpretation is consistent over the whole studied area, the selected seismic horizons were propagated from a seismic line to another through the entire seismic grid. The robustness of this horizon picking is confirmed by the fact that the position of our Cenozoic seismic horizons fall within a time interval of less than 0.5 Myr on the dated sections outcropping several 100s of km apart in different places of the basin.

3.3. Structural mapping

In order to highlight the structures activated during the Cenozoic, we constructed a georeferenced structural map of the Cenozoic deformation through the Tarim Basin and its surrounding ranges (Figs. 6 and S1). On this map, we reported the main faults and folds affecting the Cenozoic sedimentary series. We identified and located the outcropping structures from the available surface data (i.e. the field constraints, satellite images, digital elevation models, together with the previously-published geological maps and cross-sections) (e.g., Figs. 4 and 5). When it was possible, we also verified the occurrence and location of these structures on the seismic profiles. In addition, we identified and located the structures buried below the Cenozoic sediments from the available subsurface data (i.e. the previously-published and unpublished seismic profiles and wells) (e.g., Fig. S2). Finally, we reported the position of the outcropping and buried fault tips and fold axes on the map, using different line thicknesses according to the scale of the structures, and different colours according to their rooting depth (red for the basement, orange for the Paleozoic decollements and yellow for the Cenozoic ones) (Fig. 6).

3.4. Time-to-depth conversion

To build geological cross-sections through the basin, we needed to convert our seismic interpretations (in two-way-time) into geological geometries (in depth). For this, we used the VSP data from four boreholes distributed across the basin (red dots in Fig. 1) to establish

velocity models for three sediment packages: the Sinian-Paleozoic (Sinian to Carboniferous), Permian-Mesozoic (Permian to Cretaceous) and Cenozoic series (Fig. 3). Indeed, for these different packages, the variation of the interval velocities according to depth follows a similar trend in the four wells. For each series, we approximated this variation by a velocity function versus depth with two parts: (1) an upper part corresponding to a single linear regression of the velocity data (solid lines in Fig. 3), and (2) a lower part corresponding to a maximum velocity determined according to the main lithology of the sediment package (calcareous for the Sinian-Paleozoic deposits, terrigenous for the Permian-Mesozoic and Cenozoic series) (dashed lines in Fig. 3). By using this velocity model, we assumed that the three approximated velocity functions are uniform at the basin scale, i.e. we neglected the local velocity variations that can exist due to lateral lithological changes. The time-to-depth conversion based on these functions is therefore a first-order achievement, which seems to be acceptable for this study at the scale of the whole Tarim Basin. Indeed, the depths estimated for the selected horizons falls in the range of their depths assessed in previously-published structural interpretations (cross-sections, isobath and isopach maps where the horizon depths vary by a few kilometres) (e.g., Li et al., 1996; Chen and Shi, 2003; Tang et al., 2014; Li et al., 2016e; Lu et al., 2016; Wang and Wang, 2016; Izquierdo-Llavall et al., 2018; Jiang et al., 2018).

3.5. Geological transect construction

In addition to the structural map, we constructed four balanced geological transects through the basin and the outer parts of the ranges (Figs. 7, 8, 9, 10, and S3). We built these regional cross-sections following a standard method (e.g., Woodward et al., 1989). We chose their paths perpendicular to the Cenozoic structure direction, which may change along each section (Fig. 6). As much as possible, we also located them along seismic profiles to precisely constrain the deformation in the basin (Figs. 1 and S2). Where this was not possible (e.g., where the sections are not parallel to the seismic data such as in the centre of the basin for example), the deformation could however still be constrained using the seismic profiles crossing the transects in multiple locations. As for the structural map, we used the surface geology (e.g., Figs. 4 and 5) to build these transects where structures are cropping out, in particular through the ranges at the ends of the sections. We also used the available subsurface data to constrain the structures buried

below the Cenozoic sediments in the basin (e.g., Fig. S2). Finally, to balance our geological transects, we used the concepts of the typical area balancing approach (e.g., Hossack, 1979; Mitra and Namson, 1989), combined with a line-length balancing (e.g., Dahlstrom, 1969) for the Meso-Cenozoic stratigraphic boundary. The line-length and area balancing approaches refer to the basic assumption that the strata lengths and cross-sectional areas do not substantially change during deformation. The combination of these approaches allowed us to propose admissible and viable cross-sections over their whole length (Elliott, 1983), even where the details of the structural geometries are not well imaged on seismic profiles (e.g., inside the duplex structures to the south of transects A and B or to the north of transect C). This implies that the produced cross-sections are restorable.

3.6. Transect restoration

In order to quantify the total Cenozoic shortening accommodated within the basin and the outer parts of the ranges, we restored the proposed balanced geological transects at the beginning of the Cenozoic (Fig. 7). This restoration was thus mainly based on the length conservation of the Paleogene basal boundary, which pre-dates the Cenozoic deformation onset. Where this boundary is lost by erosion without any older stratigraphic horizon that may be used as another marker, we minimized the eroded length by closing the structures just above the present-day topography (e.g., see the dotted lines to the south of transects C and D or to the north of transect A). Moreover, where this boundary is missing in the stratigraphy (e.g., where the lower Tertiary is lacking due to no deposit or erosion at that time), the restoration was made at the base of the oldest Cenozoic sediments existing in the area (e.g., the Middle-Upper Miocene to the north of transect A or the Plio-Quaternary to the north of transects B and D). Therefore, by following those rules, the shortening amounts deduced from our structural restoration are minimum estimates. However, to avoid too much approximation, we only performed this restoration between the main bordering faults of the Cenozoic deposits, without including the range interiors where stratigraphic markers are lacking. Eventually, the fixed reference lines used for this work are located in the basin, at the turning points of the different transects (Figs. 1 and 7).

4. Overall Cenozoic deformation

The structural map and regional geological transects constructed to document the Cenozoic deformation through the Tarim area are presented in Figures 6 and 7. They illustrate the overall structure of the surrounding mountain ranges verging toward the basin, i.e. northward along the Tibetan Plateau edge to the south and southward along the Tian Shan to the north. These surrounding ranges correspond to well-developed thrust wedges to the west of the basin (Western Kunlun Range and Southwestern Tian Shan) and strike-slip wedges to the east (Altyn Tagh and Southeastern Tian Shan). They concentrate a large amount of deformation with thick-skinned structures involving a Protero-Paleozoic basement and Paleozoic sedimentary cover in their interiors, while their foothills are characterized by either thin- or thick-skinned structures involving a Protero-Paleozoic basement and/or Protero-Paleozoic, Mesozoic and Cenozoic sediments, respectively (Figs. 6 and 7).

In the case of the Western Kunlun and Southwestern Tian Shan compressive systems, these foothills are mainly formed of wide (10s of km) and long (100s of km) thin-skinned fold-and-thrust belts (Western Kunlun, Kashgar-Artux, Kepingtage, and Kuqa belts), except for the central part of the Southwestern Tian Shan where a thick-skinned belt locally occurs (Kalpin belt) (Figs. 6 and 7). Associated with these fold-and-thrust belts, which can accommodate a large amount of shortening (10s of km) and thickening, deep flexures (Southwest, North and Kuqa depressions) have developed in the basin with up to ~10 and ~9 km of Cenozoic sediments accumulated along the front of the Western Kunlun and Southwestern Tian Shan, respectively (Fig. 7A, 7B and 7C). In contrast, no fold-and-thrust belt and deep foreland flexure are associated with the Altyn Tagh and Southeastern Tian Shan transpressional systems (Figs. 7C and 7D). In their case, the foothills are narrow (a few 10s of km) and correspond to a few basement-involved structures accommodating a limited amount of shortening (a few kilometres at most). Along the front of these ranges, less than a few kilometres of Cenozoic sediments are usually trapped.

In addition to this deformation within the ranges, Cenozoic deformation also occurs within the Tarim. Wide (from ~50 to ~150 km) and long (100s of km) basement-cored uplifts are visible to the west (Bachu uplift) and south (Tanan uplift) of the basin (Figs. 6, 7B, and 7C). These basement-cored uplifts correspond to large pop-up structures bounded by conjugate thrust systems. They are clearly parallel to the ranges bordering the basin to the south (Fig. 6), with a

559 main vergence toward the north, i.e. synthetic to the deformation of the Tibetan Plateau edge.
560 Indeed, this vergence can be deduced from the observation of a compressive deformation
561 accumulated on their conjugate bounding thrust systems larger to the north than to the south.
562 Besides these basement-cored uplifts, other basement-involved structures (Tazhong, Tadong, and
563 Tabei uplifts) exist further north and east in the basin (Figs. 6, 7C and 7D). However, they
564 mainly deform the Protero-Paleozoic strata, with little evidence of a significant Cenozoic activity
565 on their bounding faults. At first order, the Cenozoic deformation of the original Proterozoic
566 Tarim block therefore mainly occurs along its edges and within its southwestern interior.
567
568 **5. Southwest deformation**
569
570 To the southwest of the Tarim Basin, the northeastward-vergent Western Kunlun thrust
571 system can be divided into four structural parts with, from the southwest to the northeast: (1) the
572 inner range from the Kongur Shan normal fault and Karakax left-lateral fault to the Main Pamir
573 thrust, Kashgar-Yecheng transfer system, and Tiklik thrust system, (2) the outer range from the
574 Main Pamir thrust, Kashgar-Yecheng transfer system and Tiklik thrust system to the Western
575 Kunlun frontal blind ramp, (3) the Mazar Tagh thrust sheet and Southwest depression from the
576 Western Kunlun frontal blind ramp to the Mazar Tagh emergent thrust ramps, and (4) the Bachu
577 uplift from the Selibuya-Mazar Tagh deep fault systems to the Aqia-Tumuxiuke thrust systems
578 (Figs. 6, 7A, 7B, 8A, 8B and 9).
579
580 *5.1. Western Kunlun inner range*
581
582 The inner range is several 10s to ~100 km wide, with typical elevations between ~2500
583 and ~5500 m. It is composed of exhumed imbricates of the Western Kunlun Protero-Paleozoic
584 (Sinian to Silurian) basement and Paleozoic (Devonian to Carboniferous) cover (see section 2.2).
585 In this system, the inner range is a continuous belt stretching from the Pamir to the west to the
586 Altyn Tagh to the east. There, its northern part ends in a large basement-involved anticline and
587 syncline to the southeast of Hotan (Fig. 6). Due to limited field access and subsurface data, its
588 detailed structure is poorly constrained, but connecting the major faults within the basement to a
589 deep basal decollement seems a reasonable hypothesis (Figs. 7A, 7B, 8A and 8B), as previously

proposed by Matte et al., 1996, Wittlinger et al., 2004 or Guilbaud et al., 2017. Towards the northeast, the range interior is separated from the outer range by the Main Pamir thrust to the northwest and by the Tiklik thrust system to the southeast, connected by the Kashgar-Yecheng transfer system along the eastern edge of the Pamir salient (Fig. 6). These emergent thrust and strike-slip zones also correspond to the main bordering faults of the southwestern Cenozoic series of the Tarim Basin.

5.2. Western Kunlun outer range

At the front of the inner range, the outer range is also several 10s to ~100 km wide, with typical elevations between ~1500 and ~2500 m. It consists in a fold-and-thrust belt that mainly developed below the Cenozoic sediments of the Tarim Basin (Figs. 6, 7A, 7B, 8A, 8B, S2A and S2B). This belt follows the range from the Pamir to the west to the southeast of Hotan to the east where it abruptly ends into a lateral thrust ramp (Fig. 6). Several cross-sections have already been proposed through this outer range with various and contradictory interpretations on its structure (e.g., Brunel et al., 1994; Matte et al., 1996; Li et al., 2012b, 2016b; Jiang et al., 2013; Wang et al., 2013; Wei et al., 2013; Tang et al., 2014; Cheng et al., 2016b, 2017; Lu et al., 2016; Wang and Wang, 2016; Wang et al., 2016a; Guilbaud et al., 2017; Thompson et al., 2017). From our surface and subsurface data, we derived a regionally-consistent structural model settling the issue of these interpretations (see Supplementary information S4 for further details and discussion). We concluded that the surface and subsurface data provide clear evidence for 10s-of-km-long, emergent or blind folded thrust slices made of the Western Kunlun Protero-Paleozoic (Sinian to Silurian) basement and its Paleo-Mesozoic (Devonian to Cretaceous) cover at the rear, whereas 10s- to 100s-of-km-long duplex structures developed within the Tarim Paleo-Mesozoic (Cambrian to Cretaceous) sedimentary cover at the front (Figs. 7A, 7B, 8A, 8B, S2A and S2B).

These structures imply a basal decollement level that progressively shallows from the southwest to the northeast. At the rear of the outer belt, the major thrusts necessarily root into a deep decollement within the basement since they exhumed basement units (Figs. 7A, 7B, 8A and 8B). This decollement probably connects with the one below the range interior as classically inferred or proposed for most compressional orogens (e.g., Muñoz, 1992; Burkhard and

621 Sommaruga; 1998, Lavé and Avouac, 2001). The northeastward change from the thick-skinned
622 thrust slices to the thin-skinned duplexes then requires the presence of a ramp connecting this
623 deep decollement to an intermediate one at the base of the deformed sedimentary cover (Figs.
624 7A, 7B, 8A, and 8B) (see also Matte et al., 1996; Wittlinger et al., 2004; Wang et al., 2013; Li et
625 al., 2016b, 2018b; Lu et al., 2016; Cheng et al., 2017; Guilbaud et al., 2017). According to our
626 regional seismic interpretation constraints by local borehole observations, this intermediate
627 decollement is located at a depth of about 10 to 13 km below sea level (b.s.l.), in the upper
628 Cambrian evaporitic assemblage of the Tarim sedimentary series (see also Wang et al., 2013;
629 Tang et al., 2014; Lu et al., 2016; Guilbaud et al., 2017). Remarkably, the stratigraphy of the
630 Paleozoic terrains is different on both sides of the ramp connecting the deep and intermediate
631 decollements (Figs. 7A, 7B, 8A and 8B). To the southwest, this stratigraphy is characteristic of
632 the Paleozoic Western Kunlun Range with Ordovician to Silurian metamorphic rocks covered by
633 Devonian to Permian deposits (see section 2.2), whereas to the northeast, it is typical of the
634 Paleozoic Tarim Basin with Cambrian to Permian sediments (see section 2.1) (Fig. 2). Therefore,
635 the deep ramp to the southwest of the outer range seems to be a major inherited Paleozoic
636 structure reactivated during the Cenozoic.

637 To the front of the outer belt, the formation of duplexes within the Tarim Paleo-Mesozoic
638 series requires the activation of a series of ramps connecting the intermediate decollement within
639 the upper Cambrian evaporitic assemblage to a shallower one (Figs. 7A, 7B, 8A and 8B).
640 According to the seismic profiles, together with field and well constraints, this shallow
641 decollement is located at a depth of about 6 to 9 km b.s.l. at the front of the duplexes, in the
642 Paleogene evaporitic assemblage at the base of the Cenozoic deposits (see also Li et al., 2012b,
643 2016b; Jiang et al., 2013; Wang et al., 2013; Tang et al., 2014; Cheng et al., 2017; Lu et al.,
644 2016; Wang and Wang, 2016; Guilbaud et al., 2017; Thompson et al., 2017). Below this
645 decollement, the stratigraphy of the Paleo-Mesozoic sedimentary cover seems to be the same
646 (Cambrian to Cretaceous deposits) across the ramps connecting the Paleozoic and Cenozoic
647 decollements. Therefore, these shallow ramps at the front of the outer range likely correspond to
648 structures created during the Cenozoic.

649 At the top of the blind basement-involved thrust slices and of duplexes of the outer belt,
650 the Cenozoic sedimentary series is folded into 10s-of-km-wide and up to ~180-km-long
651 anticlines and synclines (Figs. 6, 7A, 7B, 8A and 8B). Assuming an area conservation during

deformation to keep the cross-sections balanced, the geometry of the underlying duplexes can be reconstructed from the overall envelope of these folds, which is usually well visible on the seismic profiles (Fig. S2A and S2B). These structures are thus interpreted as a stack of several (from four to six) horses, comprised between a floor thrust within the Paleozoic decollement level and a roof thrust within the Cenozoic one (Figs. 7A, 7B, 8A and 8B). This duplex style is typical of the frontal deformation in the central part of the Western Kunlun outer range, such as for the Qimugen fold-thrust system, the Yecheng-Pishan anticline or the Pusikai anticline (see also Jiang et al., 2013; Wang et al., 2013; Wei et al., 2013; Tang et al., 2014; Li et al., 2016b; Lu et al., 2016; Wang and Wang, 2016; Guilbaud et al., 2017).

Near the lateral terminations of the belt, structures of the outer range vary slightly from this pattern. To the northwestern termination (Yingisar anticline and Wupoer fold-thrust system), duplexes are also described in the Paleo-Mesozoic cover, but they are associated with emergent ramps breaching their roof thrust or rooted in the Cenozoic decollement at their top (e.g., Li et al., 2012b, 2013; Thompson et al., 2015, 2017, 2018; Cheng et al., 2016b; Wang and Wang, 2016; Wang et al., 2016a). To the southeastern termination, the Hotan anticline corresponds to a ramp anticline involving the Western Kunlun basement thrusted over the Cenozoic decollement (e.g., Jiang et al., 2013; Cheng et al., 2017). In the centre of the fold, this thrust sheet is subsequently folded by a duplex structure that developed in the footwall of the basement ramp, within the Tarim Pre-Cenozoic sedimentary cover. However, in spite of these geometrical variations, the main structural features of the outer range are similar almost everywhere: (1) a deep ramp rooted in the basement to the south, at the transition between the Western Kunlun and Tarim Paleozoic domains, and (2) a duplex structure in the Paleo-Mesozoic Tarim sedimentary series to the north, with an emergent or blind leading shallow ramp. The only exception corresponds to the lateral ramp of the Aqike anticline at the eastern edge of the belt (Fig. 6). Indeed, this anticline corresponds to a basement-involved breached duplex with a tailing emergent ramp and no cover duplex at its front (Yang et al., 2009).

Although largely covered by the Cenozoic deposits coming from the Western Kunlun erosion, the duplexes of the outer belt localize the topographic front of the mountain range. They usually form smooth topographic features uplifted by several 100s of m above the present-day Tarim sedimentation level (Fig. 6). In the northwestern and southeastern ends of the range, this topographic front corresponds to emergent ramps, i.e. to an emergent deformation front.

However, along most of the range, the Western Kunlun frontal ramp is a blind structure since it corresponds either to the leading blind ramp of a duplex (Qimugen fold-thrust system, Yecheng-Pishan anticline or Pusikai anticline) or to the blind front of a ramp anticline (Hotan anticline) (Figs. 7A, 7B, 8A and 8B). This raises the question of how the shortening accumulated within the outer belt is accommodated and transferred upward to the Cenozoic sedimentary pile. In the NNW-SSE-oriented part of the range, at the level of the Qimugen fold-thrust system, there is no evidence of deformation, and thus of slip transfer, in the Cenozoic deposits of the foreland, which are still attached to the underlying series (Figs. 6, 7A, 8A and S2A). This implies the existence of a triangular zone at the front of this fold-thrust system, with a passive roof thrust at its top within the Cenozoic decollement. It means that the Cenozoic deposits are detached above the underlying duplex, and that their shortening is accommodated by an emergent backthrust at their base (see also Wang and Wang, 2016; Wei et al., 2013). In contrast, to the east, in the WNW-ESE-oriented part of the range, such passive roof duplexes cannot exist due to the basement-involved imbricates emerging at the rear of the outer belt, which render back slip into the Cenozoic decollement impossible (Figs. 7B and 8B). Moreover, there is evidence of deformation, and thus of slip transfer, within the Cenozoic deposits of the foreland, such as in the case of the Jiede anticline or of the Mazar Tagh emergent thrust ramps located in the Tarim Basin, to the north of the Western Kunlun topographic front (Figs. 6, S2B, 7B and 8B) (see for example Wang et al., 2013; Wei et al., 2013; Wang et al., 2014a; Li et al., 2016b; Lu et al., 2016; Guilbaud et al., 2017; Jiang et al., 2018). Accordingly, in the eastern part of the range, the shortening accumulated within the outer belt appears to be transferred toward the foreland rather than toward the hinterland, with the activation of the Cenozoic decollement within the basin.

5.3. Mazar Tagh thrust sheet and Southwest depression

The Mazar Tagh is a striking topographic feature of the western central part of the Tarim Basin corresponding to an up to ~5-km-wide and ~220-km-long single to multiple ridge, raising a few 100s of m above the sedimentation level of the basin (Figs. 5A, 5C and 5D). This ridge stretches ~150-200 km to the northeast of the Western Kunlun topographic mountain front, parallel to the eastern part of the range (Fig. 6). Several contradictory cross-sections have been proposed through the Mazar Tagh area (e.g., Wittlinger et al., 2004; Yang et al., 2007a; Pan et

al., 2010; Tong et al., 2012; Tang et al., 2014; Wang et al., 2014a; Yang et al., 2015; Guo et al., 2016; Li et al., 2016b; Li et al., 2016e; Lu et al., 2016; Guilbaud et al., 2017; Xie et al., 2017; Jiang et al., 2018). From our surface and subsurface data, we derived a regionally-coherent structural model in agreement with some of these previous studies (see Supplementary information S4 for further details and discussion).

According to our surface and subsurface dataset, this topographic high is clearly controlled by northeastward-vergent emergent thrust ramps synthetic to the Western Kunlun deformation and rooting at the base of the Cenozoic deposits (Figs. 5B, 5D, 5E, 7B, 8B, 9 and S2B) (see also Yang et al., 2007a; Pan et al., 2010; Tong et al., 2012; Tang et al., 2014; Wang et al., 2014a; Yang et al., 2015; Guo et al., 2016; Li et al., 2016b; Li et al., 2016e; Lu et al., 2016; Guilbaud et al., 2017; Xie et al., 2017; Jiang et al., 2018). Indeed, the Paleogene evaporitic assemblage acting as a major decollement level in the outer range extends northeastward into the Tarim, at least until the Mazar Tagh where it outcrops at the surface (Fig. 5D and 5E). This suggests that the slip transferred into this Cenozoic decollement at the front of the Yecheng-Pishan, Pusikai, and Hotan anticlines of the outer belt is released at the Mazar Tagh emergent thrust ramps, with erosion of the Cenozoic deposits of their hangingwalls. In agreement with some of the previous studies (Pan et al., 2010; Li et al., 2016e; Lu et al., 2016; Guilbaud et al., 2017; Li et al., 2018b), we thus argue that to the east of the central bend of the range, these ramps correspond to the present-day emergent deformation front located in the basin, ~150-200 km away from the topographic mountain front, with a large frontal thrust sheet without any major internal deformation.

From the surface and subsurface data, structures involving the Proterozoic basement and Protero-Paleozoic to Mesozoic (Sinian to Jurassic) cover of the Tarim Basin also exist below the shallow Mazar Tagh deformation (Figs. 5A, 5B, S2B, 7B, 8B and 9) (see also Yang et al., 2007a; Pan et al., 2010; Tong et al., 2012; Tang et al., 2014; Wang et al., 2014a; Guo et al., 2016; Li et al., 2016b; Li et al., 2016e; Lu et al., 2016; Guilbaud et al., 2017; Xie et al., 2017; Jiang et al., 2018). Despite a complex and sometimes poorly-imaged geometry, these structures appear as a series of fault-related anticlines, often with backthrusts, or of minor pop-ups associated with steep thrust ramps. Regardless of a certain degree of symmetry, their main vergence is clearly toward the southwest since the base of the Cenozoic series is systematically higher to the northeast than to the southwest of these structures (Figs. 7B, 8B, 9 and S2B) (see for example

745 Yang et al., 2007a; Pan et al., 2010; Tong et al., 2012; Wang et al., 2014a; Yang et al., 2015;
746 Guo et al., 2016; Li et al., 2016b, 2018b; Li et al., 2016e; Lu et al., 2016; Guilbaud et al., 2017;
747 Xie et al., 2017; Jiang et al., 2018). This unambiguously indicates an uplift of their northeastern
748 compartments due to a southwestward thrust movement on ramps antithetic to the Western
749 Kunlun deformation. At depth, the Mazar Tagh deep fault system needs to connect to a deep
750 decollement within the basement. At their tips, the Mazar Tagh emergent thrust ramps seem to
751 be correlated with south-facing steps in the Cenozoic decollement, indicating that the location of
752 these shallow ramps was probably controlled by the hangingwall uplift of the underlying deep
753 structures (Figs. 6, 7B, 8B, 9 and S2B).

754 To the west of the central bend of the range, the offset on these Mazar Tagh emergent
755 thrust ramps decreases so that these ramps progressively disappear westward, with no more
756 evidence of a wide thrust sheet or of any other deformation within the Cenozoic foreland
757 deposits (Figs. 7A, 8A and S2A). On the other hand, a thrust ramp is still visible in the seismic
758 profiles through the Proterozoic basement and Protero-Paleozoic to Mesozoic cover of the Tarim
759 Basin, in continuity with the WNW-ESE Mazar Tagh deep fault system (Figs. 6, 7A, 8A and
760 S2A). However, their Cenozoic activity remained limited as indicated by very smooth fault-
761 propagation folds at their tips without any offset of the overlying Cenozoic deposits.

762 In the Tarim Basin, the area extending from the outer range to the Mazar Tagh deep fault
763 system is known as the Southwest depression (Figs. 6, 7A and 7B). In this area, the Tarim
764 basement and sedimentary cover are tilted southward and the Cenozoic deposits thicken toward
765 the Western Kunlun Range to reach their maximum thickness at the front of the outer belt (Figs.
766 7A, 7B, 8A, 8B, S2A and S2B). This overall geometry of the southwestern Tarim is thus typical
767 of a flexural basin associated with the shortening and thickening accumulated in the Western
768 Kunlun thrust system. It corresponds to the region of maximal accommodation space in the
769 Tarim Basin with up to ~10 km of Cenozoic sediments trapped close to the cities of Kashgar and
770 Yecheng, i.e. where the Western Kunlun converge with the Tian Shan and at the front of the
771 central bend of the range, respectively. In this foreland system, the Western Kunlun outer belt
772 corresponds to the wedge-top depozone, while the area comprised between the front of this belt
773 and the Mazar Tagh deep fault system represents the foredeep (after the terminology of DeCelles
774 and Giles, 1996), with the specificity that the whole Cenozoic sediments of the foredeep have

been detached from the underlying series to form the Mazar Tagh thrust sheet to the east of the central bend of the mountain range.

5.4. Bachu uplift

To the north of the Tarim Southwest depression, the Bachu uplift is a ~150-km-wide and ~250-km-long basement-involved structure forming a structural high of the Proterozoic basement and Protero-Paleozoic to Mesozoic (Sinian to Triassic) sedimentary cover of the basin, below the Cenozoic sediments (Figs. 6, 7B, 9 and S2B). From its overall geometry documented by seismic profiles, together with field and well data, this basement-cored structure corresponds to a large pop-up bounded by two conjugate thrust fault systems necessarily rooted in a deep decollement within the basement below the Tarim. Bounding this basement high to the southwest, the Selibuya and Mazar Tagh deep fault systems are composed of a series of fault-related anticlines and small pop-ups associated with steep southwestward-vergent thrust ramps (Figs. 6, 7B, 9 and S2B) (see also Wang et al., 2014a; Yang et al., 2018b; Guo et al., 2016; Li et al., 2016e; Jiang et al., 2018). To the northeast, the Aqia and Tumuxiuke fault systems display large folds related to thrust ramps with a clear northeastward vergence and a hangingwall uplift of a few kilometres, which is larger than the one of the Selibuya and Mazar Tagh fault systems (Figs. 6, 7B, 9 and S2B) (see also Tong et al., 2012; Tang et al., 2014; Wang et al., 2014a; Guo et al., 2016; He et al., 2016; Li et al., 2016e; Jiang et al., 2018). Consequently, the main vergence of the Bachu pop-up appears to be toward the northeast, i.e. synthetic to the Western Kunlun deformation. In addition, this structure clearly developed parallel to the Western Kunlun Range, with a NNW-SSE orientation to the west changing to a WNW-ESE one to the east. To the southwest of the Bachu uplift, a thrust ramp also exists in lateral continuity with the WNW-ESE Mazar Tagh deep fault system (Figs. 6, 7A, 8A and S2A), but its Cenozoic activity remained limited compared to the one of the NNW-SSE Selibuya faults slightly further north (Tong et al., 2012; Li et al., 2016e; Yang et al., 2018b). Finally, there is no evidence of flexure associated with this large basement structure, neither at its front to the northeast, nor at its rear to the southeast.

In the western part of the Bachu uplift, a strong internal deformation occurs in between the bounding fault systems (Fig. 6). There, this large basement pop-up is relatively symmetric

with several internal conjugate steep thrusts rooted in the basement and emerging at the surface (Tong et al., 2012; Tang et al., 2014; Wang et al., 2014a; Li et al., 2016e; Jiang et al., 2018; Yang et al., 2018b). Some of these thrusts (Gudongshan Fault System) join the Mazar Tagh deep fault system in the central bend of the Bachu structure, where a relay zone occurs between several fault segments (Fig. 6). However, the internal deformation of the Bachu high tends to decrease eastward of its central bend, with only a few thrust ramps and their associated folds, as well as smooth undulations (Fig. 6). Concomitantly, the Bachu pop-up becomes more asymmetric and acquires the geometry of a large fault-propagation fold with a backlimb broken by the Mazar Tagh deep fault system (Tong et al., 2012; Guo et al., 2016; He et al., 2016; Li et al., 2016e). Finally, at the eastern termination of the Bachu uplift, the offset of the conjugate Tumuxiuke and Mazar Tagh deep faults rapidly decreases eastward, together with the associated basement-cored folding (Fig. 6).

Based on seismic profiles and well data, previous studies have demonstrated that the Bachu uplift is an inherited Protero-Paleozoic structure that was probably formed in extension before to be reactivated in compression during the early stages of the Tarim evolution (e.g., Carroll et al., 2001; Chen and Shi, 2003; Lin et al., 2012b, 2012c; Gao and Fan, 2014; Liu et al., 2015a; He et al., 2016; Wu et al., 2018). The restoration of this uplift at the beginning of the Cenozoic supports this former activity. Indeed, the compressional offsets accumulated by the Pre-Cenozoic deposits along the Bachu bounding and inner faults are not totally reset by this restoration (Fig. 7B). During the Cenozoic, these faults were again reactivated in compression. The Bachu uplift has then developed to the north of the foredeep represented by the Southwest depression, taking the place of the forebulge of the Western Kunlun foreland system (after the terminology of DeCelles and Giles, 1996). Indeed, initially at the surface at the beginning of the Cenozoic, as indicated by a major angular unconformity, the Cenozoic deposits then gradually onlapped and overlapped this reactivated uplift, which is now covered by a few 100s of m of Plio-Quaternary sediments (Figs. 7B and 9) (see also Tong et al., 2012; Tang et al., 2014; Wang et al., 2014a; He et al., 2016; Li et al., 2016e; Jiang et al., 2018).

5.5. Deformation amount

Along the two transects crossing the Western Kunlun thrust system, we quantified the shortening from the main faults bounding the southwestern Tarim Cenozoic series (i.e. from the Kashgar-Yecheng transfer system and Tiklik thrust system at the rear of the outer range) to the front of the Western Kunlun compressive system (i.e. to the front of the Bachu uplift) (see Figs. 6, 7A and 7B for the fixed reference lines set at the turning points in the centre of sections A and B). Accordingly, the shortening values and proportions given below do not account for the deformation accommodated within the inner range. In its outer range and foreland only, the Western Kunlun thrust wedge accommodates a large amount of Cenozoic compressive deformation, with a total shortening of ~32 and ~35 km measured west and east of the central bend of the system, respectively (Fig. 7A and 7B). These shortening estimates are in the range of the other values published from previous cross-section restorations of the outer range, which are comprised between 24.6 and 54 km (Jiang et al., 2013; Cheng et al., 2016b, 2017).

To the west, in the NNW-SSE oriented part of the range (transect A), most of the measured shortening concentrates in the outer range, with ~31,5 km (~98.4% of the ~32 km of total shortening) accommodated within the outer belt and ~0.5 km (~1.6%) within the basin. In the outer belt, ~9.5 km (~29.7% of the ~32 km of total shortening) are accommodated by the basement-involved thrust slices and ~22 km (~68.7%) by the cover duplex. Compared to these values, the shortening of ~0.5 km (~1.6%) accommodated within the basin on the Mazar Tagh deep fault system is almost negligible. However, it should be noted that our section A was built through the western end of the Tarim Basin to cross perpendicularly the various structures intersected from the Western Kunlun to the Tian Shan. Built perpendicularly to the Western Kunlun Range only, it would have crossed the western part of the Bachu uplift where a few additional kilometres of shortening seem to have been accommodated (e.g., Tong et al., 2012; Tang et al., 2014; Li et al., 2016e; Jiang et al., 2018; Yang et al., 2018b).

To the east, in the WNW-ESE oriented part of the range (transect B), the shortening is distributed between the outer range and the Bachu uplift, with ~30 km (~85.7% of the ~35 km of total shortening) accommodated within the outer belt and ~5 km (~14.3%) within the basin. In the outer belt, ~16.5 km (~47.1% of the ~35 km of total shortening) are accommodated by the basement-involved thrust slices and ~13.5 km (38.6%) by the cover duplex. Consequently, these ~13.5 km of shortening had to be transferred to the Mazar Tagh emergent thrust ramps through the shallow Cenozoic decollement. Across the Bachu uplift, ~2 km (~5.7% of the ~35 km of total

867 shortening) are accommodated by the Mazar Tagh deep fault system and ~3 km (~8.6%) by the
868 Tumuxiuke thrust system. The resulting ~5 km of shortening accommodated by the whole Bachu
869 uplift is thus in agreement with the values of a few kilometres published earlier (Li et al., 2016e).
870 According to these estimates, the shortening accumulated in the Western Kunlun thrust
871 wedge outward from the inner range is of the same order of magnitude to the west and to the east
872 of the central bend of the mountain belt. The structure and high topography of the range interior,
873 together with the large flexure of the Southwest depression, indicate that a large amount of
874 shortening must also be accommodated by the internal part of the system. However, in the
875 absence of stratigraphic markers, it was not possible to restore and quantify this shortening from
876 the geological transects.
877 In addition, previous investigations demonstrated that a significant amount of strike-slip
878 movements is accommodated on major strike-slip fault systems in the range, such as the Karakax
879 fault or the Kashgar-Yecheng transfer system (Ding et al., 2004; Cowgill, 2010). Strike-slip
880 motion could also have occurred in the basin, for example in the western part of the Bachu uplift
881 or along the Mazar Tagh deep fault system where very steep faults and relatively symmetric
882 structures exist. However, our 2D restoration does not allow for quantifying such a deformation
883 that takes place outside of the planes of our sections.
884
885 **6. Southeast deformation**
886
887 To the southeast of the Tarim Basin, the northwestward-vergent Altyn Tagh strike-slip
888 system can be divided into three structural parts with, from the southeast to the northwest: (1) the
889 inner range from the left-lateral Altyn Tagh fault to the Tam Karaul and Northern Altyn Tagh
890 thrusts, (2) the outer range and Southeast depression from the Tam Karaul and Northern Altyn
891 Tagh thrusts to the front of the Minfeng, Ruoqiang, and Dunhuang fault systems, and (3) the
892 Tanan uplift (Figs 6, 7C, 7D, 8C, 8D, S2C and S2D).
893
894 *6.1. Altyn Tagh inner range*
895
896 The inner range is several 10s to ~100 km wide, with typical elevations between ~2500
897 and ~5500 m. It is composed of exhumed imbricates of the Altyn Tagh Protero-Paleozoic (Sinian

to Silurian-Devonian) basement and Paleo-Mesozoic (Carboniferous and Jurassic) cover (see section 2.3). However, this inner range is discontinuous and only developed to the southwest and in the centre of the Altyn Tagh system (Fig. 6). Indeed, except to the southwest where it is in continuity with the southeastern part of the Western Kunlun interior, the Altyn Tagh inner range disappears where its frontal thrusts (the Tam Karaul and Northern Altyn Tagh thrusts) laterally join and merge into the major left-lateral Altyn Tagh fault at the rear. This fault organization pattern is typical of transpressive wedges. As for the Western Kunlun Range, the detailed structure of the Altyn Tagh inner range is poorly constrained, but connecting the major faults to a deep basal decollement within the basement seems a reasonable hypothesis (see also Wittlinger et al., 1998 and Tang et al., 2014). To the northwest, the range interior is separated from the outer range by the Tam Karaul and Northern Altyn Tagh emergent thrusts (Fig. 6). With the Altyn Tagh fault, these thrusts correspond to the main bordering faults of the southeastern Cenozoic series of the Tarim Basin.

6.2. Altyn Tagh outer range and Southeast depression

At the front of the inner range, the outer range is several 10s to ~60 km wide, with typical elevations between ~1500 and ~2500 m. To our knowledge, no specific cross-section has ever been proposed so far for this outer range. However, contrary to the Western Kunlun compressive system bordering the Tarim Basin to the southwest, the Altyn Tagh transpressive system does not have any fold-and-thrust belt in its outer part. According to the surface and subsurface data, the outer range is mainly composed of several-10s-of-km-long basement-involved structures made of the Altyn Tagh Protero-Paleozoic basement and its Paleo-Mesozoic to Cenozoic (Carboniferous to Quaternary) cover (Figs. 7C, 7D, 8C, 8D, S2C and S2D). These structures are related to northwestward-vergent, blind or emergent thrust ramps forming the Minfeng, Ruoqiang and Dunhuang fault systems. These ramps necessarily root into a deep decollement within the basement, which is probably in continuity with the one below the inner range.

With no sediments older than the Carboniferous (see also XBGMR, 1985; Li et al., 1996; Tang et al., 2014; He et al., 2016), the Paleozoic stratigraphy of the outer belt is similar to the one of the inner range (e.g., Sobel and Arnaud, 1999; Chen et al., 2003). In the outer range, unconformities are also frequent in the Paleo-Mesozoic strata or at the base of the Cenozoic

deposits in the hanging wall of the thrust ramps (Figs. 7C, 8C and S2C) (see also XBGMR, 1985; Li et al., 1996; Tang et al., 2014; He et al., 2016). Moreover, the restoration of the section at the beginning of the Cenozoic does not totally reset the compressional offsets accumulated by the older sediments along these faults (Fig. 7C). All this implies that the latter are inherited structures reactivated during the Cenozoic. In the Altyn Tagh outer range, the whole Cenozoic deformation is associated with these inherited faults since there is no evidence of younger structures rooted in a decollement level in the Paleozoic or Cenozoic sedimentary series.

Associated with these reactivated thrusts, the Paleo-Mesozoic and Cenozoic sediments are gently folded into 10s-of-km-wide and up to 100s-of-km-long anticlines and synclines. To the southwest, the Cenozoic deposits related to the erosion of the Altyn Tagh cover these folds and the topographic mountain front is located behind, at the front of the inner range. To the northeast, they form smooth topographies uplifted several 100s of m above the present-day Tarim sedimentation level and localize the topographic mountain front.

In the Tarim Basin, the area at the front of these folds is known as the Southeast depression (Figs. 6, 7C, and 7D). In this area, the Tarim basement and sedimentary cover are gently tilted southeastward, with the Cenozoic deposits slightly thicker at the front of the Altyn Tagh outer belt than further northwest in the basin (Figs. 7C, 7D, 8C, 8D, S2C and S2D). This overall geometry of the southeast Tarim thus indicates a slight flexure associated with the shortening and thickening accumulated in the Altyn Tagh strike-slip system. However, with ~3 km of trapped Cenozoic sediments at most, the generated accommodation space remains moderate. This suggests a limited compressive deformation accommodated across the Altyn Tagh Range, which is somehow expected when compared to a thrust wedge such as the Western Kunlun Range for example. Moreover, the southwestern part of the Altyn Tagh foredeep is broken by the Tanan basement uplift, which probably explains the limited accommodation space in this foreland (Strecker et al., 2012).

6.3. Tanan uplift

To the north of the Tarim Southeast depression, the Tanan uplift (also known as the Qiemo uplift) is a ~50-km-wide and ~600-km-long basement-involved structure forming a structural high of Proterozoic basement and Paleo-Mesozoic (Carboniferous to Cretaceous)

cover, below the Cenozoic sediments of the basin (Figs. 6, 7C, 8C and S2C) (see also Lin et al., 2012b, 2012c; Tang et al., 2014; Li et al., 2015c; Liu et al., 2015a; He et al., 2016). From its overall geometry documented by seismic profiles, together with field and well data, this basement-cored structure corresponds to a large pop-up bounded by two conjugate fault systems necessarily rooted in a deep decollement within the basement below the Tarim. To the south, the Niya fault system is composed of a few conjugate thrust faults that locally delimitate a small pop-up, at the tip of a southward-vergent steep thrust ramp (Figs. 6, 7C, 8C and S2C) (see also Tang et al., 2014; Li et al., 2015c). To the north, the Cherchen fault system displays fault-related folds and steep thrust ramps with a clear northward vergence and a hangingwall uplift of up to ~1.5 km, which is larger than that of the Niya fault system (Figs. 6, 7C, 8C and S2C) (see also Lin et al., 2012b, 2012c; Tang et al., 2014; Li et al., 2015c Liu et al., 2015a; He et al., 2016; Jiang et al., 2018). Consequently, the Tanan pop-up has clearly developed parallel to the Altyn Tagh Range over its entire length (Fig. 6), and its main vergence appears to be toward the northwest, i.e. synthetic to the Altyn Tagh deformation. However, in spite of this clear northwestward vergence, there is no evidence of flexural subsidence at the front of the Tanan uplift (Figs. 7C, 8C and S2C).

In its central part, where the two conjugate bounding fault systems are present, this large pop-up is relatively symmetric (Figs. 6, 7C, 8C and S2C) (see also Li et al., 2015c). However, where the Niya fault system vanishes laterally, the Tanan pop-up becomes more asymmetric and acquires the geometry of a large fault-propagation fold (Liu et al., 2015a; Jiang et al., 2018). Finally, at the lateral terminations of the Tanan uplift, the offset of the Cherchen fault system decreases and the associated basement-cored fold progressively flattens toward the eastern part of the Tarim Basin to the northeast and the eastern end of the Western Kunlun Range to the southwest (Fig. 6). In this area, the Hotan-Qira normal fault system is a series of conjugate normal faults described and interpreted by Avouac and Peltzer (1993) as related to the subsidence of the Tarim Basin loaded by the Western Kunlun mountain range. However, seismic profiles in this area (Fig. 1) led us to re-evaluate these faults as extrado normal faults above the southwestward vanishing basement-cored fold of the Tanan uplift (see also Li et al., 2018b).

Based on seismic profiles, together with field and well data, previous studies have demonstrated that the Tanan uplift is an inherited Protero-Paleozoic compressive structure active during the early stages of the Tarim evolution (e.g., Lin et al., 2012b, 2012c; Gao and Fan, 2014;

Lin et al., 2015a; Liu et al., 2015a; He et al., 2016). Here again, the restoration of this uplift at the beginning of the Cenozoic supports a former activity since the compressional offsets accumulated by the Pre-Cenozoic deposits along the Tanan bordering faults are not totally reset (Fig. 7C). As for the Bachu uplift, these faults were then reactivated in compression during the Cenozoic. However, although well visible on seismic profiles all along the Altyn Tagh Range, the Cherchen fault system has not been reactivated significantly all along its entire length. Indeed, at the eastern end of the basin, this fault system does not yet present any geometrical evidence for a significant cumulative Cenozoic deformation (Figs. 7D, 8D and S2D) (see also Morin et al., 2019). Yet, reactivation of this part of the fault system could be currently ongoing since some clues of recent activity exist at its eastern termination (Chang et al., 2014a).

Where it is reactivated, the Cherchen fault system now corresponds to the present-day hidden to emergent deformation front of the Altyn Tagh wedge, located in the basin ~100-150 km away from the topographic mountain front. Remarkably, this structure also localizes a major stratigraphic change between the Altyn Tagh Paleozoic domain with Silurian to Devonian metamorphic and plutonic rocks covered by Carboniferous deposits (see section 2.3) to the south, and the Tarim Paleozoic domain with Cambrian to Permian sediments (see section 2.1) to the north (Figs. 7C and 8C) (e.g., Lin et al., 2012b, 2012c; Tang et al., 2014; Li et al., 2015c; Liu et al., 2015a; He et al., 2016). Accordingly, the Cherchen fault system is a major inherited structure equivalent to the deep basement ramp below the Western Kunlun outer belt, where a similar change between two stratigraphic domains is localized. Together, these structures therefore represent a major tectonic palaeo-boundary between the Paleozoic orogenic systems of the Tibetan edge to the south and the contemporaneous Tarim Basin to the north.

This tectonic palaeo-boundary was thus reactivated during the Cenozoic all along the northern edge of the Tibetan Plateau. In the foreland of the Western Kunlun compressive system, the deformation also propagated as far north as the Bachu uplift (Figs. 6, 7B and S2B), whereas in the foreland of the Altyn Tagh transpressive system, there is no evidence of Cenozoic activity further north than the Tanan uplift (Figs. 6, 7C and S2C), even though some inherited Protero-Paleozoic structures, known as the Tazhong and Tadong uplifts, also exist in the central part of the basin (Figs. 6, 7C, 7D, S2C and S2D) (see also Lin et al., 2012b, 2012c; Tang et al., 2014; Lin et al., 2015c; Liu et al., 2015a; He et al., 2016). Indeed, there is little evidence of a significant Cenozoic activity on the bounding faults of these basement highs, and if deformation

occurs in this part of the basin, it remains very limited. In this undeformed area of the Tarim, the Cenozoic deposits are typically less than ~2 km thick.

6.4. Deformation amount

Along the two transects crossing the Altyn Tagh strike-slip system, we quantified the shortening from the main faults bounding the southeastern Tarim Cenozoic series (i.e. from the Tam Karaul and Northern Altyn Tagh thrust faults at the rear of the outer range) to the centre of the basin (see Figs. 6, 7C and 7D for the fixed reference lines set at the turning points in the centre of sections C and D). Accordingly, the shortening values and proportions given just below do not account for the deformation accommodated within the inner range. In its outer range and foreland only, the Altyn Tagh strike-slip wedge accommodates a small amount of Cenozoic compressive deformation, with a total shortening of ~0.9 and ~0.3 km measured to the west and to the east of the system, respectively (Fig. 7C and 7D).

To the west (transect C), the measured shortening is distributed between the outer range and the Tanan uplift, with ~0.3 km (~33.3% of the above ~0.9 km of total shortening) accommodated within the outer belt and ~0.6 km (~66.7%) within the basin. Across the Tanan uplift, ~0.2 km (~22.2% of the ~0.9 km of total shortening) are accommodated by the Niya fault system and ~0.4 km (~44.5%) by the Cherchen thrust and associated faults. To the east (transect D), the entire measured ~0.3 km shortening concentrates in the outer range and is accommodated by the local basement thrust ramps.

According to these estimates, the shortening accumulated within the Altyn Tagh strike-slip wedge outward from the inner range is very limited. Morevover, it decreases from the southwest to the northeast to become almost negligible at the eastern termination of the system. The structure and high topography of the inner range indicate that most of the shortening must rather be accommodated in this internal part of the system. However, even though we were not able to restore and quantify this deformation given the lack of stratigraphic markers in the range interior, the slight flexure associated with the Altyn Tagh wedge suggests a limited cumulative shortening and thickening, as expected for such a strike-slip system. Indeed, previous studies demonstrated that a large amount of strike-slip deformation is accommodated on major strike-slip faults in the range such as the Altyn Tagh fault (e.g., Wang, 1997; Cowgill et al., 2000,

2003; Sobel, 2001; Yue et al., 2001; Meng et al., 2001; Yin et al., 2002; Gehrels et al., 2003; Ding et al., 2004; Cheng et al., 2015, 2016a). Strike-slip motion may also have occurred in the basin, along the Niya and Cherchen bounding fault systems of the Tanan uplift, where very steep thrusts and relatively symmetric structures exist (see also Avouac and Peltzer, 1993; Yin et al., 2002). However, our 2D restoration does not allow for quantifying these movements, which take place outside of the planes of our sections.

7. Northwest deformation

To the northwest of the Tarim Basin, the southeastward-vergent Southwestern Tian Shan thrust system can be divided into three structural parts with, from the northwest to the southeast: (1) the inner range from the Nikolaev Line and Narat fault to the Muziduke thrust and Southern Tian Shan fault system, (2) the outer range from the Muziduke thrust and Southern Tian Shan fault system to the Kashgar deformation front, Kepingtage thrust, Kalpintagh fault, and Kuqa deformation front, and (3) the Southwest and North depressions at the front of the Kashgar deformation front, Kalpintagh thrust and Kuqa deformation front (Figs. 6, 7A, 7B, 7C, 8A, 8B, 10C, S2B and S2C).

7.1. Southwestern Tian Shan inner range

The inner range is several 10s to ~200 km wide, with typical elevations between ~2500 and ~7400 m. It is composed of exhumed imbricates of the Southern Tian Shan Proterozoic basement, Paleozoic (Devonian to Permian) plutons, and Paleozoic-Mesozoic (Silurian to Cretaceous) cover (see section 2.4). It also comprises a few compressive intra-mountainous basins filled by Cenozoic sediments, such as the Bayanbulak Basin for example (Fig. 6). In the Southwestern Tian Shan system, the inner range is a continuous belt crossed by the Talas Fergana fault to the southwest and in continuity with the Southeastern Tian Shan interior to the northeast (Fig. 6). Despite numerous surface and subsurface studies, its detailed structure remains controversial. To the southwest, connecting the major basement faults, such as the Muziduke thrust and Southern Tian Shan fault system, to a deep basal decollement seems a reasonable hypothesis (Figs. 7A, 7B, 10A and 10B) (see also Buslov et al., 2007; Gao et al.,

2013; Jia et al., 2015). However, alternative interpretations have been proposed with these major faults crossing the entire crust or branching onto the Southern Tian Shan fault system (e.g., Allen et al., 1999; Loury et al., 2017; Makarov et al., 2010; Xiao et al., 2013). To the northeast, the Southern Tian Shan fault system is much steeper and possibly cuts through the whole crust since its location at the surface correlates with a step in the Moho at depth (Figs. 7C and 10C) (Li et al., 2007; Qi et al., 2009; Wen et al., 2017). Alternatively, this major basement fault system has also been suggested to connect at depth into a deep basal decollement (e.g., Yin et al., 1998; Poupinet et al., 2002). Toward the southeast, the range interior is then separated from the outer range by the Muziduke thrust to the southwest and the Southern Tian Shan fault system to the northeast (Fig. 6). These emergent thrust zones also correspond to the main bordering faults of the northwestern Cenozoic series of the Tarim Basin.

Remarkably, in the western and central parts of the Southwestern Tian Shan, the stratigraphy of the Paleozoic terrains is different on both sides of the Muziduke thrust and Southern Tian Shan fault system (Figs. 7A, 7B, 10A and 10B). To the northwest, this stratigraphy is characteristic of the Southern Tian Shan Paleozoic Range with Silurian to Devonian metamorphic and plutonic rocks covered by Devonian to Permian deposits (see section 2.4), whereas to the southeast, it is typical of the Paleozoic Tarim Basin with Cambrian to Permian sediments (see section 2.1) (Fig. 2). Therefore, the Muziduke thrust and Southern Tian Shan fault system seem to be major inherited Paleozoic structures that have been reactivated during the Cenozoic. Such a major stratigraphic change also occurs in the northeastern part of the Southwestern Tian Shan, but it seems to be located slightly to the south, within the outer range.

7.2. Southwestern Tian Shan outer range and Kuqa depression

At the front of the inner range, the outer range is also several 10s to ~100 km wide, with typical elevations between ~1000 and ~2500 m. It consists in four different fold-and-thrust belts that developed below and above the Cenozoic sediments of the Tarim Basin (Figs. 6, 7A, 7B, 7C and S2C). These four belts present different styles of deformation all along the range. They are presented below from the southwest to the northeast.

7.2.1. Kashgar-Artux fold-and-thrust belt

To the southwestern end of the Southwestern Tian Shan outer range, the Kashgar-Artux fold-and-thrust belt is a ~150-km-long belt located between the Muziduke thrust and the Kashgar deformation front (Fig. 6). Several cross-sections have already been proposed across this belt (e.g., Scharer et al., 2004; Sobel et al., 2006; Heermance et al., 2007, 2008). The surface and subsurface data provide clear evidence for 10s-of-km-long, emergent or blind, folded thrust slices made of the Tarim Paleo-Mesozoic (Cambrian to Cretaceous) sedimentary cover at the rear, whereas several-km-wide and 10s-of-km-long fault-propagation or detachment folds developed within the Tarim Cenozoic (Paleogene to Quaternary) deposits at the front.

Together with the basement-involved imbricates of the inner range, these structures imply a basal decollement level that progressively shallows from the northwest to the southeast. Indeed, in the range interior, the major thrusts probably root in a deep decollement within the basement. At the transition between the inner and outer ranges, the change from thick-skinned to thin-skinned thrust slices that operates within the Paleo-Mesozoic cover then requires the presence of a ramp connecting this deep basement decollement to an intermediate one, most probably within the upper Cambrian evaporitic formation found in the western Tarim sedimentary series (e.g., Heermance et al., 2007, 2008). However, the poor quality of the seismic profiles and the lack of deep well data do not allow to precisely constrain the depth of this Paleozoic decollement in this part of the basin.

Toward the front of the outer belt, the formation of thrusts and folds within the Tarim Cenozoic cover then required the activation of a second ramp connecting this intermediate decollement at the base of the deformed Paleo-Mesozoic series to a shallow one at its top. According to the seismic profiles, together with field and well constraints, this shallow decollement corresponds to the Paleogene evaporitic assemblage located at the base of the Cenozoic sediments, at a depth of about 6 to 9 km b.s.l. in this area (e.g., Scharer et al., 2004; Sobel et al., 2006; Heermance et al., 2007, 2008). In the Kashgar-Artux belt, there is no evidence for a structural inheritance such as stratigraphic changes or non-restorable offsets across faults. Accordingly, all the structures developed in this belt likely correspond to structures created during the Cenozoic.

Although partially covered by the Cenozoic deposits coming from the Southwestern Tian Shan erosion, the frontal folds of the Kashgar-Artux belt form smooth topographies uplifted

several 10s to 100s of m above the present-day Tarim sedimentation level (Fig. 6). Along this belt, the local topographic front of the mountain range is thus localized by the detachment fold associated with the Kashgar deformation front, beyond which the Cenozoic deposits of the foreland have remained undeformed and attached to the underlying series.

7.2.2. Kepingtage fold-and-thrust belt

In the southwestern part of the Southwestern Tian Shan outer range, the Kepingtage fold-and-thrust belt is a ~230-km-long belt comprised between the Muziduke thrust to the northwest or Southern Tian Shan fault system to the northeast, and the Kepingtage thrust (Fig. 6). Several cross-sections have already been proposed through the Kepingtage belt (e.g., Yin et al., 1998; Allen et al., 1999; Turner et al., 2010; Tang et al., 2014; Yang et al., 2018b). In agreement with the previous interpretations, we concluded that the surface and subsurface data provide clear evidence for a-few-10s-of-km-wide and 10s-of-km-long thrust sheets made of the Tarim Paleozoic (Cambrian to Permian) sedimentary cover, with fault-propagation folds related to emergent thrust ramps at their front (Figs. 7 and 10A). These thrust sheets also include Cenozoic (Paleogene to Quaternary) sediments deposited in up to ~4-km-deep piggy-back basins. Associated with these compressive structures, a set of strike-slip faults perpendicular to the thrust sheets also exists in the Kepingtage belt, including the left-lateral Piqiang fault (Fig. 6) (see Allen et al., 1999; Turner et al., 2010, 2011; Yang et al., 2018b).

As in the Kashgar-Artux belt, the transition from the basement imbricates of the inner range to the sedimentary cover thrust sheets of the Kepingtage belt implies a basal decollement level that progressively shallows from the northwest to the southeast. Indeed, the major thrusts of the range interior probably root in a deep decollement within the basement, while the change from thick-skinned to thin-skinned thrust slices that involves the Paleozoic and Cenozoic cover requires the presence of a ramp connecting this deep decollement to the intermediate one within the upper Cambrian evaporitic formation of the western Tarim sedimentary series (Fig. 2) (e.g., Allen et al., 1999; Turner et al., 2010). According to the seismic profiles and field constraints, this Paleozoic decollement is located here at a depth of about 4 to 6 km b.s.l. (Figs. 7A and 10A) (see also Allen et al., 1999; Turner et al., 2010; Yang et al., 2018b). In the Kepingtage belt, the whole deformation is accommodated by the thrust sheets that grew above this decollement level,

since there is no evidence of structures rooted in a shallower one within the Cenozoic sedimentary series.

Based on field data, previous studies have documented unconformities, as well as SW-NE thickness and facies changes, in the Paleozoic sedimentary series of the Kepingtage belt (e.g. Allen et al., 1999; Turner et al., 2010, 2011; Chang et al., 2012b). Moreover, the strike-slip faults offsetting the belt are aligned with the faults present in the northwestern part of the Bachu uplift to the southeast. These observations suggest that the Kepingtage area was the place of a large inherited structure, in continuity with the one of the Bachu uplift, which has also been reactivated during the Cenozoic (e.g. Allen et al., 1999; Carroll et al., 2001; Turner et al., 2010, 2011; Yang et al., 2018b). However, the reactivated strike-slip faults appear to be perpendicular to the compressive structures of the Kepingtage belt, for which there is no evidence of a structural inheritance such as stratigraphic changes or non-restorable offsets across the faults. Therefore, the shallow thrusts rooting into the Paleozoic decollement likely correspond to faults created during the Cenozoic above a large basement-involved structure, whose inheritance rather controls the occurrence of orthogonally-oriented strike-slip deformation (e.g., Turner et al., 2010, 2011; Yang et al., 2018b).

Although partially covered by the Cenozoic deposits resulting from the erosion of the Southwestern Tian Shan, the frontal part of the Kepingtage thrust sheets form sharp topographies uplifted several 100s of m to more than ~1 km above the present-day Tarim sedimentation level (Fig. 6). In this area, the local topographic mountain front is thus localized by the Kepingtage thrust ramp emerging at the front of the belt.

7.2.3. Kalpin belt

In the central part of the Southwestern Tian Shan outer range, the Kalpin belt is a ~80-km-long belt located between the Southern Tian Shan fault system and the Kalpintagh fault (Fig. 6). As far as we know, there has been no published cross-section across this belt. According to the surface and subsurface data, this belt is composed of 10s-of-km-long, emergent and folded thrust slices and small pop-ups related to a few steep thrust ramps. These structures involved the Tarim Proterozoic basement and its Protero-Paleozoic (Sinian to Permian) cover (Figs. 7B and 10B). They also individualize two basins containing less than ~2 km of Cenozoic (Plio-

Quaternary) deposits. At depth, these structures possibly connect to a deep decollement within the basement. In the Kalpin belt, like in the Kepingtage one, there is no evidence of structures rooting into a shallow decollement level within the Cenozoic sedimentary series.

According to field data, the Kalpin area, which is known as the Kalpin uplift, appears to be a lateral extension of the large inherited Kepingtage basement structure (e.g. Allen et al., 1999; Carroll et al., 2001; Turner et al., 2010; Chang et al., 2012b). Consequently, in contrast with the neo-formed compressive structures of the thin-skinned Kepingtage fold-and-thrust belt, the basement-involved structures of the thick-skinned Kalpin belt are probably related to inherited basement faults reactivated during the Cenozoic, such as possibly for the frontal Kalpintagh thrust fault.

Although partially covered by the Cenozoic deposits coming from the erosion of the Southwestern Tian Shan, the structures of the Kalpin belt now form sharp topographies uplifted several 100s of m up to ~1.5 km above the present-day Tarim sedimentation level (Fig. 6). In this area, the local topographic front of the mountain range is localized by the Kalpintagh fault emerging at the front of the belt.

7.2.4. Kuqa fold-and-thrust belt and depression

In the northeastern part of the Southwestern Tian Shan outer range, the Kuqa fold-and-thrust belt is a ~370-km-long belt located between the Southern Tian Shan fault system and the Kuqa deformation front (Fig. 6). Numerous contradictory cross-sections have been proposed through this belt (e.g. Burchfield et al., 1999; Chen et al., 2004; He et al., 2005; Qi et al., 2009; Li et al., 2012a; Wu et al., 2014; Zhang et al., 2014b; Li et al., 2016d; Wen et al., 2017; Zhao and Wang, 2016; Wang et al., 2017; Izquierdo-Llavall et al., 2018; Neng et al., 2018). From our surface and subsurface dataset, we derived a regionally-consistent structural model settling the issue of these contradictory interpretations (see Supplementary information S4 for further details and discussion). At the rear of the belt, the surface and subsurface data provide evidence for 10s-of-km-long, emergent or blind, folded thrust slices constituted of the Southern Tian Shan Proterozoic basement, Paleozoic (Devonian to Permian) plutons and Paleo-Mesozoic (Silurian to Cretaceous) cover. At the front, 10s-of-km-long duplex structures involve the Tarim Paleo-Mesozoic (Cambrian? to Cretaceous) sedimentary cover (Figs. 7C, 10C and S2C). The surface

and subsurface data also reveal several-km-wide and up to ~200-km-long fault-propagation or detachment folds that developed within the Tarim Cenozoic (Paleogene to Quaternary) deposits at the top and the front of the basement-involved thrust slices and Paleo-Mesozoic cover duplexes (Figs. 7C, 10C and S2C). Finally, these folds individualize a few piggy-back basins, such as the ~30-km-wide and ~130-km-long Kuqa depression where ~9 km of Cenozoic sediments are stacked nearby the city of Baicheng (Fig. 6, 7C and 10C).

These structures imply a basal decollement level that progressively shallows from the north to the south. At the rear of the Kuqa belt, the major thrusts necessarily connect to a deep decollement within the basement or directly onto the Southern Tian Shan fault system. The southeastward change from the thick-skinned thrust slices to the thin-skinned duplexes then requires the presence of a ramp transmitting slip from depth to an intermediate decollement at the base of the deformed Paleo-Mesozoic sedimentary cover (Figs. 7C and 10C). However, in this part of the basin, the quality of the seismic profiles and the lack of deep well data do not allow for precisely constraining the age, lithology and depth of this intermediate decollement that remains unclear (compare the cross-sections of Chen et al., 2004; He et al., 2005; Qi et al., 2009; Li et al., 2012a; Wen et al., 2017; Wang et al., 2017; Izquierdo-Llavall et al., 2018; Neng et al., 2018; and Supplementary information S4 for more details on the different interpretations).

Nonetheless, the stratigraphy of the Paleozoic terrains appears to be different on both sides of the ramp connecting the deep and intermediate decollements (Figs. 7C and 10C). To the northwest, this stratigraphy is characteristic of the Southern Tian Shan Paleozoic domain with Silurian to Devonian metamorphic and plutonic rocks directly covered by Devonian to Permian deposits (see section 2.4) (Fig. 2). To the southeast, the Proterozoic basement of the Tarim Basin could be topped by a lower Paleozoic series, even if the latter is truncated by an unconformity located at the base of the overlying Mesozoic sediments (Fig. 2). The occurrence within this Paleo-Mesozoic cover of a sedimentary level acting as an intermediate decollement in the Kuqa belt, but which does not exist at the surface further north, is an additional indication of a significant stratigraphic change between these two Paleozoic domains with Southern Tian Shan vs. Tarim stratigraphic affinities. Therefore, the ramp connecting the deep and intermediate decollements to the northwest of the Kuqa belt seems to be a major inherited Paleozoic structure reactivated during the Cenozoic, similar to the Muziduke thrust and the Southern Tian Shan fault system further west. Together, these structures thus represent a major structural palaeo-boundary

between the Paleozoic orogenic systems of the Southern Tian Shan to the north and the contemporaneous Tarim Basin to the south.

At the front of the Kuqa belt, the formation of duplexes within the Tarim Paleo-Mesozoic cover and of thrusts and folds within the Cenozoic deposits requires the activation of blind ramps connecting the intermediate decollement to a shallow one between the two sedimentary series (Figs. 7C, 10C and S2C). Based on the field constraints, seismic profiles, and well data, this shallow decollement is located at a depth of about 5 to 8 km b.s.l. at the front of the duplexes, within the Paleogene evaporitic assemblage of the Cenozoic deposits (see also Chen et al., 2004; He et al., 2005; Li et al., 2012a; Wu et al., 2014; Tian et al., 2016; Izquierdo-Llavall et al., 2018; Neng et al., 2018). Below this decollement, the interpretation and reconstruction of the underlying duplexes may be problematic because of a strong component of salt tectonics, as well as a seismic imaging degraded by the presence of evaporites (e.g., Chen et al., 2004; He et al., 2005; Li et al., 2012a; Wu et al., 2014; Li et al., 2016d; Tian et al., 2016; Wang et al., 2017; Izquierdo-Llavall et al., 2018; Neng et al., 2018). However, the stratigraphy of the Paleo-Mesozoic cover seems to be the same across the ramps connecting the Paleozoic and Cenozoic decollements. Therefore, these shallow ramps in the centre of the Kuqa belt likely correspond to structures created during the Cenozoic.

Above the basement-involved thrust slices and Paleo-Mesozoic cover duplexes, the slip is transferred toward the top and the front of the Kuqa belt through the Cenozoic decollement. Within the Cenozoic deposits, long fault-propagation or detachment folds developed in association with emergent or blind thrust ramps, often with a strong component of salt tectonics (Figs. 7C and 10C) (e.g. Chen et al., 2004; He et al., 2005; Hubert-Ferrari et al., 2007; Li et al., 2012a; Wu et al., 2014; Li et al., 2016d; Tian et al., 2016; Zhao and Wang, 2016; Wang et al., 2017; Izquierdo-Llavall et al., 2018; Neng et al., 2018). These folds are located just at the front of the structures involving the basement and the Paleozoic cover below the Cenozoic decollement, or a few 10s of km further south. In this case, these most frontal folds individualize the Kuqa depression that corresponds to a piggy-back basin developed within a wide syncline at their rear (Figs. 6, 7C and 10C).

Although largely covered by the Cenozoic deposits resulting from the erosion of the Southwestern Tian Shan, these frontal folds localize the topographic front of the mountain range. At the surface of the basin, they usually form smooth topographies uplifted several 100s of m

above the present-day Tarim sedimentation level (Fig. 6). Along the belt, the topographic front is thus localized by the detachment folds at the front of the Kuqa belt. Further southeast, the Cenozoic deposits of the foreland have remained undeformed and attached to the underlying series.

7.3. Southwest and North depressions

The Tarim Basin at the front of the Southwestern Tian Shan outer range can be considered in terms of different sub-areas, which are presented below from the southwest to the northeast.

The Tarim Basin sub-area located at the front of the Kashgar-Artux belt corresponds to the northwestern termination of the Southwest depression (Fig. 6). There, this depression corresponds to the region where the accommodation space is maximal in the Tarim Basin, with up to ~10 km of Cenozoic sediments nearby Kashgar. Indeed, the added loads of the Western Kunlun and Southwestern Tian Shan thrust wedges probably explain the very strong flexural subsidence of this specific area. In this foreland system, the Western Kunlun outer belt and the Kashgar-Artux belt correspond to two facing wedge-top depozones, and the Southwest depression located between these belts to a triangular foredeep, according to the terminology of DeCelles and Giles (1996).

At the front of the Kepingtage belt, there is no such depression (Figs. 7A and 10A). Indeed, this belt is thrusted over the western part of the Bachu uplift, which clearly prevents the development of a flexural foredeep (Fig. 6). Moreover, the Bachu high seems to persist and be also active below the Kepingtage belt (see also Allen et al., 1999; Turner et al., 2010), possibly interfering with its deformation. In particular, this may explain why the Kepingtage wedge-top depozone (terminology of DeCelles and Giles, 1996) is mainly developed above the sedimentation level, with deeply-eroded anticlines at the front of the thrust sheets and shallow piggy-back basins at their top.

Finally, the Tarim Basin sub-area located at the front of the Kalpin and Kuqa belts is known as the North depression (Fig. 6). In this area, the Tarim basement and sedimentary cover are tilted northward so that the Cenozoic deposits thicken toward the Southwestern Tian Shan and reach their maximum thickness at the front of its outer belt (Figs. 7B, 7C, 10B, 10C, S2B

and S2C). This overall geometry of the northern Tarim is thus typical of a flexural basin, associated here with the shortening and thickening accumulated in the Southwestern Tian Shan thrust system. It corresponds to a region of high accommodation space, with up to ~7 km of Cenozoic sediments to the south of Aksu, i.e. at the front of the Kalpin belt (Figs. 7B, 10B and S2B). Moreover, to the northeast, the North depression is bounded by the Kuqa belt, which in turn surrounds the Kuqa depression where up to ~9 km of Cenozoic deposits are trapped close to the city of Baicheng (Figs. 7C and 10C). In this foreland system, the Kuqa belt and its associated depression correspond to the wedge-top depozone, the North depression at the front of this belt represents the foredeep, and the undeformed central area of the basin constitutes the forebulge (terminology of DeCelles and Giles, 1996).

At the transition between these foredeep and forebulge, an inherited Protero-Paleozoic basement-cored structure called the Tabei uplift exists. However, there is little evidence of a significant Cenozoic activity on the faults associated with this basement high, except to its very eastern part. There, its southern bounding fault appears to have been reactivated as a normal fault, most probably in response to the stresses generated by the flexural bending of the northern Tarim Basin. However, this Cenozoic deformation occuring in the northern part of the basin remains very limited (Figs. 7C, 10C and S2C).

7.4. Deformation amount

Along the transects crossing the Southwestern Tian Shan thrust system, we quantified the shortening from the main faults bounding the northwestern Tarim Cenozoic series (i.e. from the Muziduke thrust and Southern Tian Shan fault system at the rear of the outer range) to the centre of the basin (see Figs. 6, 7A, 7B and 7C for the fixed reference lines set at the turning points in the centre of sections A, B and C). Accordingly, the shortening values and proportions given just below do not account for the deformation accommodated within the inner range. In its outer range only, the Southwestern Tian Shan thrust wedge already accommodates a large amount of Cenozoic compressive deformation, with a total shortening of ~36 and ~22 km measured to the southwest and to the northeast, i.e. through the Kepingtage and Kuqa belts, respectively (Figs. 7A and 7C). These shortening amounts are in the range of the other values published from previous cross-section restorations of these systems, which range from 23 to 50 km for the

Kepingtage belt (e.g., Yin et al., 1998; Allen et al., 1999; Yang et al., 2007b; Turner et al., 2010), and from ~10 to ~42 km for the Kuqa one (e.g., Yin et al., 1998, Burchfield et al., 1999; Li et al., 2012a; Zhang et al., 2014b; Tian et al., 2016; Wen et al., 2017; Izquierdo-Llavall et al., 2018). Unfortunately, in the absence of a preserved Mesozoic-Cenozoic stratigraphic marker, it was not possible to properly quantify the Cenozoic deformation accumulated in the central part of the Southwestern Tian Shan compressive system, i.e. through the Kalpin belt, since eroded material cannot be reconstructed. The proposed restoration therefore only provides a very low and probably meaningless minimum estimate of ~4 km for the total shortening across this belt.

In the Southwestern Tian Shan, the whole quantified shortening is accommodated in the outer range with no shortening within the basin. To the southwest, in the Kepingtage belt (transect A), the ~36 km of total shortening are a minimum estimate due to the eroded front of the cover thrust sheets, which accommodate 100% of the deformation. To the northeast, in the Kuqa belt (transect C), ~19 km (~86.4% of the ~22 km of total shortening there) are accommodated by the basement-involved thrust slices and ~3 km (~13.6%) by the cover duplexes.

According to these estimates, the shortening accumulated within the Southwestern Tian Shan thrust wedge outward from the inner range decreases from west to east. The structure and high topography of the range interior, together with the large flexure of the Southwest and North depressions, indicate that a large amount of shortening must also be accommodated in this internal part of the system. However, the absence of stratigraphic markers impedes here the quantification of this deformation using a structural restoration approach.

In addition to shortening, strike-slip deformation may be accommodated on strike-slip fault systems in the range (e.g., Yin et al., 1998; Zubovitch et al., 2010). Strike-slip motion may also have occurred on faults at the margins of the basin, for example on the steep Kalpintagh fault (Li et al., 2015d). However, our 2D restoration does not allow for quantifying such movements, which take place outside of the planes of our sections.

8. Northeast deformation

To the northeast of the Tarim Basin, the southward-vergent Southeastern Tian Shan strike-slip system can be divided into two parts with, from the north to the south: (1) the inner

range from the right-lateral Baluntay fault to the right-lateral Korla fault, and (2) the outer range from the Korla fault to the Lop Nur fault system (Figs. 6, 7D, 10D and S2D).

8.1. Southeastern Tian Shan inner range

The inner range is several 10s to ~140 km wide, with typical elevations between ~1000 and ~4800 m. It is composed of exhumed imbricates of the Southern Tian Shan Proterozoic basement, Paleozoic (Devonian to Permian) plutons, and Paleozoic-Mesozoic (Silurian to Jurassic) cover (see section 2.4). These terrains are in continuity with the Southwestern Tian Shan interior further west (Fig. 6). A few intra-mountainous basins filled by Cenozoic sediments, such as the Korla Basin for example, are also included in this part of the range (Fig. 6). There, the steep inherited Paleozoic faults have been mainly reactivated as right-lateral strike-slip faults that delimitate some ridges separating the basins (e.g., XBGMR, 1976, 1985; Yin et al., 1998; Allen et al., 1994; Li et al., 2016a), a deformation style typical of a transpressive system. In this system, the major faults appear to cut through the whole crust since their location at the surface correlates with steps in the Moho at depth (Li et al., 2016a). To the south, this inner range is separated from the outer range by the Korla fault. However, this strike-slip fault zone does not always correspond to the northeastern boundary of the Cenozoic series of the Tarim Basin, which is most often located further south (Fig. 6).

In this part of the Southern Tian Shan, the main stratigraphic change between the Paleozoic range and the Paleozoic Tarim Basin is localized on the Kuruk Tagh fault system (Figs. 7D and 10D) (e.g., XBGMR, 1976, 1985; Charvet et al., 2011). Accordingly, this fault zone is a major inherited structure equivalent to the thrust ramps at the font of the basement imbricates of the Southwestern Tian Shan outer belt. The Kuruk Tagh fault system thus corresponds to the eastward extension of the major deformation palaeo-boundary between the Paleozoic orogenic systems of the Southern Tian Shan to the north and the contemporaneous Tarim Basin to the south.

8.2. Southeastern Tian Shan outer range

At the front of the inner range, the outer range is a few to several 10s of km wide, with typical elevations between ~800 and ~1000 m. To our knowledge, no cross-section across this outer range has ever been published. However, like the Altyn Tagh transpressional system bordering the Tarim Basin to the southeast, the Southeastern Tian Shan strike-slip wedge does not have any fold-and-thrust belt in its outer part. According to the surface and subsurface data, the outer range is composed of 100s-of-km-long basement-involved structures made of the Tarim Proterozoic basement and its Protero-Paleozoic to Cenozoic (Sinian to Quaternary) cover (Figs. 7D and 10D). These structures are related to emergent or blind faults, such as the Lop Nur fault system. Although very steep to nearly vertical, these faults generally have a north block uplifted by a few 10s to 100s of m, which indicates a southward vergence (Figs. 7D, 10D and S2D). At depth, all these structures possibly connect to a deep basal decollement within the basement (e.g., Charvet et al., 2011).

Unconformities, together with thickness and facies changes, were documented from surface observations in the Protero-Paleozoic (Sinian to Devonian) sedimentary cover of the outer range, such as in the Tarim Basin to the south (e.g., Tang et al., 2008; Lin et al., 2012b; Wu et al., 2018; Morin et al., 2019). These observations imply that the Lop Nur fault system and the associated basement-cored uplift, which is known as the Kuruk Tagh uplift, are inherited Protero-Paleozoic structures of the Tarim Basin reactivated during the Cenozoic. In the Southeastern Tian Shan outer range, the whole Cenozoic deformation is associated with these inherited faults, since there is no evidence of younger structures rooting into a Paleozoic or Cenozoic decollement level in the sedimentary series at their front.

The large basement-involved structure of the outer range now forms a smooth topography uplifted by a few 100s of m above the present-day Tarim sedimentation level, and localizes the mountain front (Fig. 6). Located several kilometres further south, the Lop Nur fault system, which corresponds to the present-day deformation front of the Southeastern Tian Shan range, is hidden by onlapping Plio-Quaternary deposits (Figs. 6, 7D, 10D and S2D). At the front of this fault system, there is no evidence of a significant flexural subsidence, with less than ~1 km of Cenozoic sediments trapped in this part of the basin (Figs. 7D, 10D and S2D) (see also Morin et al., 2019). There, some inherited Protero-Paleozoic structures also exist, but there is little evidence of a significant Cenozoic activity on their bounding faults, so that any eventual Cenozoic deformation in this area would have remained very limited. However, towards the very

eastern end of the Tarim Basin, other likely inherited structures may have been slightly reactivated (Fig. 6).

8.3. Deformation amount

Along the transect crossing the Southeastern Tian Shan strike-slip system, we quantified the shortening from the main bordering fault of the northeastern Tarim Cenozoic series (i.e. from the Korla fault in the outer range) to the centre of the basin (see Figs. 6 and 7D for the fixed reference lines set at the turning points in the centre of section D). Accordingly, the shortening values given just below do not account for the deformation accommodated within the inner range. In its outer range only, the Southeastern Tian Shan strike-slip wedge accommodates a very limited amount of Cenozoic compressive deformation, with a possible total shortening of less than several 10s of m. However, in the absence of a preserved Mesozoic-Cenozoic stratigraphic marker, it was not possible to properly quantify the Cenozoic shortening, since eroded material cannot be reconstructed. Nevertheless, this shortening is entirely accommodated by basement-involved structures.

Even if the compressive deformation accumulated within the outer range of the Southeastern Tian Shan strike-slip wedge is poorly constrained, it seems to be limited. Moreover, the structure and low topography of the inner range suggest that the compressive deformation accommodated across this internal part of the system should also be limited. Even though the absence of stratigraphic markers impedes any restoration and quantification of the deformation within the inner range, the non-existence of a flexure associated with the Southeastern Tian Shan supports limited shortening and thickening, typical of such a strike-slip wedge. Instead, a large amount of strike-slip movements has likely been accommodated on major strike-slip faults of the range, such as the Kuruk Tagh fault system or the Korla fault. Strike-slip motion may also have occurred in the basin, along the very steep Lop Nur faults for instance. However, 2D restoration does not allow for quantifying such deformation, which take place outside of the plane of our section.

9. Discussion

9.1. Neo-formed structures and particular case of the Mazar Tagh thrust sheet

In the outer part of the ranges surrounding the Tarim Basin, a significant fraction of the deformation (up to 100%) is accommodated by structures neo-formed during the Cenozoic (Table 1). However, these neo-formed structures are restricted to the sedimentary cover (thin-skinned deformation) at the front of the Western Kunlun Range and Southwestern Tian Shan, where the amount of compressive deformation is most important (Fig. 11). In contrast, neo-formed structures are absent at the front of the Altyn Tagh or Southeastern Tian Shan transpressive systems. In addition, the development of these structures is also strongly correlated with the occurrence of Paleozoic and Cenozoic favorable decollement levels in the sedimentary cover.

Among these neo-formed structures, the Mazar Tagh thrust sheet, which is located at the front of the Western Kunlun, has remarkable dimensions (Figs. 6, 7B, 8B and 11). With a north-south width of ~150-200 km and an east-west length of ~300 km, it could even be the largest active thrust sheet in the world without internal deformation (see also Wang et al., 2014c, Suppe et al., 2015; Guilbaud et al., 2017). Consequently, the whole foredeep sedimentary pile (i.e. the sediments of the Southwest depression) is detached at the base of the Cenozoic series and transported northwards. The Mazar Tagh thrust sheet is therefore oversized compared to classical thrust sheets. To the first order, the size of a thrust sheet is controlled by the ratio between its internal resistance (depending on its thickness) and its basal friction (depending on the nature and thickness of its basal decollement level) (e.g., Liu et al., 1992; Mandal et al., 1997; Smit et al., 2003; Hatcher, 2004). Accordingly, the gypsiferous Paleocene-Eocene decollement level should thus be very efficient (i.e. with a low basal friction) to allow for the development of the Mazar Tagh thrust sheet (Suppe et al., 2015). However, this is probably not the only explanation for such an oversized thrust sheet. Indeed, the large thickness (up to ~10 km) of sediments trapped in the Southwest depression may have also drastically increased the rigidity of this thrust sheet, leading to the emergence of its frontal ramps far away from the range topographic front, where flexure, accommodation and sedimentation are reduced (e.g., Mugnier et al., 1997; Fillon et al., 2013).

Finally, an obvious spatial correlation exists between the location of the Mazar Tagh emergent thrust ramps rooting into the Cenozoic decollement and the Mazar Tagh deep faults

below it (Fig. 6). In fact, these ramps appear to emerge towards the surface from existing structural steps in this decollement, caused by the hangingwall uplift of the underlying basement-cored structures (Figs. S2B, 7B, 8B and 9). Therefore, the deformation of the Cenozoic decollement by the deep Mazar Tagh thrusts most probably controlled the subsequent localization of the shallow ramps. Potentially, the Mazar Tagh thrust sheet could have been even wider if this basement structures did not exist.

9.2. Structural inheritance

In the ranges surrounding the Tarim Basin, metamorphic and stratigraphic evidences indicate that the basement-cored structures (thick-skinned deformation) are inherited from the orogens that developed around the Tarim block during the Paleozoic (e.g., Windley et al., 1990; Allen et al., 1993, 1994; Matte et al., 1996; Jolivet et al., 2010, 2013; Glorie et al., 2011; Macaulay et al., 2014; this study). Within the inner ranges, these inherited structures absorb all the deformation, while in the outer ranges they accommodate from 0 to 100% of the shortening (Fig. 11; Table 1). Within the basin, at the front of the Altyn Tagh Range, the Tanan uplift also corresponds to an inherited structure from the large Paleozoic orogenic system of the southern margin of the Tarim block. Together with the most frontal basement ramp below the Western Kunlun outer belt, this structure corresponds to a major structural palaeo-boundary between the Paleozoic ranges to the south and the contemporaneous Tarim Basin to the north (Fig. 11). To the north, the structural palaeo-boundary between the Paleozoic Tian Shan and the Tarim Basin also presents evidence of a Cenozoic activity along its whole length. Accordingly, the Paleozoic structures all around the Tarim block have been reactivated during the Cenozoic orogeny (Fig. 11).

In the outer part of the Tian Shan and within the basin, structures inherited from the Protero-Paleozoic history of the Tarim block were also reactivated (e.g., Allen et al., 1999; Carroll et al., 2001; Turner et al., 2010, 2011; Chang et al., 2012b; this study). The Kalpin and Kuruk Tagh uplifts are now part of the Southwestern and Southeastern Tian Shan outer ranges, respectively (Fig. 11). On the other hand, in the western part of the Tarim Basin, the Bachu uplift was rejuvenated in the foreland of the Western Kunlun (Fig. 11).

The Cenozoic reactivation of all those Paleozoic and Protero-Paleozoic structures confirms the major role of structural inheritance in continental deformation, as already widely demonstrated in Asia (e.g., Molnar et al., 1981; Windley et al., 1990; Matte et al., 1996; De Grave et al., 2007; Jolivet et al., 2010; Jolivet et al., 2013; Tang et al., 2014). However, all the inherited Protero-Paleozoic structures in the basin have not been reactivated. If the Tanan and Bachu uplifts show evidence of a significant Cenozoic deformation, such is not the case for the Tazhong, Tadong and Tabei uplifts (Figs. 6, 7 and 11). The location and orientation of the Tanan and Bachu structures may have played a decisive role in their reactivation, with a compressive vs. strike-slip main deformation component similar to the one of the local edge of the Tibetan Plateau. Indeed, the Tanan uplift, which is probably reactivated with a prevailing strike-slip component, is oriented parallel to the Altyn Tagh and located just to the front of this range. The Bachu uplift, which is reactivated with a prevailing compressive component, is oriented parallel to the Western Kunlun Range and developed where the forebulge should have been located in the foreland of this orogenic system. In contrast, the Tazhong, Tadong and Tabei uplifts were not reactivated even though their orientations are comparabale to the ones of the surrounding ranges, probably because they are located further from the Tibetan Plateau edge.

In spite of all the reactivated structures in the Tarim basin and surrounding ranges, the experimental and numerical models designed to understand the Cenozoic deformation of Asia usually only focus on the influence of stress boundary conditions and lithospheric rheology, but neglect structural inheritance (e.g. Tapponnier et al., 1982; Vilotte et al., 1984; England and Houseman, 1985; Davy and Cobbold, 1988; Peltzer and Tapponnier, 1988; Burg et al., 1994; Neil and Houseman, 1997; Wang et al., 2007; Dayem et al., 2009; Calignano et al., 2015). Ideally, these various parameters should be all considered in the modelling. In the future, testing the effect of different stress boundary conditions on the reactivation of the inherited basement structures in the area could be a step forward, as a comprehensive regional study is now available to compare with model results.

9.3. Strike-slip faults and potential deformation partitioning

This study mainly deals with the compressive deformation in the Tarim region since 2D restoration does not allow for quantifying strike-slip movements. However, strike-slip

deformation may occur in various places in the ranges (e.g., Wang, 1997; Cowgill et al., 2000, 2003; Sobel, 2001; Yue et al., 2001; Meng et al., 2001; Yin et al., 2002; Gehrels et al., 2003; Ding et al., 2004; Cowgill, 2010; Cheng et al., 2015, 2016a; Wang et al., 2016b) and in the basin, such as on the fault systems bounding the Tanan and Bachu uplifts (e.g., Avouac and Peltzer, 1993; Yin et al., 2002; Li et al., 2016e; Yang et al., 2018b; this study). Indeed, the central part of the Tanan uplift corresponds to a symmetric basement pop-up bounded by steep (> 50°) thrusts (Figs. 6, 7C and 8C), an overall geometry characteristic of strike-slip structures (e.g., Casas et al., 2001; McClay and Bonora, 2001 and references therein; Woodcock and Rickards, 2003). The Bachu uplift also corresponds to an asymmetric (to the east) or symmetric (to the west) basement pop-up with steep (> 60°) bounding thrusts, in particular in the case of the Seyibula or Mazar Tagh deep fault systems (Figs. 6, 7B and 9). Vertical faults may even be observed in these systems (Li et al., 2016e). The existence of these potential strike-slip structures may indicate deformation partitioning through the Bachu uplift, with a prevailing compressive component to the north (on the Aqia-Tumuxiuke thrust systems) and a prevailing strike-slip one to the south (on the Seyibula-Mazar Tagh deep fault systems) (Fig. 6). As for the structure orientation, this configuration is similar to the one of the Western Kunlun Range where deformation is partitioned between compressive structures to the front, and the Kashgar-Yecheng transfer system and the Karakax strike-slip fault to the rear.

Additionally, a few studies proposed a prolongation of the Talas Fergana strike-slip fault (Shache-Yangdaman fault) inside the Tarim Basin, in front of the Pamir Range, southeastward down to the city of Yecheng (Wei et al., 2013; Blayney et al., 2016, 2019; Bande et al., 2017b). However, we find no evidence of deformation associated with such a fault prolongation, neither at the surface, nor on the seismic data in spite of some available seismic profiles crossing the supposed fault location (Figs. 1, S2A, 7A and 8A). Indeed, the Shache basement fault below the Jiede anticline nearby Yecheng has a limited lateral extension (Fig. 6), since it is not observed on the seismic lines available laterally. Consequently, this structure cannot be a prolongation of the Talas Fergana fault. A horsetail splay termination of this fault into the Southwestern Tian Shan thrusts, as suggested by Jia et al., (2015), seems to be a more reasonable interpretation, with regards to our dataset in the basin.

Finally, the sharp eastern edges of the Western Kunlun Range and Bachu uplift in map view could suggest the occurrence of a major NNE-SSW strike-slip fault linking both

terminations. However, we did not observe any evidence for such a fault in the numerous seismic lines crossing the area (Fig. 1). The eastern extremities of the Western Kunlun Range and Bachu uplift rather correspond to a progressive, but locally abrupt, eastward decline of their structures (Fig. 6).

9.4. Shortening

In the basin and the outer part of the surrounding ranges, we quantified the Cenozoic shortening from structural restorations (Fig. 7; Table 1). However, the associated estimates correspond to the deformation accommodated from the margins of the basin to its centre, and therefore consist in minimum values with respect to the total shortening accumulated in the ranges. Indeed, our restorations do not account for the shortening absorbed across the inner ranges. In order to assess the total deformation across the ranges, we used a crustal budget approach (for the methodology see Fig. 12A and 12B, as well as the Supplementary information S5 and references therein). This approach is based on the conservation of the crustal matter during deformation. Practically, it corresponds to an area balancing of the crust of the ranges between the present-day and initial states of deformation (e.g., Ménard et al., 1991; Avouac et al., 1993; Teixell, 1998). Eventually, the compressive deformation across the inner ranges can be inferred from the difference between the shortening estimates across the entire and the outer ranges (Table 1).

In the Western Kunlun compressive system, we estimate a total crustal shortening of ~49.5 +23/-17.5 km to the west (transect A) and ~83 ± 23 km to the east (transect B) (Fig. S6A1 and S6B1; Table 1). This compressive deformation is essentially accommodated within the entire (inner and outer) range when compared to the basin, with ~99% (49 +23/-17.5 km) and ~94% (78 ± 23 km) of this total shortening concentrated across the range for transects A and B, respectively (Table 1). These estimates are within the wide range of values, from ~42 to ~272 km, already suggested for this orogen (Lyon-Caen and Molnar, 1984; Rumelhart et al., 1999; Cowgill et al., 2003). However, the highest of these suggested shortening values are based on the probably oversimplified assumption that the Pamir-Western Kunlun Range was initially straight and subsequently acquired its present-day bend during the Cenozoic orogeny (see Chen et al., 2018 and references therein). In the inner range, ~35.4% (17.5 +23/-17.5 km) and ~57.8% (48 ±

23 km) of the total shortening is absorbed to the west (transect A) and to the east (transect B), respectively (Table 1). In addition, ~63.6% (~31.5 km) and ~36.2% (~30 km) of the total shortening are accumulated within the outer range to the west (transects A) and to the east (transect B) (Fig. 7A and 7B; Table 1). The different shortening amounts absorbed across the inner range, when the shortening amount within the outer range is similar, could thus reflect varying proportions of strike-slip vs. compressive deformation in the interior of the mountain belt, with more strike slip deformation in its NNW-SSE part than in its WNW-ESE one. In the Tarim Basin, a significant amount of deformation is also accommodated by the Bachu uplift that absorbs ~6% (~5 km) of the total compressive deformation in the Western Kunlun system along transect B (Fig. 7B; Table 1).

Across the Altyn Tagh transpressive system, we estimate a total crustal shortening of ~38.6 ± 18 km to the west (transect C) and 24 ± 9 km to the east (transect D) (Fig. S6C1 and 6D1; Table 1). Here again, this compressive deformation is essentially accommodated within the entire (inner and outer) range when compared to the basin, with ~98.5% (38 ± 18.0 km) and 100% (24 ± 9 km) of this total shortening accommodated in the range for transects C and D, respectively (Table 1). The main part of this compressive deformation is absorbed within the inner range, with ~97.7% (37.7 ± 18 km) and ~98.8% (23.7 ± 9 km) concentrated across transects C and D, respectively (Table 1). The outer range only accumulates ~0.8 to ~1.2% (~0.3 km) of the total shortening (Fig. 7C and 7D; Table 1). To the west, a limited amount of deformation is also accommodated within the basin where the Tanan uplift accommodates ~1.5% (~0.6 km) of the total compressive deformation across the Altyn Tagh system (Fig. 7C; Table 1). To our knowledge, these values are the first shortening estimates provided for this strike-slip wedge.

Across the Southwestern Tian Shan compressive system, we estimate a total crustal shortening of 54 +24/-18 km to the west (transect A), 53 ± 23 km in the centre (transect B), and 44 ± 15 km to the east (transect C) (Fig. S6A2, S6B2 and S6C2; Table 1). This compressive deformation is totally accommodated within the range when compared to the basin (Table 1). Many other shortening values, ranging from ~80 to ~280 km, have been proposed for the Tian Shan (e.g., Molnar and Tapponnier, 1975; Chen et al., 1991; Avouac et al., 1993; Allen et al., 1994). However, these values correspond to estimates of shortening across the whole range (Northern, Central and Southern Tian Shan), and cannot be therefore easily compared with our

results. In the inner range, ~33.3% (18 +24/-18 km) and ~50% (22 ± 15 km) of the total shortening are accumulated to the west (transect A) and to east (transect C), respectively (Table 1). In the outer range, at least ~66.7% (~36 km) and ~50% (~22 km) of the compressive deformation is absorbed across the Kepingtage and Kuqa belts, respectively, to the west (transect A) and to the east (transect C) of the Southwestern Tian Shan (Fig. 7A and 7C; Table 1).

In the Southeastern Tian Shan transpressive system, we estimate a total crustal shortening of 15 +20/-15 km (transect D) that may be entirely accommodated in the inner range (Fig. S6D2; Table 1). Indeed, in the outer range, the compressive deformation seems to be negligible, with less than several 10s of m of shortening (Fig. 7D; Table 1). To our knowledge, these values are the first estimates of shortening provided for the Southeastern Tian Shan strike-slip system.

In this study, we do not have enough constraints to quantify the shortening on each side of the Paleozoic sutures in the ranges surrounding the Tarim Basin, and thus to isolate the exact contribution of compressive deformation affecting the original Proterozoic Tarim block. However, based on our shortening assessments, we find that several 10s of km of Cenozoic compressive deformation have been accommodated on the margins of the Tarim block. Nevertheless, this deformation is lower in the eastern strike-slip systems (Altyn Tagh and Southeastern Tian Shan) than in the western compressive ones (Western Kunlun and Southwestern Tian Shan). Accordingly, regarding this geological evidence and the quantified shortening, a continental crust dipping down to ~80 km below the Western Kunlun Range (e.g., Lyon-Caen and Molnar, 1984; Wittlinger et al., 2004; this study) is plausible. In contrast, a continental subduction implying a crust dipping down to ~100 km below the Altyn Tagh Range (Wittlinger et al., 1998) seems unlikely given the limited number of compressive structures and the associated very low shortening.

Finally, in addition to the Cenozoic deformation on the Tarim block margins, some basement-involved deformation also occurs within the western and southern parts of this block. Indeed, in spite of an overall flat topography due to an important sediment filling, a non-negligible amount of compressive deformation (up to a few % of the total shortening) is also accommodated within the Tarim Basin across the Bachu and Tanan uplifts. Accordingly, the Tarim block, including its central part occupied by the present-day Tarim Basin, does not correspond to a totally rigid and undeformable heterogeneity within the Asian compressive system.

9.5. Crustal structure and implications for the deformation of Central Asia

In order to propose a crustal-scale cross-section across the Tarim Basin and the surrounding mountain ranges, we combined our geological transects with Moho depths inferred from the deep geophysical data (gravimetry, tomography, seismology, rheology, etc.) available in the area, the basin geometry and isostasic calculations (Figs. 12 and S6; Supplementary information S5 and references therein). Below the ranges (e.g., below the Western Kunlun and Southern Tian Shan), we connected the major faults (e.g., the Karakax fault and Southern Tian Shan fault system) with well-documented offsets of the Moho (e.g., Jiang et al., 2004; Wittlinger et al., 2004; Li et al., 2007). However, in the centre of the basin, the deep geophysical data do not precisely constrain the Moho geometry below the Bachu and Tanan basement-cored uplifts, raising the question of where they root at depth (Fig. 12C). The involvement of the basement in these structures and their large wavelength (respectively ~150 km and ~50 km of width) suggest that they are large-scale structures that may be deeply rooted into the middle crust, the base of the crust or into the mantle (Fig. 13).

Such large foreland basement-cored uplifts exist in other orogenic systems (e.g., Himalayas, Laramides, Andes, Alps, etc.), where their rooting depth has also been discussed and investigated (e.g., Lacombe and Mouthereau, 2002; Yin et al., 2010; Yeck et al., 2014; Yonkee and Weil, 2015; Lacombe and Bellahsen, 2016). Usually, these structures are interpreted as developing above a mid-crustal decollement level (e.g., Lacombe and Mouthereau, 2002; Yeck et al., 2014; Yonkee and Weil, 2015; Lacombe and Bellahsen, 2016). Based on these other case examples and on the rheology of the local continental lithosphere (Fig. 12C), we thus propose that the Bachu and Tanan uplifts also root into a decollement level within the crust (Fig. 13A and 13B). Indeed, some geophysical interpretations (yield strength profiles and earthquake frequency at depth) suggest the existence of two possible decollement levels below the Tarim Basin, in the middle and at the base of the crust (Fig. 12C) (Sloan et al., 2011; Zhang et al., 2013b; Liu et al., 2015b; Chang et al., 2016b; Deng and Tesauro, 2016). The Bachu and Tanan uplifts may therefore deform above one of these crustal decollements (Fig. 13A and 13B). The main northward structural vergency of these basement highs would then indicate that the activated

1732 decollement transfers deformation from the northern edge of the Tibetan Plateau to the centre of
1733 the basin.
1734 However, in the Himalayan system, the Shillong Plateau is a foreland basement-cored
1735 uplift that may root into the mantle, as suggested by underlying possible Moho offsets (Yin et al.,
1736 2010). To investigate this possibility for the Bachu and Tanan basement uplifts, new deep
1737 geophysical data are necessary to specifically constrain the local Moho geometry. Indeed,
1738 accurate geophysical images of these areas are still lacking (e.g., Fig. 3 of Wittlinger et al.,
1739 2004). Nevertheless, rooting these structures directly into the mantle raises the problem of the
1740 foreland-ward transfer of the deformation associated with the Moho offset imaged below the
1741 outer range of the Western Kunlun (Wittlinger et al., 2004) (Fig. 13C). Consequently, we favor
1742 our previous interpretations of a crustal decollement level below the Tarim.
1743 These interpretations imply a decoupling between the deforming crust and an underlying
1744 rigid mantle. This is in agreement with the tomographic studies proposing a cold and rigid
1745 mantle below the basin (Deng and Tesauro, 2016; Deng et al., 2017). Moreover, the deformation
1746 pattern of the Tarim block can be compared with results of experimental models studying the
1747 influence of the depth of a rigid lithospheric heterogeneity on continental deformation
1748 (Calignano et al., 2015). Indeed, the deformation localization around the Tarim Basin and the
1749 associated flexures are in agreement with models simulating a strong upper mantle (Figs. 5, 8c
1750 and 9b of Calignano et al., 2015). Therefore, the geological, geophysical and experimental
1751 observations all suggest that the rigidity of the Tarim block is supported by the mantle, while
1752 deformation is transmitted above a crustal decollement below the Tarim Basin, from the Tibetan
1753 Plateau to the Tian Shan and further north.
1754
1755 **10. Conclusion**
1756
1757 On the basis of a structural map and of four balanced geological transects, we
1758 characterized the Cenozoic deformation across the Tarim Basin and the surrounding ranges.
1759 From structural restorations and crustal budgets, we also quantified the compressive component
1760 of this deformation. This comprehensive study thus provides a consistent regional overview of
1761 how the Tarim block participates to the Cenozoic deformation of Asia.

To the west, up to 83 ± 23 and 54 +24/-18 km of total crustal shortening is accommodated across the Western Kunlun and Southwestern Tian Shan compressive systems, respectively. On the other hand, to the east, only up to 38 ± 18 and 15 +20/-15 km of total crustal shortening is accommodated across the Altyn Tagh and Southeastern Tian Shan transpressive systems, respectively. The crustal shortening is therefore higher in the thrust wedges to the west, than in the strike-slip ones to the east. Accordingly, continental subduction is plausible below the Western Kunlun Range, whereas it seems unlikely below the Altyn Tagh.

Most of this Cenozoic compressive deformation of the Tarim block (from ~94% to 100%) is concentrated within the surrounding ranges. Indeed, a shortening of up to 78 ± 23 km (with ~30 km in the outer range only) is accommodated in the Western Kunlun Range, 54 +24/-18 km (~36 in the outer range) in the Southwestern Tian Shan, 38 ± 18 km (~0.3 in the outer range) in the Altyn Tagh Range, and 15 +20/-15 km (~0 km in the outer range) in the Southeastern Tian Shan. In spite of an overall flat topography due to an important sediment filling, a non-negligible amount of compressive deformation is also accommodated within the Tarim Basin by large basement-cored uplifts with a vergence synthetic to the deformation of the Tibetan Plateau edge. To the west, the Bachu uplift absorbs ~6% (~5 km) of the total crustal shortening of the Western Kunlun compressive system. To the south, the Tanan uplift accumulates ~1.5% (~0.6 km) of the total crustal shortening of the Altyn Tagh transpressive system. Strike-slip deformation may have also occurred on the bordering faults of these uplifts, but these displacements still need to be quantified. Consequently, the Tarim block, including its central part occupied by the present-day Tarim Basin, does not correspond to a totally rigid and undeformable heterogeneity within the Asian compressive system.

In the ranges around the Tarim Basin, thin-skinned structures neo-formed during the Cenozoic orogeny accommodate a significant fraction of the compressive deformation (up to ~66.7%). However, the main part of the deformation (from ~33.3% to 100 %) is rather accommodated by reactivated thick-skinned structures inherited from the Protero-Paleozoic history of the Tarim block. The structural inheritance thus appears to be at least as important as the stress boundary conditions or the lithospheric rheology in controlling the Cenozoic deformation of the Tarim area.

Finally, in the centre of the basin, the Bachu and Tanan uplifts probably root into a deep crustal decollement level. This decollement implies decoupling between the deforming crust and

an underlying rigid mantle, in agreement with the geological and geophysical data available in the region, and in line with experimental observations. Therefore, the rigidity of the Tarim block seems to be supported by the mantle, while deformation is transmitted above a decollement in the crust from the Tibetan Plateau to the Tian Shan and further north.

Acknowledgments

The study presented here was conducted with research grants from the CNRS-INSU RELIEF (M.S.) and SYSTER (L.B.) programs, the IPGP BQR program (M.S.), and the China Geological Survey grant DD20160022 (H.L.). A.L. and T.C. benefitted from a PhD grant from the French Ministry of Research and Higher Education (MESR). The seismic and well data used for this study are a courtesy of the Sinopec Group of the China Petrochemical Corporation. Yves Gaudemer (Institut de Physique du Globe de Paris, Université de Paris), Nicolas Bellahsen (Institut des Sciences de la Terre de Paris, Sorbonne Université), and Jing Liu (Institute of Geophysics, China Earthquake Administration) are thanked for thorough discussions. Finally, we are grateful to Guillaume Dupont-Nivet and an anonymous reviewer, as well as to the editor Douwe van Hinsbergen, for their critical and constructive comments and suggestions. This is IPGP contribution #3986. This study contributes to the IdEx Université de Paris ANR-18-IDEX-0001.

References

Alexeiev, D.V., Biske, Y.S., Wang, B., Djenchuraeva, A.V., Getman, O.F., Aristov, V.A., Krôner, A., Liu, H., Zhong, L., 2015. Tectono-Stratigraphic framework and Palaeozoic evolution of the Chinese South Tianshan. Geotectonics 49, 93–122. doi:10.1134/S0016852115020028

Allen, M.B., Windley, B.F., Zhang, C., Guo, J., 1993. Evolution of the Turfan Basin, Chinese Central Asia. Tectonics 12, 889–896. doi:10.1029/93TC00598

Allen, M.B., Windley, B.F., Zhang, C., 1994. Cenozoic tectonics in the Urumqi-Korla region of the Chinese Tien Shan. In: Giese, P., Behrmann, J. (Eds.), Active Continental Margins — Present and Past. Springer, Berlin, Heidelberg, Berlin, Heidelberg, pp. 406–416.

1825 doi:10.1007/978-3-662-38521-0_15
1826 Allen, M.B., Vincent, S.J., Wheeler, P.J., 1999. Late Cenozoic tectonics of the Kepingtage thrust
1827 zone: Interactions of the Tien Shan and Tarim Basin, northwest China. Tectonics 18, 639–
1828 654. doi:10.1029/1999TC900019
1829 Arnaud, N., Tapponnier, P., Roger, F., Brunel, M., Scharer, U., Wen, C., Zhiqin, X., 2003.
1830 Evidence for Mesozoic shear along the western Kunlun and Altyn-Tagh fault, northern Tibet
1831 (China). Journal of Geophysical Research: Solid Earth 108, 2053.
1832 doi:10.1029/2001JB000904
1833 Avouac, J.-P., Peltzer, G., 1993. Active tectonics in southern Xinjiang, China: Analysis of
1834 terrace riser and normal fault scarp degradation along the Hotan-Qira Fault System. Journal
1835 of Geophysical Research: Solid Earth 98, 21773–21807. doi:10.1029/93JB02172
1836 Avouac, J.-P., Tapponnier, P., 1993. Kinematic model of active deformation in central Asia.
1837 Geophysical Research Letters 20, 895–898. doi:10.1029/93GL00128
1838 Avouac, J.P., Tapponnier, P., Bai, M., You, H., Wang, G., 1993. Active thrusting and folding
1839 along the northern Tien Shan and Late Cenozoic rotation of the Tarim relative to Dzungaria
1840 and Kazakhstan. Journal of Geophysical Research: Solid Earth 98, 6755–6804.
1841 doi:10.1029/92JB01963
1842 Bande, A., Radjabov, S., Sobel, E.R., Sim, T., 2017a. Cenozoic palaeoenvironmental and
1843 tectonic controls on the evolution of the northern Fergana Basin. Geological Society,
1844 London, Special Publications 427, 313–335. doi:10.1144/SP427.12
1845 Bande, A., Sobel, E.R., Mikolaichuk, A., Torres Acosta, V., 2017b. Talas-Fergana Fault
1846 Cenozoic timing of deformation and its relation to Pamir indentation. Geological Society,
1847 London, Special Publications 427, 295–311. doi:10.1144/SP427.1
1848 Bershaw, J., Garzione, C.N., Schoenbohm, L., Gehrels, G., Tao, L., 2012. Cenozoic evolution of
1849 the Pamir plateau based on stratigraphy, zircon provenance, and stable isotopes of foreland
1850 basin sediments at Oytag (Wuyitake) in the Tarim Basin (west China). Journal of Asian
1851 Earth Sciences 44, 136–148. doi:10.1016/j.jseaes.2011.04.020
1852 Blayney, T., Najman, Y., Dupont-Nivet, G., Carter, A., Millar, I., Garzanti, E., Sobel, E.R.,
1853 Rittner, M., Ando, S., Guo, Z., Vezzoli, G., 2016. Indentation of the Pamirs with respect to
1854 the northern margin of Tibet: Constraints from the Tarim basin sedimentary record.
1855 Tectonics 35, 2345–2369. doi:10.1002/(ISSN)1944-9194

1856 Blayney, T., Dupont-Nivet, G., Najman, Y., Proust, J.-N., Meijer, N., Roperch, P., Sobel, E.R.,
1857 Millar, I., Guo, Z., 2019. Tectonic Evolution of the Pamir Recorded in the Western Tarim
1858 Basin (China): Sedimentologic and Magnetostratigraphic Analyses of the Aertashi Section.
1859 Tectonics 98, 6755–24. doi:10.1029/2018TC005146
1860 Bosboom, R.E., Dupont-Nivet, G., Houben, A.J.P., Brinkhuis, H., Villa, G., Mandic, O., Stoica,
1861 M., Zachariasse, W.J., Guo, Z., Li, C., Krijgsman, W., 2011. Late Eocene sea retreat from
1862 the Tarim Basin (west China) and concomitant Asian paleoenvironmental change.
1863 Palaeogeography, Palaeoclimatology, Palaeoecology 299, 385–398.
1864 doi:10.1016/j.palaeo.2010.11.019
1865 Bosboom, R.E., Dupont-Nivet, G., Grothe, A., Brinkhuis, H., Villa, G., Mandic, O., Stoica, M.,
1866 Huang, W., Yang, W., Guo, Z., Krijgsman, W., 2014a. Linking Tarim Basin sea retreat (west
1867 China) and Asian aridification in the late Eocene. Basin Research 26, 621–640.
1868 doi:10.1111/bre.12054
1869 Bosboom, R.E., Dupont-Nivet, G., Grothe, A., Brinkhuis, H., Villa, G., Mandic, O., Stoica, M.,
1870 Kouwenhoven, T., Huang, W., Yang, W., Guo, Z., 2014b. Timing, cause and impact of the
1871 late Eocene stepwise sea retreat from the Tarim Basin (west China). Palaeogeography,
1872 Palaeoclimatology, Palaeoecology 403, 101–118. doi:10.1016/j.palaeo.2014.03.035
1873 Bosboom, R.E., Mandic, O., Dupont-Nivet, G., Proust, J.-N., Ormukov, C., Aminov, J., 2017.
1874 Late Eocene palaeogeography of the proto-Paratethys Sea in Central Asia (NW China,
1875 southern Kyrgyzstan and SW Tajikistan). Geological Society, London, Special Publications
1876 427, 565–588. doi:10.1144/SP427.11
1877 Brunel, M., Arnaud, N., Tapponnier, P., Pan, Y., Wang, Y., 1994. Kongur Shan normal fault:
1878 Type example of mountain building assisted by extension (Karakoram fault, eastern Pamir).
1879 Geology 22, 707–4. doi:10.1130/0091-7613(1994)022<0707:KSNFTE>2.3.CO;2
1880 Burchfiel, B.C., Brown, E.T., Deng, Q., Feng, X., Li, J., Molnar, P., Molnar, P., Shi, J., Wu, Z.,
1881 You, H., 1999. Crustal shortening on the margins of the Tien Shan, Xinjiang, China.
1882 International Geology Review 41, 665–700. doi:10.1080/00206819909465164
1883 Burg, J.P., Davy, P., Martinod, J., 1994. Shortening of analogue models of the continental
1884 lithosphere: New hypothesis for the formation of the Tibetan plateau. Tectonics 13, 475–
1885 483. doi:10.1029/93TC02738
1886 Burkhard, M., Sommaruga, A., 1998. Evolution of the western Swiss Molasse basin: structural

relations with the Alps and the Jura belt. Geological Society, London, Special Publications 134: 279–298. doi:10.1144/GSL.SP.1998.134.01.13

Buslov, M.M., De Grave, J., Bataleva, E.A.V., Batalev, V.Y., 2007. Cenozoic tectonic and geodynamic evolution of the Kyrgyz Tien Shan Mountains: A review of geological, thermochronological and geophysical data. Journal of Asian Earth Sciences 29, 205–214. doi:10.1016/j.jseaes.2006.07.001

Cai, Z., Xu, Z., Yu, S., Li, S., He, B., Ma, X., Chen, X., Xu, X., 2018. Neoarchean magmatism and implications for crustal growth and evolution of the Kuluketage region, northeastern Tarim Craton. Precambrian Research 304, 156–170. doi:10.1016/j.precamres.2017.11.016

Calignano, E., Sokoutis, D., Willingshofer, E., Gueydan, F., Cloetingh, S., 2015. Strain localization at the margins of strong lithospheric domains: Insights from analog models. Tectonics 34, 396–412. doi:10.1002/2014TC003756

Cao, K., Wang, G.-C., van der Beek, P., Bernet, M., Zhang, K.-X., 2013. Cenozoic thermo-tectonic evolution of the northeastern Pamir revealed by zircon and apatite fission-track thermochronology. Tectonophysics 589, 17–32. doi:10.1016/j.tecto.2012.12.038

Cao, K., Xu, Y., Wang, G., Zhang, K., van der Beek, P., Wang, C., Jiang, S., Bershaw, J., 2014. Neogene Source-to-Sink Relations between the Pamir and Tarim Basin: Insights from Stratigraphy, Detrital Zircon Geochronology, and Whole-Rock Geochemistry. The Journal of Geology 122, 433–454. doi:10.1086/676478

Cao, K., Wang, G.-C., Bernet, M., van der Beek, P., Zhang, K.-X., 2015. Exhumation history of the West Kunlun Mountains, northwestern Tibet: Evidence for a long-lived, rejuvenated orogen. Earth and Planetary Science Letters 432, 391–403. doi:10.1016/j.epsl.2015.10.033

Carroll, A.R., Graham, S.A., Hendrix, M.S., Ying, D., Zhou, D., 1995. Late Paleozoic tectonic amalgamation of northwestern China: Sedimentary record of the northern Tarim, northwestern Turpan, and southern Junggar Basins. Geological Society of America Bulletin 107, 571–594. doi:10.1130/0016-7606(1995)107<0571:LPTAON>2.3.CO;2

Carroll, A.R., Graham, S.A., Chang, E.Z., McKnight, C., 2001. Sinian through Permian tectonostratigraphic evolution of the northwestern Tarim basin, China. In: Hendrix, M.S., Davis, G.A. (Eds.), Paleozoic and Mesozoic Tectonic Evolution of Central Asia. Geological Society of America Memoir 194, pp. 47–69.

Casas, A.M., Gapais, D., Nalpas, T., Besnard, K., Román-Berdiel, T., 2001. Analogue models of

transpressive systems. Journal of Structural Geology 23, 733–743. doi:10.1016/S0191-8141(00)00153-X

Chang, H., An, Z., Liu, W., Qiang, X., Song, Y., Ao, H., 2012a. Magnetostratigraphic and paleoenvironmental records for a Late Cenozoic sedimentary sequence drilled from Lop Nor in the eastern Tarim Basin. Global and Planetary Change 80-81, 113–122. doi:10.1016/j.gloplacha.2011.09.008

Chang, J., Qiu, N., Li, J., 2012b. Tectono-thermal evolution of the northwestern edge of the Tarim Basin in China: Constraints from apatite (U-Th)/He thermochronology. Journal of Asian Earth Sciences 61, 187–198. doi:10.1016/j.jseaes.2012.09.020

Chang, H., An, Z., Liu, W., Ao, H., Qiang, X., Song, Y., Lai, Z., 2014a. Quaternary structural partitioning within the rigid Tarim plate inferred from magnetostratigraphy and sedimentation rate in the eastern Tarim Basin in China. Quaternary Research 81, 424–432. doi:10.1016/j.yqres.2013.10.018

Chang, J., Brown, R.W., Yuan, W., Li, W., Que, Y., Qiu, N., 2014b. Mesozoic cooling history of the "Bachu Uplift‘’ in the Tarim Basin, China: Constraints from zircon fission-track thermochronology. Radiation Measurements 67, 5–14. doi:10.1016/j.radmeas.2014.05.019

Chang, J., Qiu, N., Song, X., Li, H., 2016a. Multiple cooling episodes in the Central Tarim (Northwest China) revealed by apatite fission track analysis and vitrinite reflectance data. International Journal of Earth Sciences 105, 1257–1272. doi:10.1007/s00531-015-1242-7

Chang, J., Qiu, N., Xu, W., 2016b. Thermal regime of the Tarim Basin, Northwest China: a review. International Geology Review 59, 45–61. doi:10.1080/00206814.2016.1210546

Chang, J., Tian, Y., Qiu, N., 2017. Mid-Late Miocene deformation of the northern Kuqa fold-and-thrust belt (southern Chinese Tian Shan): An apatite (U-Th-Sm)/He study. Tectonophysics 694, 101–113. doi:10.1016/j.tecto.2016.12.003

Charreau, J., Gilder, S., Chen, Y., Dominguez, S., Avouac, J.-P., Sen, S., Jolivet, M., Li, Y., Wang, W., 2006. Magnetostratigraphy of the Yaha section, Tarim Basin (China): 11 Ma acceleration in erosion and uplift of the Tian Shan mountains. Geology 34, 181–184. doi:10.1130/G22106.1

Charreau, J., Gumiaux, C., Avouac, J.-P., Augier, R., Chen, Y., Barrier, L., Gilder, S., Dominguez, S., Charles, N., Wang, Q., 2009. The Neogene Xiyu Formation, a diachronous prograding gravel wedge at front of the Tianshan: Climatic and tectonic implications. Earth

and Planetary Science Letters 287, 298–310. doi:10.1016/j.epsl.2009.07.035

Charvet, J., Shu, L.S., Laurent-Charvet, S., 2007. Paleozoic structural and geodynamic evolution of eastern Tianshan (NW China): welding of the Tarim and Junggar plates. Episodes Journal of International Geoscience 30, 162–186.

Charvet, J., Shu, L., Laurent-Charvet, S., Wang, B., Faure, M., Cluzel, D., Chen, Y., De Jong, K., 2011. Palaeozoic tectonic evolution of the Tianshan belt, NW China. Science China Earth Sciences 54, 166–184. doi:10.1007/s11430-010-4138-1

Chen, Y., Cogné, J.P., Courtillot, V., Avouac, J.-P., Tapponnier, P., Wang, G., Bai, M., You, H., Li, M., Wei, C., Buffetaut, E., 1991. Paleomagnetic study of Mesozoic continental sediments along the northern Tien Shan (China) and heterogeneous strain in central Asia. Journal of Geophysical Research: Solid Earth 96, 4065–4082. doi:10.1029/90JB02699

Chen, X., An, Y., Gehrels, G.E., Cowgill, E.S., Grove, M., Harrison, T.M., Wang, X.-F., 2003. Two phases of Mesozoic north-south extension in the eastern Altyn Tagh range, northern Tibetan Plateau. Tectonics 22, 1053. doi:10.1029/2001TC001336

Chen, Z.Q., Shi, G.R., 2003. Late Paleozoic depositional history of the Tarim basin, northwest China: An integration of biostratigraphic and lithostratigraphic constraints. American Association of Petroleum Geologists Bulletin 87, 1323–1354. doi:10.1306/0401032001115

Chen, S., Tang, L., Jin, Z., Jia, C., Pi, X., 2004. Thrust and fold tectonics and the role of evaporites in deformation in the Western Kuqa Foreland of Tarim Basin, Northwest China. Marine and Petroleum Geology 21, 1027–1042. doi:10.1016/j.marpetgeo.2004.01.008

Chen, X., Chen, H., Lin, X., Cheng, X., Yang, R., Ding, W., Gong, J., Wu, L., Zhang, F., Chen, S., Zhang, Y., Yan, J., 2018. Arcuate Pamir in the Paleogene? Insights from a review of stratigraphy and sedimentology of the basin fills in the foreland of NE Chinese Pamir, western Tarim Basin. Earth Science Reviews 180, 1–16. doi:10.1016/j.earscirev.2018.03.003

Cheng, F., Guo, Z., Jenkins, H.S., Fu, S., Cheng, X., 2015. Initial rupture and displacement on the Altyn Tagh fault, northern Tibetan Plateau: Constraints based on residual Mesozoic to Cenozoic strata in the western Qaidam Basin. Geosphere 11, 921–942. doi:10.1130/GES01070.1

Cheng, F., Jolivet, M., Fu, S., Zhang, C., Zhang, Q., Guo, Z., 2016a. Large-scale displacement along the Altyn Tagh Fault (North Tibet) since its Eocene initiation: Insight from detrital zircon U–Pb geochronology and subsurface data. Tectonophysics 677-678, 261–279.

1980 doi:10.1016/j.tecto.2016.04.023
1981 Cheng, X., Chen, H., Lin, X., Yang, S., Chen, S., Zhang, F., Li, K., Liu, Z., 2016b. Deformation
1982 geometry and timing of the Wupoer thrust belt in the NE Pamir and its tectonic implications.
1983 Frontiers in Earth Sciences 1–10. doi:10.1007/s11707-016-0606-z
1984 Cheng, X., Chen, H., Lin, X., Wu, L., Gong, J., 2017. Geometry and Kinematic Evolution of the
1985 Hotan-Tiklik Segment of the Western Kunlun Thrust Belt: Constrained by Structural
1986 Analyses and Apatite Fission Track Thermochronology. The Journal of Geology 125, 65–82.
1987 doi:10.1086/689187
1988 Clark, M.K., Royden, L.H., Whipple, K.X., Burchfiel, B.C., Zhang, X., Tang, W., 2006. Use of a
1989 regional, relict landscape to measure vertical deformation of the eastern Tibetan Plateau.
1990 Journal of Geophysical Research 111, 1–23. doi:10.1029/2005JF000294
1991 Coutand, I., Barrier, L., Govin, G., Grujic, D., Hoorn, C., Dupont-Nivet, G., Najman, Y., 2016.
1992 Late Miocene-Pleistocene evolution of India-Eurasia convergence partitioning between the
1993 Bhutan Himalaya and the Shillong Plateau: New evidences from foreland basin deposits
1994 along the Dungsam Chu section, eastern Bhutan. Tectonics 35, 2963–2994.
1995 doi:10.1002/2016TC004258
1996 Cowgill, E., An, Y., Xiao-Feng, W., Zhang, Q., 2000. Is the North Altyn fault part of a strike-slip
1997 duplex along the Altyn Tagh fault system? Geology 28, 255–258. doi:10.1130/0091-
1998 7613(2000)28<255:ITNAFP>2.0.CO;2
1999 Cowgill, E., An, Y., Harrison, T.M., Xiao-Feng, W., 2003. Reconstruction of the Altyn Tagh
2000 fault based on U-Pb geochronology: Role of back thrusts, mantle sutures, and heterogeneous
2001 crustal strength in forming the Tibetan Plateau. Journal of Geophysical Research 108, 2346.
2002 doi:10.1029/2002JB002080
2003 Cowgill, E., 2010. Cenozoic right-slip faulting along the eastern margin of the Pamir salient,
2004 northwestern China. Geological Society of America Bulletin 122, 145–161.
2005 doi:10.1130/B26520.1
2006 Craig, T.J., Copley, A., Jackson, J., 2012. Thermal and tectonic consequences of India
2007 underthrusting Tibet. Earth and Planetary Science Letters 353-354, 231–239.
2008 doi:10.1016/j.epsl.2012.07.010
2009 Dahlstrom, C.D.A., 1969. Balanced cross sections. Canadian Journal of Earth Sciences 6, 743–
2010 757. doi:10.1139/e69-069

2011 Daout, S., Doin, M.-P., Peltzer, G., Lasserre, C., Socquet, A., Volat, M., Sudhaus, H., 2018.
2012 Strain partitioning and present-day fault kinematics in NW Tibet from SAR interferometry.
2013 Journal of Geophysical Research: Solid Earth 123, 2462–2483. doi:10.1002/2017JB015020
2014 Davy, P., Cobbold, P.R., 1988. Indentation tectonics in nature and experiment. 1. Experiments
2015 scaled for gravity. Bulletin of the Geological Institute of Uppsala 14, 129–141.
2016 Dayem, K.E., Molnar, P., Clark, M.K., Houseman, G.A., 2009. Far-field lithospheric
2017 deformation in Tibet during continental collision. Tectonics 28, 1–9.
2018 doi:10.1029/2008TC002344
2019 De Grave, J., Buslov, M.M., Van den haute, P., 2007. Distant effects of India–Eurasia
2020 convergence and Mesozoic intracontinental deformation in Central Asia: Constraints from
2021 apatite fission-track thermochronology. Journal of Asian Earth Sciences 29, 188–204.
2022 doi:10.1016/j.jseaes.2006.03.001
2023 DeCelles, P.G., Giles, K.A., 1996. Foreland basin systems. Basin Research 8, 105–123.
2024 doi:10.1046/j.1365-2117.1996.01491.x
2025 DeCelles, P.G., Kapp, P., Ding, L., Gehrels, G.E., 2007. Late Cretaceous to middle Tertiary
2026 basin evolution in the central Tibetan Plateau: Changing environments in response to
2027 tectonic partitioning, aridification, and regional elevation gain. Geological Society of
2028 America Bulletin 119, 654–680. doi:10.1130/B26074.1
2029 Deng, Y., Tesauro, M., 2016. Lithospheric strength variations in Mainland China: Tectonic
2030 implications. Tectonics 35, 2313–2333. doi:doi.org/0.1002/2016TC004272
2031 Deng, Y., Levandowski, W., Kusky, T., 2017. Lithospheric density structure beneath the Tarim
2032 basin and surroundings, northwestern China, from the joint inversion of gravity and
2033 topography. Earth and Planetary Science Letters 460, 244–254.
2034 doi:10.1016/j.epsl.2016.10.051
2035 Ding, G., Chen, J., Tian, Q., Shen, X., Xing, C., Wei, K., 2004. Active faults and magnitudes of
2036 left-lateral displacement along the northern margin of the Tibetan Plateau. Tectonophysics
2037 380, 243–260. doi:10.1016/j.tecto.2003.09.022
2038 Dong, S., Li, Z., Jiang, L., 2016. The early Paleozoic sedimentary–tectonic evolution of the
2039 circum-Mangar areas, Tarim block, NW China: Constraints from integrated detrital records.
2040 Tectonophysics 682, 17–34. doi:10.1016/j.tecto.2016.05.047
2041 Dubille, M., Lavé, J., 2015. Rapid grain size coarsening at sandstone/conglomerate transition:

2042 similar expression in Himalayan modern rivers and Pliocene molasse deposits. Basin
2043 Research 27, 26–42. doi:10.1111/bre.12071
2044 Dumitru, T., Zhou, D., Chang, E., Graham, S., Hendrix, M., Sobel, E., Carroll, A., 2001. Uplift,
2045 exhumation, and deformation in the Chinese Tian Shan. In: Hendrix, M.S., Davis, G.A.
2046 (Eds.), Paleozoic and Mesozoic Tectonic Evolution of Central Asia. Geological Society of
2047 America Memoir 194, pp. 71–99.
2048 Elliott, D., 1983. The construction of balanced cross-sections. Journal of Structural Geology 5,
2049 101. doi:10.1016/0191-8141(83)90035-4
2050 England, P., Houseman, G., 1985. Role of lithospheric strength heterogeneities in the tectonics of
2051 Tibet and neighbouring regions. Nature 315, 297–301. doi:10.1038/315297a0
2052 Fan, Q., Lü, X., Yang, M., Xie, H., 2008. Influence of Salt Beds on the Segmentation of
2053 Structure and Hydrocarbon Accumulation in Qiulitag Structural Belt, Tarim Basin, China.
2054 Journal of China University of Geosciences 19, 162–173. doi:10.1016/S1002-
2055 0705(08)60035-7
2056 Fillon, C., Huismans, R.S., van der Beek, P., 2013. Syntectonic sedimentation effects on the
2057 growth of fold-and-thrust belts. Geology 41, 83–86. doi:10.1130/G33531.1
2058 Fu, B., Ninomiya, Y., Guo, J., 2010. Slip partitioning in the northeast Pamir–Tian Shan
2059 convergence zone. Tectonophysics 483, 344–364. doi:10.1016/j.tecto.2009.11.003
2060 Gao, J., Long, L., Klemd, R., Qian, Q., Liu, D., Xiong, X., Su, W., Liu, W., Wang, Y., Yang, F.,
2061 2009. Tectonic evolution of the South Tianshan orogen and adjacent regions, NW China:
2062 geochemical and age constraints of granitoid rocks. International Journal of Earth Sciences
2063 98, 1221–1238. doi:10.1007/s00531-008-0370-8
2064 Gao, R., Hou, H., Cai, X., Knapp, J.H., He, R., Liu, J., Xiong, X., Guan, Y., Li, W., Zeng, L.,
2065 Roecker, S.W., 2013. Fine crustal structure beneath the junction of the south-west Tian Shan
2066 and Tarim Basin, NW China. Lithosphere 5, 382–392. doi:10.1130/L248.1
2067 Gao, Z., Fan, T., 2014. Intra-platform tectono-sedimentary response to geodynamic transition
2068 along the margin of the Tarim Basin, NW China. Journal of Asian Earth Sciences 96, 178–
2069 193. doi:10.1016/j.jseaes.2014.08.023
2070 Ge, R., Zhu, W., Wu, H., Zheng, B., Zhu, X., He, J., 2012. The Paleozoic northern margin of the
2071 Tarim Craton: Passive or active? Lithos 142-143, 1–15. doi:10.1016/j.lithos.2012.02.010
2072 Gehrels, G.E., An, Y., Wang, X.-F., 2003. Magmatic history of the northeastern Tibetan Plateau.

2073 Journal of Geophysical Research: Solid Earth 108, 51–14. doi:10.1029/2002JB001876
2074 Glorie, S., De Grave, J., Buslov, M.M., Zhimulev, F.I., Stockli, D.F., Batalev, V.Y., Izmer, A.,
2075 Van den haute, P., Vanhaecke, F., Elburg, M.A., 2011. Tectonic history of the Kyrgyz South
2076 Tien Shan (Atbashi-Inylchek) suture zone: The role of inherited structures during
2077 deformation-propagation. Tectonics 30, 1–23. doi:10.1029/2011TC002949
2078 Gourbet, L., Mahéo, G., Leloup, P.H., Paquette, J.L., Sorrel, P., Henriquet, M., Liu, X., Liu, X.,
2079 2015. Western Tibet relief evolution since the Oligo-Miocene. Gondwana Research 41, 425–
2080 437. doi:10.1016/j.gr.2014.12.003
2081 Guilbaud, C., Simoes, M., Barrier, L., Barrier, L., Laborde, A., Van der Woerd, J., Haibing, L.,
2082 Tapponnier, P., Coudroy, T., Murray, A., 2017. Kinematics of active deformation across the
2083 Western Kunlun mountain range (Xinjiang, China), and potential seismic hazards within the
2084 southern Tarim Basin. Journal of Geophysical Research: Solid Earth 122, 10–398–10–4226.
2085 doi:10.1002/2017JB014069
2086 Guillot, S., Garzanti, E., Baratoux, D., Marquer, D., Mahéo, G., de Sigoyer, J., 2003.
2087 Reconstructing the total shortening history of the NW Himalaya. Geochemistry Geophysics
2088 Geosystems 4, 1–22. doi:10.1029/2002GC000484
2089 Guo, Z.J., An, Y., Robinson, A., Jia, C.-Z., 2005. Geochronology and geochemistry of deep-
2090 drill-core samples from the basement of the central Tarim basin. Journal of Asian Earth
2091 Sciences 25, 45–56. doi:10.1016/j.jseaes.2004.01.016
2092 Guo, F., Yang, D., Eriksson, K.A., Guo, L., 2015. Paleoenvironments, stratigraphic evolution
2093 and reservoir characteristics of the Upper Cretaceous Yingjisha Group, southwest Tarim
2094 Basin. Marine and Petroleum Geology 67, 336–355. doi:10.1016/j.marpetgeo.2015.05.023
2095 Guo, Y., Tang, L., Yu, T.-X., Lu, J.-M., Yue, Y., 2016. Structural characteristics and petroleum
2096 geological significances of Mazhatage Fault Belt in Tarim Basin. Journal of Earth Sciences
2097 and Environment 38, 104–114. doi:1672-6561(2016)01-0104-11
2098 Han, Y., Zhao, G., Sun, M., Eizenhöfer, P.R., Hou, W., Zhang, X., Liu, Q., Wang, B., Liu, D.,
2099 Xu, B., 2016. Late Paleozoic subduction and collision processes during the amalgamation of
2100 the Central Asian Orogenic Belt along the South Tianshan suture zone. Lithos 246-247, 1–
2101 12. doi:10.1016/j.lithos.2015.12.016
2102 Hatcher, R.D., Jr, 2004. Properties of Thrusts and Upper Bounds for the Size of Thrust Sheets.
2103 In: McClay, K.R. (Ed.), Thrust Tectonics and Hydrocarbon Systems. American Association

of Petroleum Geologists Memoir 82, pp. 18–29.

He, D., Suppe, J., Geng, Y., Guan, S., Huang, S., Shi, X., Wang, X., Zhang, C., 2005. Guidebook for field trip in south and north Tianshan foreland basin, Xinjiang Uygur Autonomous Region, China. Guidebook, 78 p.

He, B., Jiao, C., Xu, Z., Cai, Z., Zhang, J., Liu, S., Li, H., Chen, W., Yu, Z., 2016. The paleotectonic and paleogeography reconstructions of the Tarim Basin and its adjacent areas (NW China) during the late Early and Middle Paleozoic. Gondwana Research 30, 191–206. doi:10.1016/j.gr.2015.09.011

Heermance, R.V., Chen, J., Burbank, D.W., Wang, C., 2007. Chronology and tectonic controls of Late Tertiary deposition in the southwestern Tian Shan foreland, NW China. Basin Research 19, 599–632. doi:10.1111/j.1365-2117.2007.00339.x

Heermance, R.V., Chen, J., Burbank, D.W., Miao, J., 2008. Temporal constraints and pulsed Late Cenozoic deformation during the structural disruption of the active Kashi foreland, northwest China. Tectonics 27. doi:10.1029/2007TC002226

Hendrix, M.S., Graham, S.A., Carroll, A.R., Sobel, E.R., McKnight, C.L., Schulein, B.J., Wang, Z., 1992. Sedimentary record and climatic implications of recurrent deformation in the Tian Shan: Evidence from Mesozoic strata of the north Tarim, south Junggar, and Turpan basins, northwest China. Geological Society of America Bulletin 104, 53–79. doi:10.1130/0016-7606(1992)104<0053:SRACIO>2.3.CO;2

Hendrix, M.S., Dumitru, T.A., Graham, S.A., 1994. Late Oligocene-early Miocene unroofing in the Chinese Tian Shan: An early effect of the India-Asia collision. Geology 22, 487–490. doi:10.1130/0091-7613(1994)022<0487:LOEMUI>2.3.CO;2

Hossack, J.R., 1979. The use of balanced cross-sections in the calculation of orogenic contraction: A review. Journal of the Geological Society 136, 705–711. doi:10.1144/gsjgs.136.6.0705

Huang, B., Piper, J.D.A., Peng, S., Liu, T., Li, Z., Wang, Q., Zhu, R., 2006. Magnetostratigraphic study of the Kuche Depression, Tarim Basin, and Cenozoic uplift of the Tian Shan Range, Western China. Earth and Planetary Science Letters 251, 346–364. doi:10.1016/j.epsl.2006.09.020

Huang, B., Piper, J.D.A., Qiao, Q., Wang, H., Zhang, C., 2010. Magnetostratigraphic and rock magnetic study of the Neogene upper Yaha section, Kuche Depression (Tarim Basin):

Implications to formation of the Xiyu conglomerate formation, NW China. Journal of Geophysical Research 115, 62–17. doi:10.1029/2008JB006175

Hubert-Ferrari, A., Suppe, J., Gonzalez-Mieres, R., Wang, X., 2007. Mechanisms of active folding of the landscape (southern Tian Shan, China). Journal of Geophysical Research 112, 450–39. doi:10.1029/2006JB004362

Izquierdo-Llavall, E., Roca, E., Xie, H., Pla, O., Munoz, J.A., Rowan, M.G., Yuan, N., Huang, S., 2018. Influence of overlapping décollements, syntectonic sedimentation, and structural inheritance in the evolution of a contractional system: The Central Kuqa Fold-and-Thrust Belt (Tian Shan Mountains, NW China). Tectonics 37, 2608–2632. doi:10.1029/2017TC004928

Jia, D., Lu, H., Cai, D., Wu, S., Shi, Y., Chen, C., 1998. Structural Features of Northern Tarim Basin: Implications for Regional Tectonics and Petroleum Traps. American Association of Petroleum Geologists Bulletin 82, 147–159.

Jia, Y., Fu, B., Jolivet, M., Zheng, S., 2015. Cenozoic tectono-geomorphological growth of the SW Chinese Tian Shan: Insight from AFT and detrital zircon U-Pb data. Journal of Asian Earth Sciences 111, 395–413. doi:10.1016/j.jseaes.2015.06.023

Jiang, X., Jin, Y., McNutt, M.K., 2004. Lithospheric deformation beneath the Altyn Tagh and West Kunlun faults from recent gravity surveys. Journal of Geophysical Research 109, 1–14. doi:10.1029/2003JB002444

Jiang, X., Li, Z.-X., Li, H., 2013. Uplift of the West Kunlun Range, northern Tibetan Plateau, dominated by brittle thickening of the upper crust. Geology 41, 439–442. doi:10.1130/G33890.1

Jiang, X., Li, Zheng-Xiang, 2014. Seismic reflection data support episodic and simultaneous growth of the Tibetan Plateau since 25 Myr. Nature Communications 5, 1–7. doi:10.1038/ncomms6453

Jiang, Z., Jiang, S., Lan, X., Wang, B., Huang, S., Zhang, H., 2018. Neotectonic evolution of the Tarim Basin Craton from Neogene to quaternary. International Geology Review 60, 1213–1230. doi:10.1080/00206814.2017.1379365

Jin, X., Wang, J., Chen, B., Ren, L., 2003. Cenozoic depositional sequences in the piedmont of the west Kunlun and their paleogeographic and tectonic implications. Journal of Asian Earth Sciences 21, 755–765. doi:10.1016/S1367-9120(02)00073-1

Jin, Z., Yang, M., Lü, X., Sun, D., Tang, X., Peng, G., Lei, G., 2008. The tectonics and petroleum system of the Qiulitagh fold and thrust belt, northern Tarim basin, NW China. Marine and Petroleum Geology 25, 767–777. doi:10.1016/j.marpetgeo.2008.01.011

Jolivet, M., Roger, F., Arnaud, N., Brunel, M., Tapponnier, P., Seward, D., 1999. Histoire de l'exhumation de l'Altun Shan: indications sur l‘‘âge de la subduction du bloc du Tarim sous le système de l’’Altyn Tagh (Nord Tibet). Comptes Rendus de l'Académie des Sciences - Series IIA - Earth and Planetary Science 329, 749–755. doi:10.1016/S1251-8050(00)88495-5

Jolivet, M., Brunel, M., Seward, D., Xu, Z., Yang, J., Roger, F., Tapponnier, P., Malavieille, J., Arnaud, N., Wu, C., 2001. Mesozoic and Cenozoic tectonics of the northern edge of the Tibetan plateau: fission-track constraints. Tectonophysics 343, 111–134. doi:10.1016/S0040-1951(01)00196-2

Jolivet, M., Dominguez, S., Charreau, J., Chen, Y., Li, Y., Wang, Q., 2010. Mesozoic and Cenozoic tectonic history of the central Chinese Tian Shan: Reactivated tectonic structures and active deformation. Tectonics 29. doi:10.1029/2010TC002712

Jolivet, M., Heilbronn, G., Robin, C., Barrier, L., Bourquin, S., Guo, Z., Jia, Y., Guerit, L., Yang, W., Fu, B., 2013. Reconstructing the Late Palaeozoic - Mesozoic topographic evolution of the Chinese Tian Shan: available data and remaining uncertainties. Advances in Geosciences. 37, 7–18. doi:10.5194/adgeo-37-7-2013

Jolivet, M., 2017. Mesozoic tectonic and topographic evolution of Central Asia and Tibet: a preliminary synthesis. Geological Society, London, Special Publications 427, 19–55. doi:10.1144/SP427.2

Jolivet, M., Barrier, L., Dauteuil, O., Laborde, A., Li, Q., Reichenbacher, B., Popescu, S.-M., Sha, J., Guo, Z., 2018. Late Cretaceous–Palaeogene topography of the Chinese Tian Shan: New insights from geomorphology and sedimentology. Earth and Planetary Science Letters 499, 95–106. doi:10.1016/j.epsl.2018.07.004

Jourdon, A., Petit, C., Rolland, Y., Loury, C., Bellahsen, N., Guillot, S., Le Pourhiet, L., Ganino, C., 2017. New structural data on Late Paleozoic tectonics in the Kyrgyz Tien Shan (Central Asian Orogenic Belt). Gondwana Research 46, 57–78. doi:10.1016/j.gr.2017.03.004

Jun, G., Maosong, L., Xuchang, X., Yaoqing, T., Guoqi, H., 1998. Paleozoic tectonic evolution of the Tianshan Orogen, northwestern China. Tectonophysics 287, 213–231. doi:10.1016/S0040-1951(98)80070-X

Kaya, M.Y., Dupont-Nivet, G., Proust, J.N., Roperch, P., Bougeois, L., Meijer, N., Frieling, J., Fioroni, C., Özkan Altiner, S., Vardar, E., Barbolini, N., Stoica, M., Aminov, J., Mamtimin, M., Guo, Z., 2019. Paleogene evolution and demise of the proto-Paratethys Sea in Central Asia (Tarim and Tajik basins): Role of intensified tectonic activity at ca. 41 Ma. Basin Research 2019;00, 1-26. doi: 10.1111/bre.12330

Kent-Corson, M.L., Ritts, B.D., Zhuang, G., Bovet, P.M., Graham, S.A., Chamberlain, C.P., 2009. Stable isotopic constraints on the tectonic, topographic, and climatic evolution of the northern margin of the Tibetan Plateau. Earth and Planetary Science Letters 282, 158–166. doi:10.1016/j.epsl.2009.03.011

Lacombe, O., Mouthereau, F., 2002. Basement-involved shortening and deep detachment tectonics in forelands of orogens: Insights from recent collision belts (Taiwan, Western Alps, Pyrenees). Tectonics 21, 1–22. doi:10.1029/2001TC901018

Lacombe, O., Bellahsen, N., 2016. Thick-skinned tectonics and basement-involved fold–thrust belts: insights from selected Cenozoic orogens. Geological Magazine 153, 763–810. doi:10.1017/S0016756816000078

Lavé, J., Avouac, J.P., 2001. Fluvial incision and tectonic uplift across the Himalayas of central Nepal. Journal of Geophysical Research: Solid Earth 106, 26561–26591. doi:10.1029/2001JB000359

Lee, K.Y., 1985. Geology of the Tarim Basin with special emphasis on petroleum deposits, Xinjiang Uygur Zizhiqu, Northwest China (No. 85-616), United States Geological Survey Open-file Report 85-616, 55 p. doi:10.3133/ofr85616

Li, D.S., Liang, D., Jia, C., Wang, G., Wu, Q., Dengfa, 1996. Hydrocarbon accumulations in the Tarim Basin, China. American Association of Petroleum Geologists Bulletin 80, 1587–1603.

Li, H.B., Yang, J., Shi, R., Wu, C., Tapponnier, P., Wan, Y., Zhang, J., Meng, F., 2002a. Determination of the Altyn Tagh strike-slip fault basin and its relationship with mountains. Chinese Science Bulletin 47, 572–577. doi:10.1360/02tb9132

Li, Q.S., Gao, R., Lu, D., Li, J., Fan, J., Zhang, Z., Liu, W., Li, Y., Yan, Q., Li, D., 2002b. Tarim underthrust beneath western Kunlun: evidence from wide-angle seismic sounding. Journal of Asian Earth Sciences 20, 247–253. doi:10.1016/S1367-9120(01)00057-8

Li, Y, Liu, Q., Chen, J., Li, S., Guo, B., Lai, Y., 2007. Shear wave velocity structure of the crust and upper mantle underneath the Tianshan orogenic belt. Science in China Series D: Earth

Sciences 50, 321–330. doi:10.1007/s11430-007-0008-x

Li, S.Q., Wang, X., Suppe, J., 2012a. Compressional salt tectonics and synkinematic strata of the western Kuqa foreland basin, southern Tian Shan, China. Basin Research 24, 475–497. doi:10.1111/j.1365-2117.2011.00531.x

Li, T., Chen, J., Thompson, J.A., Burbank, D.W., Xiao, W., 2012b. Equivalency of geologic and geodetic rates in contractional orogens: New insights from the Pamir Frontal Thrust. Geophysical Research Letters 39, 450–6. doi:10.1029/2012GL051782

Li, T., Chen, J., Thompson, J.A., Burbank, D.W., Yang, X., 2013. Quantification of three-dimensional folding using fluvial terraces: A case study from the Mushi anticline, northern margin of the Chinese Pamir. Journal of Geophysical Research: Solid Earth 118, 4628–4647. doi:10.1002/jgrb.50316

Li, D.X., Yang, S., Chen, H., Cheng, X., Li, K., Jin, X., Li, Z., Li, Y., Zou, S., 2014a. Late Carboniferous crustal uplift of the Tarim plate and its constraints on the evolution of the Early Permian Tarim Large Igneous Province. Lithos 204, 36–46. doi:10.1016/j.lithos.2014.05.023

Li, J.F., Zhang, Z., Tang, W., Li, K., Luo, Z., Li, J., 2014b. Provenance of Oligocene-Miocene sediments in the Subei area, eastern Altyn Tagh fault and its geological implications: Evidence from detrital zircons LA-ICP-MS U-Pb chronology. Journal of Asian Earth Sciences 87, 130–140. doi:10.1016/j.jseaes.2014.02.015

Li, D., He, D., Tang, Y., Wu, X., Lian, Y., Yang, Y., 2015a. Dynamic processes from plate subduction to intracontinental deformation: Insights from the tectono-sedimentary evolution of the Zhaosu-Tekesi Depression in the southwestern Chinese Tianshan. Journal of Asian Earth Sciences 113, 728–747. doi:10.1016/j.jseaes.2015.09.007

Li, Y.L., Wang, C., Dai, J., Xu, G., Hou, Y., Li, X., 2015b. Propagation of the deformation and growth of the Tibetan-Himalayan orogen: A review. Earth Science Reviews 143, 36–61. doi:10.1016/j.earscirev.2015.01.001

Li, Y.J., Wen, L., Yang, H.-J., Zhang, G.-Y., Shi, J., Peng, G.-X., Hu, J.-F., Luo, J.-C., Huang, Z.-B., Chen, Y.-G., Zhang, Q., 2015c. New discovery and geological significance of Late Silurian-Carboniferous extensional structures in Tarim Basin. Journal of Asian Earth Sciences 98, 304–319. doi:10.1016/j.jseaes.2014.11.020

Li, Y.J., Zhang, Q., Zhang, G.-Y., Yang, H.-J., Yang, X.-Z., Shi, J., Neng, Y., Chen, Y.-G., Wen,

L., 2015d. Late Cenozoic transtensional fault belt discovered on the boundary of the Awati Sag in the northwestern Tarim Basin. International Journal of Earth Sciences 104, 1253–1265. doi:10.1007/s00531-015-1145-7

Li, J.Y., Zhang, J., Zhao, X., Jiang, M., Li, Y., Zhu, Z., Feng, Q., Wang, L., Sun, G., Liu, J., Yang, T., 2016a. Mantle Subduction and Uplift of Intracontinental Mountains: A Case Study from the Chinese Tianshan Mountains within Eurasia. Scientific Reports 6, 1–8. doi:10.1038/srep28831

Li, T., Chen, J., Fang, L., Chen, Z., Thompson, J.A., Jia, C., 2016b. The 2015 Mw 6.4 Pishan Earthquake: Seismic Hazards of an Active Blind Wedge Thrust System at the Western Kunlun Range Front, Northwest Tibetan Plateau. Seismological Research Letters 87, 601–608. doi:10.1785/0220150205

Li, Y.J., Wen, L., Li, H.-L., Peng, G.-X., Bin Qiu, Zheng, D.-M., Luo, J.-C., Zhang, Q., Jia, T.-G., 2016c. The Madong Early Paleozoic fold-thrust belt in southern Tarim Basin. Journal of Asian Earth Sciences 115, 247–256. doi:10.1016/j.jseaes.2015.10.007

Li, Y.J., Wen, L., Zhang, H.-A., Huang, T.-Z., Li, H.-L., Shi, Y.-Y., Meng, Q.-L., Peng, G.-X., Huang, S.-Y., Zhang, Q., 2016d. The Kuqa late Cenozoic fold–thrust belt on the southern flank of the Tian Shan Mountains. International Journal of Earth Sciences 105, 1417–1430. doi:10.1007/s00531-015-1262-3

Li, Y.J., Zhang, Q., Zhang, G.-Y., Tian, Z.-J., Peng, G.-X., Bin Qiu, Huang, Z.-B., Luo, J.-C., Wen, L., Zhao, Y., Jia, T.-G., 2016e. Cenozoic faults and faulting phases in the western Tarim Basin (NW China): Effects of the collisions on the southern margin of the Eurasian Plate. Journal of Asian Earth Sciences 132, 40–57. doi:10.1016/j.jseaes.2016.09.018

Li, S.Z., Zhao, S., Liu, X., Cao, H., Yu, S., Li, X., Somerville, I., Yu, S., Suo, Y., 2018a. Closure of the Proto-Tethys Ocean and Early Paleozoic amalgamation of microcontinental blocks in East Asia. Earth Science Reviews 186, 37–75. doi:10.1016/j.earscirev.2017.01.011

Li, T., Chen, J., Thompson Jobe, J.A., Burbank, D.W., Cheng, X., Xu, J., Li, Z., Zheng, W., Zhang, P.-Z., 2018b. Active bending-moment faulting: Geomorphic expressions, controlling conditions, and the role in accommodating folding deformation. Tectonics 37, 2278–2306. doi:10.1029/2018TC004982

Li, C., Wang, S., Wang, L., 2019. Tectonostratigraphic history of the southern Tian Shan, western China, from seismic reflection profiling. Journal of Asian Earth Sciences 172, 101–

114. doi:10.1016/j.jseaes.2018.08.017

Lin, C., Li, H., Liu, J., 2012a. Major unconformities, tectonostratigraphic frameword, and evolution of the superimposed Tarim Basin, northwest China. Journal of Earth Science 23, 395–407. doi:10.1007/s12583-012-0263-4

Lin, C., Yang, H., Liu, J., Rui, Z., Cai, Z., Li, S., Yu, B., 2012b. Sequence architecture and depositional evolution of the Ordovician carbonate platform margins in the Tarim Basin and its response to tectonism and sea-level change. Basin Research 24, 559–582. doi:10.1111/j.1365-2117.2011.00536.x

Lin, C., Yang, H., Liu, J., Rui, Z., Cai, Z., Zhu, Y., 2012c. Distribution and erosion of the Paleozoic tectonic unconformities in the Tarim Basin, Northwest China: Significance for the evolution of paleo-uplifts and tectonic geography during deformation. Journal of Asian Earth Sciences 46, 1–19. doi:10.1016/j.jseaes.2011.10.004

Lin, W., Chu, Y., Ji, W., Zhang, Z., Shi, Y., Wang, Z., Li, Z., Wang, Q., 2013. Geochronological and geochemical constraints for a middle Paleozoic continental arc on the northern margin of the Tarim block: Implications for the Paleozoic tectonic evolution of the South Chinese Tianshan. Lithosphere 5, 355–381. doi:10.1130/L231.1

Lin, B., Zhang, X., Xu, X., Yuan, J., Neng, Y., Zhu, J., 2015a. Features and effects of basement faults on deposition in the Tarim Basin. Earth Science Reviews 145, 43–55. doi:10.1016/j.earscirev.2015.02.008

Lin, X., Zheng, D., Sun, J., Windley, B.F., Tian, Z., Gong, Z., Jia, Y., 2015b. Detrital apatite fission track evidence for provenance change in the Subei Basin and implications for the tectonic uplift of the Danghe Nan Shan (NW China) since the mid-Miocene. Journal of Asian Earth Sciences 111, 302–311. doi:10.1016/j.jseaes.2015.07.007

Liu, H., McClay, K.R., Powell, D., 1992. Physical models of thrust wedges. In: McClay, K.R. (Ed.), Thrust Tectonics. Springer Netherlands, Dordrecht, pp. 71–81. doi:10.1007/978-94-011-3066-0_6

Liu, Y.-J., Neubauer, F., Genser, J., Ge, X.-H., Takasu, A., Yuan, S.-H., Chang, L.-H., Li, W.-M., 2007. Geochronology of the initiation and displacement of the Altyn Strike-Slip Fault, western China. Journal of Asian Earth Sciences 29, 243–252. doi:10.1016/j.jseaes.2006.03.002

Liu, D., Jolivet, M., Yang, W., Zhang, Z., Cheng, F., Zhu, B., Guo, Z., 2013. Latest Paleozoic–

Early Mesozoic basin–range interactions in South Tian Shan (northwest China) and their tectonic significance: Constraints from detrital zircon U–Pb ages. Tectonophysics 599, 197–213. doi:10.1016/j.tecto.2013.04.018

Liu, H., Somerville, I.D., Lin, C., Zuo, S., 2015a. Distribution of Palaeozoic tectonic superimposed unconformities in the Tarim Basin, NW China: significance for the evolution of palaeogeomorphology and sedimentary response. Geological Journal 1–25. doi:10.1002/gj.2664

Liu, S., Lei, X., Wang, L., 2015b. New heat flow determination in northern Tarim Craton, northwest China. Geophysical Journal International 200, 1196–1204. doi:10.1093/gji/ggu458

Liu, Y.J., Genser, J., Ge, X., Neubauer, F., Friedl, G., Chang, L., Ren, S., Handler, R., 2003. 40Ar/39Ar age evidence for Altyn fault tectonic activities in western China. Chinese Science Bulletin 48, 2024–2030. doi:10.1360/02wd0611

Liu-Zeng, J., Tapponnier, P., Gaudemer, Y., Ding, L., 2008. Quantifying landscape differences across the Tibetan plateau: Implications for topographic relief evolution. Journal of Geophysical Research 113, 1–26. doi:10.1029/2007JF000897

Loury, C., Rolland, Y., Guillot, S., Mikolaichuk, A.V., Lanari, P., Bruguier, O., Bosch, D., 2017. Crustal-scale structure of South Tien Shan: implications for subduction polarity and Cenozoic reactivation. Geological Society, London, Special Publications 427, 197–229. doi:10.1144/SP427.4

Loury, C., Rolland, Y., Lanari, P., Guillot, S., Bosch, D., Ganino, C., Jourdon, A., Petit, C., Gallet, S., Monié, P., Riel, N., 2018. Permian charnockites in the Pobeda area: Implications for Tarim mantle plume activity and HT metamorphism in the South Tien Shan range. Lithos 304-307, 135–154. doi:10.1016/j.lithos.2018.01.025

Lu, H., Burbank, D.W., Li, Y., Liu, Y., 2010. Late Cenozoic structural and stratigraphic evolution of the northern ChineseTian Shan foreland. Basin Research 22, 249–269. doi:10.1111/j.1365-2117.2009.00412.x

Lu, H., Wang, E., Meng, K., 2014. Paleomagnetism and anisotropy of magnetic susceptibility of the Tertiary Janggalsay section (southeast Tarim basin): Implications for Miocene tectonic evolution of the Altyn Tagh Range. Tectonophysics 618, 67–78. doi:10.1016/j.tecto.2014.01.031

Lu, R., Xu, X., He, D., Liu, B., Tan, X., Wang, X., 2016. Coseismic and blind fault of the 2015

Pishan Mw 6.5 earthquake: Implications for the sedimentary-tectonic framework of the western Kunlun Mountains, northern Tibetan Plateau. Tectonics 35, 956–964. doi:10.1002/(ISSN)1944-9194

Lyon-Caen, H., Molnar, P., 1984. Gravity anomalies and the structure of western Tibet and the Southern Tarim Basin. Geophysical Research Letters 11, 1251–1254. doi:10.1029/GL011i012p01251

Macaulay, E.A., Sobel, E.R., Mikolaichuk, A., Kohn, B., Stuart, F.M., 2014. Cenozoic deformation and exhumation history of the Central Kyrgyz Tien Shan. Tectonics 33, 135–165. doi:1002/2013TC003376

Makarov, V.I., Alekseev, D.V., Batalev, V.Y., Bataleva, E.A., Belyaev, I.V., Bragin, V.D., Dergunov, N.T., Efimova, N.N., Leonov, M.G., Munirova, L.M., Pavlenkin, A.D., Roecker, S., Roslov, Y.V., Rybin, A.K., Shchelochkov, G.G., 2010. Underthrusting of Tarim beneath the Tien Shan and Deep Structure of Their Junction Zone: Main Results of Seismic Experiment along MANAS Profile Kashgar–Song-Köl. Geotectonics 44, 102–126. doi:10.1134/S0016852110020020

Mandal, N., Chattopadhyay, A., Bose, S., 1997. Imbricate thrust spacing: experimental and theoretical analyses. In: Sengupta, S. (Ed.), Evolution of Geological Structures in Micro- to Macro-Scales. Springer Netherlands, Dordrecht, pp. 143–165. doi:10.1007/978-94-011-5870-1

Mattauer, M., Matte, P., Olivet, J.L., 1999. A 3D model of the India-Asia collision at plate scale. Comptes Rendues de l'Académie des Sciences, Series IIA, Earth and Planetary Science 328, 499–508. doi:10.1016/S1251-8050(99)80130-X

Matte, P., Tapponnier, P., Arnaud, N., Bourjot, L., Avouac, J.P., Vidal, P., Liu, Q., Pan, Y., Wang, Y., 1996. Tectonics of Western Tibet, between the Tarim and the Indus. Earth and Planetary Science Letters 142, 311–330. doi:10.1016/0012-821X(96)00086-6

Mattern, F., Schneider, W., 2000. Suturing of the Proto- and Paleo-Tethys oceans in the western Kunlun (Xinjiang, China). Journal of Asian Earth Sciences 18, 637–650. doi:10.1016/S1367-9120(00)00011-0

McClay, K., Bonora, M., 2001. Analog models of restraining stepovers in strike-slip fault systems. American Association of Petroleum Geologists Bulletin 85, 233–260. doi:10.1306/8626C7AD-173B-11D7-8645000102C1865D

Meng, Q.R., Hu, J.-M., Yang, F.-Z., 2001. Timing and magnitude of displacement on the Altyn Tagh fault: constraints from stratigraphic correlation of adjoining Tarim and Qaidam basins, NW China. Terra Nova 13, 86–91. doi:10.1046/j.1365-3121.2001.00320.x

Ménard, G., Molnar, P., Platt, J.P., 1991. Budget of crustal shortening and subduction of continental crust in the Alps. Tectonics 10, 231–244. doi:10.1029/90TC02552

Métivier, F., Gaudemer, Y., 1997. Mass transfer between eastern Tien Shan and adjacent basins (central Asia): constraints on regional tectonics and topography. Geophysical Journal International 128, 1–17. doi:10.1111/j.1365-246X.1997.tb04068.x

Métivier, F., Gaudemer, Y., Tapponnier, P., Meyer, B., 1998. Northeastward growth of the Tibet plateau deduced from balanced reconstruction of two depositional areas: The Qaidam and Hexi Corridor basins, China. Tectonics 17, 823–842. doi:10.1029/98TC02764

Métivier, F., Gaudemer, Y., Tapponnier, P., Klein, M., 1999. Mass accumulation rates in Asia during the Cenozoic. Geophysical Journal International 137, 280–318. doi:10.1046/j.1365-246X.1999.00802.x

Mitra, S., Namson, J., 1989. Equal-area balancing. American Journal of Science 289, 563–599.

Molnar, P., 1984. Structure and Tectonics of the Himalaya: Constraints and Implications of Geophysical Data. Annual Review of Earth and Planetary Sciences 12, 489–516. doi:10.1146/annurev.ea.12.050184.002421

Molnar, P., Tapponnier, P., 1975. Cenozoic tectonics of Asia : Effects of a continental collision. Science 189, 419–426.

Morin, J., Jolivet, M., Robin, C., Heilbronn, G., Barrier, L., Bourquin, S., Jia, Y., 2018. Jurassic paleogeography of the Tian Shan: An evolution driven by far-field tectonics and climate. Earth Science Reviews 187, 286–313. doi:10.1016/j.earscirev.2018.10.007

Morin, J., Jolivet, M., Barrier, L., Laborde, A., Haibing, L., Dauteuil, O., 2019. Planation surfaces of the Tian Shan Range (Central Asia): Insight on several 100 Myrs of topographic evolution. Journal of Asian Earth Sciences, 177: 52-65. doi:10.1016/j.jseaes.2019.03.011

Mugnier, J.L., Baby, P., Colletta, B., Vinour, P., Bale, P., Leturmy, P., 1997. Thrust geometry controlled by erosion and sedimentation: A view from analogue models. Geology 25, 427–4. doi:10.1130/0091-7613(1997)025<0427:TGCBEA>2.3.CO;2

Muñoz, J.A., 1992. Evolution of a continental collision belt: ECORS-Pyrenees crustal balanced cross-section. In: McClay, K.R. (Ed.), Thrust Tectonics. Springer Netherlands, Dordrecht,

pp. 235–246. doi:10.1007/978-94-011-3066-0_21

Neil, E.A., Houseman, G.A., 1997. Geodynamics of the Tarim Basin and the Tian Shan in central Asia. Tectonics 16, 571–584. doi:10.1029/97TC01413

Neng, Y., Xie, H., Yin, H., Li, Y., Wang, W., 2018. Effect of basement structure and salt tectonics on deformation styles along strike: An example from the Kuqa fold–thrust belt, West China. Tectonophysics 730, 114–131. doi:10.1016/j.tecto.2018.02.006

Nester, D.C., Padgett, M.J., 1992. Seismic interpretation. In: Morton-Thompson, D., Woods, A.M. (Eds.), Development Geology Reference Manual. American Aassociation of Petroleum Geologists Methods in Exploration Series, 10: 379-380.

Pan, J., Li, H., Sun, Z., Pei, J., Si, J., Barrier, L., Van der Woerd, J., Qiu, Z., Wu, F., Zhang, L., 2010. Deformation features of the Mazartagh fold-thrust belt, south central Tarim Basin and its tectonic significances. Chinese Journal of Geology 45, 1038–1056. (in Chinese with English abstract)

Pan, G., Wang, L., Li, R., Yuan, S., Ji, W., Yin, F., Zhang, W., Wang, B., 2012. Tectonic evolution of the Qinghai-Tibet Plateau. Journal of Asian Earth Sciences 53, 3–14. doi:10.1016/j.jseaes.2011.12.018

Peltzer, G., Tapponnier, P., 1988. Formation and evolution of strike-slip faults, rifts, and basins during the India-Asia Collision: An experimental approach. Journal of Geophysical Research: Solid Earth 93, 15085–15117. doi:10.1029/JB093iB12p15085

Peng, S., Li, Z., Huang, B., Liu, T., Wang, Q., 2006. Magnetostratigraphic study of Cretaceous depositional succession in the northern Kuqa Depression, Northwest China. Chinese Science Bulletin 51, 97–107. doi:10.1007/s11434-005-0340-5

Peng, J., Li, J., Li, W., Slater, S.M., Zhu, H., Vajda, V., 2018. The Triassic to Early Jurassic palynological record of the Tarim Basin, China. Palaeobiodiversity and Palaeoenvironments 98, 7–28. doi:10.1007/s12549-017-0279-y

Poupinet, G., Avouac, J.P., Jiang, M., Wei, S., Kissling, E., Herquel, G., Guilbert, J., Paul, A., Wittlinger, G., Su, H., Thomas, J.C., 2002. Intracontinental subduction and Palaeozoic inheritance of the lithosphere suggested by a teleseismic experiment across the Chinese Tien Shan. Terra Nova 14, 18–24. doi:10.1046/j.1365-3121.2002.00391.x

Puigdefabregas, C., Muoz, J.A., Marzo, M., 1986. Thrust Belt Development in the Eastern Pyrenees and Related Depositional Sequences in the Southern Foreland Basin. In: Allen,

P.A., Homewood, P. (Eds.), Foreland Basins. Blackwell Publishing Ltd., Oxford, UK, pp. 229–246. doi:10.1002/9781444303810.ch12

Qi, J., Lei, G., Li, M., Xie, H., Yang, S., 2009. Contractional structure model of the transition belt between Kuche Depression and South Tianshan Uplift. Earth Science Frontiers 16, 120–128. doi:10.1016/S1872-5791(08)60089-5

Qiu, N., Jiang, G., Mei, Q., Chang, J., Wang, S., Wang, J., 2011. The Paleozoic tectonothermal evolution of the Bachu Uplift of the Tarim Basin, NW China: Constraints from (U-Th)/He ages, apatite fission track and vitrinite reflectance data. Journal of Asian Earth Sciences 41, 551–563. doi:10.1016/j.jseaes.2011.02.008

Ren, R., Guan, S., Wu, L., Zhu, G., 2018. Evolution of the Neoproterozoic rift basins and its implication for oil and gas exploration in the Tarim Basin. Petroleum Research 3, 66–76. doi:10.1016/j.ptlrs.2018.03.003

Ritts, B.D., Yue, Y., Graham, S.A., Sobel, E.R., Abbink, O.A., Stockli, D., 2008. From sea level to high elevation in 15 million years: Uplift history of the northern Tibetan Plateau margin in the Altun Shan. American Journal of Science 308, 657–678. doi:10.2475/05.2008.01

Robinson, D.M., Dupont-Nivet, G., Gehrels, G.E., Zhang, Y., 2003. The Tula uplift, northwestern China: Evidence for regional tectonism of the northern Tibetan Plateau during late Mesozoic–early Cenozoic time. Geological Society of America Bulletin 115, 35–47. doi:10.1130/0016-7606(2003)115<0035:TTUNCE>2.0.CO;2

Rumelhart, P.E., An, Y., Cowgill, E., Butler, R., Zhang, Q., Xiao-Feng, W., 1999. Cenozoic vertical-axis rotation of the Altyn Tagh fault system. Geology 27, 819–822. doi:10.1130/0091-7613(1999)027<0819:CVAROT>2.3.CO;2

Scharer, K.M., Burbank, D.W., Chen, J., Weldon, R.J., Rubin, C., Zhao, R., Shen, J., 2004. Detachment folding in the Southwestern Tian Shan–Tarim foreland, China: shortening estimates and rates. Journal of Structural Geology 26, 2119–2137. doi:10.1016/j.jsg.2004.02.016

Shu, L.S., Deng, X.L., Zhu, W.B., Ma, D.S., Xiao, W.J., 2011. Precambrian tectonic evolution of the Tarim Block, NW China: New geochronological insights from the Quruqtagh domain. Journal of Asian Earth Sciences 42, 774–790. doi:10.1016/j.jseaes.2010.08.018

Simoes, M., Avouac, J.-P., 2006. Investigating the kinematics of mountain building in Taiwan from the spatiotemporal evolution of the foreland basin and western foothills. Journal of

2476 Geophysical Research 111, 355–25. doi:10.1029/2005JB004209
2477 Sinclair, H.D., Allen, P.A., 1992. Vertical versus horizontal motions in the Alpine orogenic
2478 wedge: stratigraphic response in the foreland basin. Basin Research 4, 215–232.
2479 doi:10.1111/j.1365-2117.1992.tb00046.x
2480 Sloan, R.A., Jackson, J.A., McKenzie, D., Priestley, K., 2011. Earthquake depth distributions in
2481 central Asia, and their relations with lithosphere thickness, shortening and extension.
2482 Geophysical Journal International 185, 1–29. doi:10.1111/j.1365-246X.2010.04882.x
2483 Smit, J.H.W., Brun, J.P., Sokoutis, D., 2003. Deformation of brittle-ductile thrust wedges in
2484 experiments and nature. Journal of Geophysical Research: Solid Earth 108, 3–18.
2485 doi:10.1029/2002JB002190
2486 Sobel, E.R., 2001. Jurassic to Cenozoic exhumation history of the Altyn Tagh range, northwest
2487 China, constrained by 40Ar/39Ar and apatite fission track thermochronology. In: Hendrix,
2488 M.S., Davis, G.A. (Eds.), Paleozoic and Mesozoic Tectonic Evolution of Central Asia.
2489 Geological Society of America Memoir 194, pp. 247–267.
2490 Sobel, E.R., Dumitru, T.A., 1997. Thrusting and exhumation around the margins of the western
2491 Tarim basin during the India-Asia collision. Journal of Geophysical Research: Solid Earth
2492 102, 5043–5063. doi:10.1029/96JB03267
2493 Sobel, E.R., 1999. Basin analysis of the Jurassic–Lower Cretaceous southwest Tarim basin,
2494 northwest China. Geological Society of America Bulletin 111, 709–724. doi:10.1130/0016-
2495 7606(1999)111<0709:BAOTJL>2.3.CO;2
2496 Sobel, E.R., Arnaud, N., 1999. A possible middle Paleozoic suture in the Altyn Tagh, NW
2497 China. Tectonics 18, 64–74. doi:10.1029/1998TC900023
2498 Sobel, E., Chen, J., Heermance, R., 2006. Late Oligocene–Early Miocene initiation of shortening
2499 in the Southwestern Chinese Tian Shan: Implications for Neogene shortening rate variations.
2500 Earth and Planetary Science Letters 247, 70–81. doi:10.1016/j.epsl.2006.03.048
2501 Strecker, M.R., Hilley, G.E., Bookhagen, B., Sobel, E.R., 2012. Structural, geomorphic, and
2502 depositional characteristics of contiguous and broken foreland basins: examples from the
2503 eastern flanks of the central Andes in Bolivia and NW Argentina. In: Busby, C., Azor, A.
2504 (Eds.), Tectonics of Sedimentary Basins: Recent Advances. pp. 1–14.
2505 Sun, Z., Feng, X., Li, D., Yang, F., Qu, Y., Wang, H., 1999. Cenozoic Ostracoda and
2506 palaeoenvironments of the northeastern Tarim Basin, western China. Palaeogeography,

Palaeoclimatology, Palaeoecology 148, 37–50. doi:10.1016/S0031-0182(98)00174-6

Sun, J., Zhu, R., An, Z., 2005. Tectonic uplift in the northern Tibetan Plateau since 13.7 Ma ago inferred from molasse deposits along the Altyn Tagh Fault. Earth and Planetary Science Letters 235, 641–653. doi:10.1016/j.epsl.2005.04.034

Sun, J., Li, Y., Zhang, Z., Fu, B., 2009a. Magnetostratigraphic data on Neogene growth folding in the foreland basin of the southern Tianshan Mountains. Geology 37, 1051–1054. doi:10.1130/G30278A.1

Sun, J., Zhang, Z., Zhang, L., 2009b. New evidence on the age of the Taklimakan Desert. Geology 37, 159–162. doi:10.1130/G25338A.1

Sun, J., Jiang, M., 2013. Eocene seawater retreat from the southwest Tarim Basin and implications for early Cenozoic tectonic evolution in the Pamir Plateau. Tectonophysics 588, 27–38. doi:10.1016/j.tecto.2012.11.031

Sun, J., Windley, B.F., Zhang, Z., Fu, B., Li, S., 2016a. Diachronous seawater retreat from the southwestern margin of the Tarim Basin in the late Eocene. Journal of Asian Earth Sciences 116, 222–231. doi:10.1016/j.jseaes.2015.11.020

Sun, J., Xiao, W.-J., Windley, B.F., Ji, W., Fu, B., Wang, J., Jin, C., 2016b. Provenance change of sediment input in the northeastern foreland of Pamir related to collision of the Indian Plate with the Kohistan-Ladakh arc at around 47 Ma. Tectonics 35, 315–338. doi:10.1002/2015TC003974

Sun, J., Liu, W., Liu, Z., Deng, T., Windley, B.F., Fu, B., 2017. Extreme aridification since the beginning of the Pliocene in the Tarim Basin, western China. Palaeogeography, Palaeoclimatology, Palaeoecology 485, 189–200. doi:10.1016/j.palaeo.2017.06.012

Suppe, J., Wang, X., He, D., Liang, H., 2015. Large-scale thrusting along the northern margin of the Tibetan Plateau and the southwest Tarim basin: 230 km long active Hotian thrust sheet. AGU Fall Meeting Abstract.

Tang, D., Xing, W., Lin, W., Kong, F., Li, D., Xu, H., Tao, S., Gao, G., 2008. Composite Petroleum System and Advantageous Exploration Targets in the Kongquehe Area of Tarim Basin. Earth Science Frontiers 15, 167–177. doi:10.1016/S1872-5791(08)60031-7

Tang, L., Huang, T., Qiu, H., Wan, G., Li, M., Yang, Y., Xie, D., Chen, G., 2014. Fault systems and their mechanisms of the formation and distribution of the Tarim Basin, NW China. J. Earth Sci. 25, 169–182. doi:10.1007/s12583-014-0410-1

Tang, P., Rao, G., Li, S., Yu, Y., Pei, Y., Wang, X., Shen, Z., Chen, N., Zhao, B., 2017. Lateral structural variations and drainage response along the Misikantage anticline in the western Kuqa fold-and-thrust belt, southern Tianshan, NW China. Tectonophysics 721, 196–210. doi:10.1016/j.tecto.2017.10.007

Tapponnier, P., Molnar, P., 1977. Active faulting and tectonics in China. Journal of Geophysical Research 82, 2905–2930. doi:10.1029/JB082i020p02905

Tapponnier, P., Molnar, P., 1979. Active faulting and cenozoic tectonics of the Tien Shan, Mongolia, and Baykal Regions. Journal of Geophysical Research: Solid Earth 84, 3425–3459. doi:10.1029/JB084iB07p03425

Tapponnier, P., Peltzer, G., Le Dain, A.Y., Armijo, R., Cobbold, P., 1982. Propagating extrusion tectonics in Asia: New insights from simple experiments with plasticine. Geology 10, 611–616. doi:10.1130/0091-7613(1982)10<611:PETIAN>2.0.CO;2

Tapponnier, P., Zhiqin, X., Roger, F., Meyer, B., Arnaud, N., Wittlinger, G., Jingsui, Y., 2001. Oblique stepwise rise and growth of the Tibet Plateau. Science 294, 1671–1677. doi:10.1126/science.105978

Teixell, A., 1998. Crustal structure and orogenic material budget in the west central Pyrenees. Tectonics 17, 395–406. doi:10.1029/98TC00561

Thompson, J.A., Burbank, D.W., Li, T., Chen, J., Bookhagen, B., 2015. Late Miocene northward propagation of the northeast Pamir thrust system, northwest China. Tectonics 34, 510–534. doi:10.1002/2014TC003690

Thompson Jobe, J.A., Li, T., Chen, J., Burbank, D.W., Bufe, A., 2017. Quaternary tectonic evolution of the Pamir-Tian Shan convergence zone, Northwest China. Tectonics 36, 2748–2776. doi:10.1002/2017TC004541

Thompson Jobe, J.A., Li, T., Bookhagen, B., Chen, J., Burbank, D., 2018. Dating growth strata and basin fill by combining 26Al/10Be burial dating and magnetostratigraphy: Constraining active deformation in the Pamir–Tian Shan convergence zone, NW China. Lithosphere 10, 806–828. doi:10.1130/L727.1

Tian, Z., Sun, J., Windley, B.F., Zhang, Z., Gong, Z., Lin, X., Xiao, W.-J., 2016. Cenozoic detachment folding in the southern Tianshan foreland, NW China: Shortening distances and rates. Journal of Structural Geology 84, 142–161. doi:10.1016/j.jsg.2016.01.007

Tong, D., Zhang, J., Yang, H., Hu, D., Ren, J., 2012. Fault system, deformation style and

development mechanism of the Bachu Uplift, Tarim Basin. Journal of Earth Science 23, 529–541. doi:10.1007/s12583-012-0273-2

Turner, S.A., Cosgrove, J.W., Liu, J.G., 2010. Controls on lateral structural variability along the Keping Shan Thrust Belt, SW Tien Shan Foreland, China. Geological Society, London, Special Publications 348, 71–85. doi:10.1144/SP348.5

Turner, S.A., Liu, J.G., Cosgrove, J.W., 2011. Structural evolution of the Piqiang Fault Zone, NW Tarim Basin, China. Journal of Asian Earth Sciences 40, 394–402. doi:10.1016/j.jseaes.2010.06.005

Vilotte, J.P., Daignières, M., Madariaga, R., Zienkiewicz, O.C., 1984. The role of a heterogeneous inclusion during continental collision. Physics of the Earth and Planetary Interiors 36, 236–259. doi:10.1016/0031-9201(84)90049-9

Wang, E., 1997. Displacement and timing along the northern strand of the Altyn Tagh fault zone, Northern Tibet. Earth and Planetary Science Letters 150, 55–64. doi:10.1016/S0012-821X(97)00085-X

Wang, S.Z., Li, J.-G., Zhou, Y.-S., 2007. Experimental evidence for intraplate deformation controlled by netlike plastic-flow in central-eastern Asia. Physics of the Earth and Planetary Interiors 165, 208–228. doi:10.1016/j.pepi.2007.10.001

Wang, Q., Li, S., Du, Z., 2009. Differential uplift of the Chinese Tianshan since the Cretaceous: constraints from sedimentary petrography and apatite fission-track dating. International Journal of Earth Sciences 98, 1341–1363. doi:10.1007/s00531-009-0436-2

Wang, S.L., Shu, L.-S., Zhu, W.-B., Xu, M.-J., Lu, H.-F., Xiao, Z.-Y., Luo, J.-C., Zhu, C.-J., 2012. Mesozoic faults in the NE Tarim (western China) and the implications on collisions in the southern Eurasian margin. Journal of Asian Earth Sciences 56, 191–199. doi:10.1016/j.jseaes.2012.05.012

Wang, C.Y., Chen, H.-L., Cheng, X.-G., Li, K., 2013. Evaluating the role of syn-thrusting sedimentation and interaction with frictional detachment in the structural evolution of the SW Tarim basin, NW China: Insights from analogue modeling. Tectonophysics 608, 642–652. doi:10.1016/j.tecto.2013.08.016

Wang, C.S., Dai, J., Zhao, X., Li, Y., Graham, S.A., He, D., Ran, B., Meng, J., 2014a. Outward-growth of the Tibetan Plateau during the Cenozoic: A review. Tectonophysics 621, 1–43. doi:10.1016/j.tecto.2014.01.036

Wang, X., Sun, D., Chen, F., Wang, F., Li, B., Popov, S.V., Wu, S., Zhang, Y., Li, Z., 2014b. Cenozoic paleo-environmental evolution of the Pamir–Tien Shan convergence zone. Journal of Asian Earth Sciences 80, 84–100. doi:10.1016/j.jseaes.2013.10.027

Wang, X., Suppe, J., Liang, H., He, D., 2014c. Large-scale thrusting along the northern margin of the Tibetan Plateau and the southwest Tarim basin: 230 km long active Hotian thrust sheet. EGU General Assembly Abstract.

Wang, Ch., Liu, L., Wang, Y.-H., He, S.-P., Li, R.-S., Li, M., Yang, W.-Q., Cao, Y.-T., Collins, A.S., Shi, C., Wu, Z.-N., 2015. Recognition and tectonic implications of an extensive Neoproterozoic volcano-sedimentary rift basin along the southwestern margin of the Tarim Craton, northwestern China. Precambrian Research 257, 65–82. doi:10.1016/j.precamres.2014.11.022

Wang, Z., Wang, X., 2016. Late Cenozoic Deformation Sequence of a Thrust System along the Eastern Margin of Pamir, Northwest China. Acta Geologica Sinica - English Edition 90, 1664–1678. doi:10.1111/1755-6724.12809

Wang, C.Y., Cheng, X., Chen, H., Ding, W., Lin, X., Wu, L., Li, K., Shi, J., Li, Y., 2016a. The effect of foreland palaeo-uplift on deformation mechanism in the Wupoer fold-and-thrust belt, NE Pamir: Constraints from analogue modelling. Journal of Geodynamics 100, 115–129. doi:10.1016/j.jog.2016.03.001

Wang, Co., Cheng, X.-G., Chen, H.-L., Li, K., Fan, X.-G., Wang, C.-Y., 2016b. From folding to transpressional faulting: the Cenozoic Fusha structural belt in front of the Western Kunlun Orogen, northwestern Tibetan Plateau. International Journal of Earth Sciences 105, 1621–1636. doi:10.1007/s00531-016-1305-4

Wang, W., Yin, H., Jia, D., Li, C., 2017. A sub-salt structural model of the Kelasu structure in the Kuqa foreland basin, northwest China. Marine and Petroleum Geology 88, 115–126. doi:10.1016/j.marpetgeo.2017.08.008

Wei, H.H., Meng, Q.-R., Ding, L., Li, Z.-Y., 2013. Tertiary evolution of the western Tarim basin, northwest China: A tectono-sedimentary response to northward indentation of the Pamir salient. Tectonics 32, 558–575. doi:10.1002/tect.20046

Wen, L., Li, Y.-J., Zhang, G.-Y., Tian, Z.-J., Peng, G.-X., Bin Qiu, Huang, Z.-B., Luo, J.-C., Zhang, Q., 2017. Evolution of fold-thrust belts and Cenozoic uplifting of the South Tianshan Mountain range in the Kuqa region, Northwest China. Journal of Asian Earth Sciences 135,

327–337. doi:10.1016/j.jseaes.2017.01.002

Windley, B.F., Allen, M.B., Zhang, C., Zhao, Z.-Y., Wang, G.-R., 1990. Paleozoic accretion and Cenozoic redeformation of the Chinese Tien Shan Range, central Asia. Geology 18, 128–131. doi:10.1130/0091-7613(1990)018<0128:PAACRO>2.3.CO;2

Wittlinger, G., Tapponnier, P., Poupinet, G., Mei, J., Danian, S., Herquel, G., Masson, F., 1998. Tomographic Evidence for Localized Lithospheric Shear Along the Altyn Tagh Fault. Science 282, 74–76. doi:10.1126/science.282.5386.74

Wittlinger, G., Vergne, J., Tapponnier, P., Farra, V., Poupinet, G., Jiang, M., Su, H., Herquel, G., Paul, A., 2004. Teleseismic imaging of subducting lithosphere and Moho offsets beneath western Tibet. Earth and Planetary Science Letters 221, 117–130. doi:10.1016/S0012-821X(03)00723-4

Woodcock, N.H., Rickards, B., 2003. Transpressive duplex and flower structure: Dent Fault System, NW England. Journal of Structural Geology 25, 1981–1992. doi:10.1016/S0191-8141(03)00057-9

Woodward, N.B., Boyer, S.E., Suppe, J., 1989. Balanced Geological Cross-sections: An Essential Technique in Geological Research and Exploration. Short Course in Geology, 6: 132 p. doi: 10.1029/SC006

Wu, LX., A., Yang, S., Wang, L., Mao, L., Wang, L., Dong, Y., Xu, B., 2012. Two-stage evolution of the Altyn Tagh Fault during the Cenozoic: new insight from provenance analysis of a geological section in NW Qaidam Basin, NW China. Terra Nova 24, 387–395. doi:10.1111/j.1365-3121.2012.01077.x

Wu, Z.Y., Yin, H., Wang, X., Zhao, B., Jia, D., 2014. Characteristics and deformation mechanism of salt-related structures in the western Kuqa depression, Tarim basin: Insights from scaled sandbox modeling. Tectonophysics 612-613, 81–96. doi:10.1016/j.tecto.2013.11.040

Wu, L., Guan, S., Zhang, S., Yang, H., Jin, J., Zhang, X., Zhang, C., 2018. Neoproterozoic stratigraphic framework of the Tarim Craton in NW China: Implications for rift evolution. Journal of Asian Earth Sciences 158, 240–252. doi:10.1016/j.jseaes.2018.03.003

Xiao, W.J., Windley, B.F., Allen, M.B., Han, C., 2013. Paleozoic multiple accretionary and collisional tectonics of the Chinese Tianshan orogenic collage. Gondwana Research 23, 1316–1341. doi:10.1016/j.gr.2012.01.012

Xiao, W.J., Windley, B.F., Liu, D.Y., Jian, P., Liu, C.Z., Yuan, C., Sun, M., 2005. Accretionary Tectonics of the Western Kunlun Orogen, China: A Paleozoic–Early Mesozoic, Long-Lived Active Continental Margin with Implications for the Growth of Southern Eurasia. The Journal of Geology 113, 687–705. doi:10.1086/449326

Xiao, W.J., Zhang, L.-C., Qin, K.-Z., Sun, S., Li, J.-L., 2004. Paleozoic accretionary and collisional tectonics of the eastern Tianshan (China): Implications for the continental growth of central Asia. American Journal of Science 304, 370–395. doi:10.2475/ajs.304.4.370

Xie, H., Chen, X., Zhu, M., Li, L., Wang, X., Chen, H., Cheng, X., 2017. Deformation characteristics, tectonic evolution and their control on deep petroleum accumulation of Mazhatage Fault Belt in Tarim Basin. Earth Science 42, 1578–1589. doi:10.3799/dqkx.2017.504 (in Chinese with English abstract)

Xinjiang Bureau of Geology and Mineral Resources, 1985. Geological maps of the Xinjiang Uygur Autonomous Region, China. Scale 1:500,000.

Xinjiang Bureau of Geology and Mineral Resources, 1976. Geological maps of the Xinjiang Uygur Autonomous Region, China. Scale 1:200,000.

Xu, C., Zhou, X.-Y., 2007. Seismic interpretation of the Kelasu triangle zone in the southern Tian Shan foothills, northwestern China. American Association of Petroleum Geologists Bulletin 91, 161–171. doi:10.1306/09070606077

Xu, Y.G., Wei, X., Luo, Z.-Y., Liu, H.-Q., Cao, J., 2014. The Early Permian Tarim Large Igneous Province: Main characteristics and a plume incubation model. Lithos 204, 20–35. doi:10.1016/j.lithos.2014.02.015

Yang, Y.Q., Liu, M., 2002. Cenozoic deformation of the Tarim plate and the implications for mountain building in the Tibetan Plateau and the Tian Shan. Tectonics 21, 1–17. doi:10.1029/2001TC001300

Yang, H.J., Li, Y., Feng, X., Zheng, M., Zhang, C.J., Zhao, Y., 2007a. Analysis on thrustings of the Mazhatage structural belt in the Tarim Basin. Chinese Journal of Geology 1–12 (in Chinese with English abstract)

Yang, X.P., Ran, Y., Cheng, J., Chen, L., Xu, X., 2007b. Measurement of terrace deformation and crustal shortening of some renascent fold zones within Kalpin nappe structure. Science in China Series D: Earth Sciences 50, 33–42. doi:10.1007/s11430-007-2072-7

Yang, Ya., Hu, J.-Z., Lin, C.-S., 2009. Geological Structure and Petroleum Geology Features of

Aqike Anticline in Southwest Tarim Basin. Acta Geoscientica Sinica 30, 263–270 (in Chinese with English abstract)

Yang, S.F., Chen, H., Li, Z., Li, Y., Yu, X., Li, D., Meng, L., 2013. Early Permian Tarim Large Igneous Province in northwest China. Science China Earth Sciences 56, 2015–2026. doi:10.1007/s11430-013-4653-y

Yang, G., Li, W., Chen, Z., Shi, X., Lei, Y., Wang, X., 2015. Mazatage detachment anticline in Hetianhe gas field, Tarim Basin, western China. Oil Gas Geology 36, 563–572. doi:10.11743/ogg20150405 (in Chinese with English abstract)

Yang, J.F., Zhu, W., Guan, D., Zhu, B., Yuan, L., Xiang, X., Su, J., He, J., Wu, X., 2016. 3D seismic interpretation of subsurface eruptive centers in a Permian large igneous province, Tazhong Uplift, central Tarim Basin, NW China. International Journal of Earth Sciences 105, 2311–2326. doi:10.1007/s00531-015-1289-5

Yang, W., Fu, L., Wu, C., Song, Y., Jiang, Z., Luo, Q., Zhang, Z., Zhang, C., Zhu, B., 2018a. U-Pb ages of detrital zircon from Cenozoic sediments in the southwestern Tarim Basin, NW China_ Implications for Eocene–Pliocene source-to-sink relations and new insights into Cretaceous–Paleogene magmatic sources. Journal of Asian Earth Sciences 156, 26–40. doi:10.1016/j.jseaes.2018.01.010

Yang, Yo., Yao, W.-Q., Yan, J.-J., Guo, Y., Xie, D.-Q., 2018b. Mesozoic and Cenozoic structural deformation in the NW Tarim Basin, China: a case study of the Piqiang–Selibuya Fault. International Geology Review 60, 929–943. doi:10.1080/00206814.2017.1360803

Yeck, W.L., Sheehan, A.F., Anderson, M.L., Erslev, E.A., Miller, K.C., Siddoway, C.S., 2014. Structure of the Bighorn Mountain region, Wyoming, from teleseismic receiver function analysis: Implications for the kinematics of Laramide shortening. Journal of Geophysical Research: Solid Earth 119, 7028–7042. doi:10.1002/(ISSN)2169-9356

Yin, A., Nie, S., Craig, P., Harrison, T.M., Ryerson, F.J., Xianglin, Q., Geng, Y., 1998. Late Cenozoic tectonic evolution of the southern Chinese Tian Shan. Tectonics 17, 1–27. doi:10.1029/97TC03140

Yin, A., Harrison, T.M., 2000. Geologic Evolution of the Himalayan-Tibetan Orogen. Annual Review of Earth and Planetary Sciences 28, 211–280. doi:10.1146/annurev.earth.28.1.211

Yin, A., Rumelhart, P.E., Butler, R., Cowgill, E., Harrison, T.M., Foster, D.A., Ingersoll, R.V., Zhang, Q., Xian-Qiang, Z., Xiao-Feng, W., Hanson, A., Raza, A., 2002. Tectonic history of

the Altyn Tagh fault system in northern Tibet inferred from Cenozoic sedimentation. Geological Society of America Bulletin 114, 1257–1295. doi:10.1130/0016-7606(2002)114<1257:THOTAT>2.0.CO;2

Yin, A., 2010. Cenozoic tectonic evolution of Asia: A preliminary synthesis. Tectonophysics 488, 293–325. doi:10.1016/j.tecto.2009.06.002

Yin, A., Dubey, C.S., Webb, A.A.G., Kelty, T.K., Grove, M., Gehrels, G.E., Burgess, W.P., 2010. Geologic correlation of the Himalayan orogen and Indian craton: Part 1. Structural geology, U-Pb zircon geochronology, and tectonic evolution of the Shillong Plateau and its neighboring regions in NE India. Geological Society of America Bulletin 122, 336–359. doi:10.1130/B26460.1

Yonkee, W.A., Weil, A.B., 2015. Tectonic evolution of the Sevier and Laramide belts within the North American Cordillera orogenic system. Earth Science Reviews 150, 531–593. doi:10.1016/j.earscirev.2015.08.001

Yu, S., Chen, W., Evans, N.J., McInnes, B.I.A., Yin, J., Sun, J., Li, J., Bin Zhang, 2014. Cenozoic uplift, exhumation and deformation in the north Kuqa Depression, China as constrained by (U–Th)/He thermochronometry. Tectonophysics 630, 166–182. doi:10.1016/j.tecto.2014.05.021

Yue, Y., Ritts, B.D., Graham, S.A., 2001. Initiation and Long-Term Slip History of the Altyn Tagh Fault. International Geology Review 43, 1087–1093. doi:10.1080/00206810109465062

Zeng, L., Wang, H., Gong, L., Liu, B., 2010. Impacts of the tectonic stress field on natural gas migration and accumulation: A case study of the Kuqa Depression in the Tarim Basin, China. Marine and Petroleum Geology 27, 1616–1627. doi:10.1016/j.marpetgeo.2010.04.010

Zhang, C.L., Li, X.H., Li, Z.-X., Ye, H.M., Li, C.N., 2008. A Permian layered intrusive complex in the Western Tarim Block, Northwestern China: Product of a ca. 275-Ma mantle Plume? The Journal of Geology 116, 269–287. doi:10.1086/587726

Zhang, Y., Liu, J., Guo, Z., 2010. Permian basaltic rocks in the Tarim basin, NW China: Implications for plume–lithosphere interaction. Gondwana Research 18, 596–610. doi:10.1016/j.gr.2010.03.006

Zhang, D., Zhou, T., Yuan, F., Jowitt, S.M., Fan, Y., Liu, S., 2012. Source, evolution and emplacement of Permian Tarim Basalts: Evidence from U-Pb dating, Sr-Nd-Pb-Hf isotope

systematics and whole rock geochemistry of basalts from the Keping area, Xinjiang Uygur Autonomous region, northwest China. Journal of Asian Earth Sciences 49, 175–190. doi:10.1016/j.jseaes.2011.10.018

Zhang, C.L., Zou, H.-B., Li, H.-K., Wang, H.-Y., 2013a. Tectonic framework and evolution of the Tarim Block in NW China. Gondwana Research 23, 1306–1315. doi:10.1016/j.gr.2012.05.009

Zhang, Z., Deng, Y., Chen, L., Wu, J., Teng, J., Panza, G., 2013b. Seismic structure and rheology of the crust under mainland China. Gondwana Research 23, 1455–1483. doi:10.1016/j.gr.2012.07.010

Zhang, J.X., Mattinson, C.G., Yu, S.Y., Li, Y.S., 2014a. Combined rutile–zircon thermometry and U–Pb geochronology: New constraints on Early Paleozoic HP/UHT granulite in the south Altyn Tagh, north Tibet, China. Lithos 200-201, 241–257. doi:10.1016/j.lithos.2014.05.006

Zhang, T., Fang, X., Song, C., Appel, E., Wang, Y., 2014b. Cenozoic tectonic deformation and uplift of the South Tian Shan: Implications from magnetostratigraphy and balanced cross-section restoration of the Kuqa depression. Tectonophysics 628, 172–187. doi:10.1016/j.tecto.2014.04.044

Zhang, Z., Zhu, W., Zheng, D., Zheng, B., Yang, W., 2016. Apatite fission track thermochronology in the Kuluketage and Aksu areas, NW China: Implication for tectonic evolution of the northern Tarim. Geoscience Frontiers 7, 171–180. doi:10.1016/j.gsf.2015.08.007

Zhang, S., Hu, X., Han, Z., Li, J., Garzanti, E., 2018. Climatic and tectonic controls on Cretaceous-Palaeogene sea-level changes recorded in the Tarim epicontinental sea. Palaeogeography, Palaeoclimatology, Palaeoecology 501, 92–110. doi:10.1016/j.palaeo.2018.04.008

Zhao, B., Wang, X., 2016. Evidence of early passive diapirism and tectonic evolution of salt structures in the western Kuqa depression (Quele area), southern Tianshan (NW China). Journal of Asian Earth Sciences 125, 138–151. doi:10.1016/j.jseaes.2016.05.021

Zhao, H., Wei, Y., Shen, Y., Xiao, A., Mao, L., Wang, L., Guan, J., Wu, L., 2016. Cenozoic tilting history of the south slope of the Altyn Tagh as revealed by seismic profiling: Implications for the kinematics of the Altyn Tagh fault bounding the northern margin of the

Tibetan Plateau. Geosphere 12, 884–899. doi:10.1130/GES01269.1

Zheng, H., Wei, X., Tada, R., Clift, P.D., Wang, B., Jourdan, F., Wang, P., He, M., 2015. Late Oligocene–early Miocene birth of the Taklimakan Desert. Proceedings of the National Academy of Sciences USA 112, 7662–7667. doi:10.1073/pnas.1424487112

Zhou, D., Graham, S.A., Chang, E.Z., Wang, B., Hacker, B., 2001. Paleozoic tectonic amalgamation of the Chinese Tian Shan: Evidence from a transect along the Dushanzi-Kuqa Highway. In: Hendrix, M.S., Davis, G.A. (Eds.), Paleozoic and Mesozoic Tectonic Evolution of Central Asia. Geological Society of America Memoir 194, pp. 23–46.

Zhu, G.Y., Ren, R., Chen, F.-R., Li, T.-T., Chen, Y.-Q., 2017. Neoproterozoic rift basins and their control on the development of hydrocarbon source rocks in the Tarim Basin, NW China. Journal of Asian Earth Sciences 150, 63–72. doi:10.1016/j.jseaes.2017.09.018

Zubovich, A.V., Wang, X.-Q., Scherba, Y.G., Schelochkov, G.G., Reilinger, R., Reigber, C., Mosienko, O.I., Molnar, P., Michajljow, W., Makarov, V.I., Li, J., Kuzikov, S.I., Herring, T.A., Hamburger, M.W., Hager, B.H., Dang, Y.-M., Bragin, V.D., Beisenbaev, R.T., 2010. GPS velocity field for the Tien Shan and surrounding regions. Tectonics 29, 1–23. doi:10.1029/2010TC002772

Figure captions

Figure 1: Geographical and geological setting of the Tarim area and location of the data used in this study. Only the main structures outcropping at the surface are represented. References for the data from previous studies are indicated in the bottom-right insert. Green long-dashed lines locate the regional balanced geological transects A, B, C and D presented in Figure 7. Green short-dashed lines at terminations of transects B and C correspond to the extended pathway of the synthetic crustal-scale cross-sections presented in Figure 13. ATF: Altyn Tagh Fault, BF: Baluntay Fault, KFX: Karakax Fault, KGS: Kongur Shan normal fault, NF: Narat Fault, NL: Nikolaev Line, TFF: Talas Ferghana Fault, VSP: Vertical Seismic Profile. In this study, the Tarim block refers to the area comprised in between the Paleozoic ophiolitic sutures (thick red lines) displayed in the surrounding ranges, rather than to the present-day Tarim Basin only. These sutures located within the Western Kunlun, Altyn Tagh and Southern Tian Shan ranges

correspond to the Oytag-Kudi, Lapeiquan-Hongliugou, and South Tian Shan sutures, respectively.

Figure 2: Simplified chronostratigraphic chart of the Tarim Basin, Western Kunlun Range and Southern Tian Shan. Black arrows represent the main decollement levels in the Tarim area, while colour lines correspond to the seismic horizons picked for this study.

Figure 3: Velocity functions used for time-to-depth conversion of the seismic interpretations. For each sediment package (Sinian-Paleozoic, Permian-Mesozoic and Cenozoic), these velocity functions are composed of two parts: (1) an upper part (solid line) corresponding to a single linear regression of the vertical seismic profiles of P-wave data (brown, green and yellow crosses) from four wells distributed across the Tarim Basin (red dots in Fig. 1), and (2) a lower part (dashed line) corresponding to a maximum velocity determined according to the main lithology of the sediment package (calcareous for the Sinian-Paleozoic deposits, terrigenous for the Permian-Mesozoic and Cenozoic series).

Figure 4: Example of surface data and the associated detailed work on the Qimugen fold-thrust system (see Fig. 1 for location). (A) Satellite image (Landsat images with a 28-m resolution) of the Qimugen hills. (B) Geological and structural map of the same area constructed from field data, satellite images and seismic profiles. (C) Field picture of the Qimugen hills taken from the south. (D) Field picture of the Qimugen hills taken from the southeast. (E) Surface geological cross-section of the Qimugen hills with a vertical exaggeration (VE) of 2.

Figure 5: Example of surface data and the associated detailed work on the eastern part of the Mazar Tagh emergent thrust ramps and deep fault system (see Fig. 1 for location). (A) Satellite image (Landsat images with a 28-m resolution) of the Mazar Tagh ridge. (B) Geological and structural map of the same area constructed from field data, satellite images and seismic profiles. (C) Field picture of the Mazar Tagh ridge taken from the south. (D) Field picture of the eastern termination of the Mazar Tagh ridge taken from the northeast. The light-colored deposits to the right correspond to the Cenozoic (Paleocene-Eocene) evaporitic decollement of the southwestern Tarim Basin, which crops out at the top of the local Mazar Tagh emergent thrust ramp. (E)

Surface geological cross-section of the eastern termination of the Mazar Tagh ridge with a vertical exaggeration (VE) of 2 (modified from Pan et al., 2010).

Figure 6: Structural map of the Cenozoic deformation of the Tarim Basin and surrounding ranges. Simplified and abbreviated structure labels are spelled out in the upper right cartoon. (A) Structures outcropping at the surface only. (B) Structures outcropping at the surface and hidden below the Cenozoic sediments of the Tarim Basin. Structures rooted in the basement are represented in red, while structures rooted into a sedimentary decollement are displayed in orange (for structures developed above Paleozoic decollements) or in yellow (for structures developed above Cenozoic decollements). Green solid lines locate the regional balanced geological transects A, B, C and D presented in Figure 7. Green dashed lines at terminations of transects B and C correspond to the extended pathway of the synthetic crustal-scale cross-sections presented in Figure 13. In this study, the Tarim block refers to the area comprised between the Paleozoic ophiolitic sutures (thick black lines) located in the surrounding ranges, rather than to the present-day Tarim Basin only.

Figure 7: Regional balanced geological transects across the Tarim Basin and surrounding ranges (see Figs. 1 or 6 for location, Fig. 6 for abbreviation labels, and Fig. S3 for a 1:2,000,000-scale version). Below each transect, a restored state at the beginning of the Cenozoic is presented. For these restorations, the fixed reference lines (red pins) are located at the turning point in the centre of sections, and the lighter thrust slices in the range interiors are not considered. Shortening amounts (black bold numbers) measured on each side of the fixed reference lines are indicated to the northern and southern ends of the restored transects.

Figure 8: Details of the regional balanced geological transects across the southern part of the Tarim Basin and the Western Kunlun and Altyn Tagh ranges (see Fig. 7 for location and Fig. 6 for abbreviation labels).

Figure 9: Details of the regional balanced geological transect B across the central part of the Tarim Basin (see Fig. 7 for location and Fig. 6 for abbreviation labels).

Figure 10: Details of the regional balanced geological transects across the northern part of the Tarim Basin and the Southern Tian Shan Range (see Fig. 7 for location and Fig. 6 for abbreviation labels).

Figure 11: Tectonic map of the Cenozoic deformation of the Tarim Basin and surrounding ranges. Structures rooted in the basement are represented in red, while structures rooted into a sedimentary decollement are displayed in orange (for structures developed above a Paleozoic decollement) or in yellow (for structures developed above a Cenozoic decollement). Areas comprising Proterozoic and (Protero-)Paleozoic inherited basement structures reactivated during the Cenozoic orogeny are indicated in light and dark grey, respectively. Regions with Cenozoic neo-formed cover structures are shown in orange (for structures developed above a Paleozoic decollement) or in yellow (for structures developed above a Cenozoic decollement). Green solid lines locate the regional balanced geological transects A, B, C and D presented in Figure 7. Green long-dashed lines at terminations of these transects correspond to the extended pathway of the simplified crustal-scale cross-sections presented in Figure S6, which are used to assess the shortening accommodated across the ranges from crustal budgets (see Fig. 12 and Supplementary information S5 for methodology). Green arrows and values at the ends of these cross-sections represent and scale with the most probable (solid line) and possible maximum (short-dashed line and bracketed numbers) values for the total Cenozoic shortening estimated along these transects (Table 1). Ptz: Proterozoic, Pz: Paleozoic, Mz: Mesozoic, Cz: Cenozoic. In this study, the Tarim block refers to the area comprised between the Paleozoic ophiolitic sutures (thick black lines) located in the surrounding ranges, rather than to the present-day Tarim Basin only.

Figure 12: Components for the crustal-scale cross-sections presented in Figures 13 and S6 (see Fig. 6 for abbreviation labels). (A) Example of an elevation profile extracted from the SRTM3 DEM and averaged every 50 km in the range (green dashed line). This average topography corresponds to the main input for assessing the Moho depth below the ranges by isostatic calculations. (B) Example of a simplified crustal-scale cross-section used to estimate the shortening accommodated across the ranges surrounding the Tarim Basin from crustal budgets (see Supplementary information S5 for methodology). To assess the Moho depth below the

ranges by isostatic calculations, a reference in a stable place (i.e. with no Cenozoic deformation or flexure) is required. This stable isostatic reference was taken in the centre of the basin, between kilometres 300 and 350 along transect C, where there is no structures activated during the Cenozoic (Figs. 7C and S6C1). A_{range}: crustal area below the range, A_{sed}: area of the Cenozoic sediments coming from the range erosion (i.e. crustal area of the range lost by erosion), H_0: initial crustal thickness at the beginning of Cenozoic, L_1: present-day length of the range, L_0: initial crustal length at the beginning of Cenozoic, d: density. (C) Intermediate state of construction for the synthetic crustal-scale cross-sections. Structures from the surface down to 20 km deep are constrained by the regional balanced geological transects (Fig. 7B). Structures below 20 km deep are inferred from the isostatic calculations and the basin geometry achieved in this study, and from the deep geophysical data available in the area (e.g., Li et al., 2002b; Jiang et al., 2004; Wittlinger et al., 2004). Examples of a lithospheric yield strength profile (from Zhang et al., 2013b) and of earthquake frequency according to depth (from Sloan et al., 2011) below the Tarim Basin. ε: deformation rate, q: heat flux, n: number of earthquakes.

Figure 13: Possible synthetic crustal-scale cross-sections across the Tarim Basin, Western Kunlun Range and Southern Tian Shan (see Fig. 6 for location and abbreviation labels). (A) and (B) Cross-sections with the basement-cored uplifts in the basin rooted into a crustal decollement (in the middle or at the base of the crust, respectively). These interpretations are favoured due to their consistency with the geological and geophysical data available so far in the area (see text for more explanations). (C) Alternative cross-section with the large basement-cored uplifts in the basin rooted into the mantle. In this study, the Tarim block refers to the area comprised between the Paleozoic ophiolitic sutures (thick black lines) located in the surrounding ranges, rather than to the present-day Tarim Basin only.

Table 1: Shortening estimates across the Tarim Basin and surrounding ranges. Shortening values are provided for (1) the entire (inner plus outer) ranges, (2) the inner ranges, (3) the outer ranges, (4) the basin, and (5) the entire orogenic systems. Shortening values for the entire ranges (1) are derived from crustal budgets (Figs. 12 and S6; Supplementary material S5). Those for the outer ranges (3) and for the basin (4) are derived from structural restorations (Fig. 7). For the outer ranges, the contributions to the shortening of the (Protero-)Paleozoic inherited (inh.) and

Cenozoic neo-formed (neo.) structures are indicated in brackets. Shortening values for the inner ranges (2) correspond to the differences between the shortenings across the entire ranges (1) and those accumulated in their outer parts (3). Finally, the total shortening amounts accommodated across the whole orogenic systems (5) are obtained by adding the shortening values accommodated across the entire ranges (1) and in the basin (4). Values given for shortenings derived from crustal budgets correspond to the most probable values according to our regional balanced geological transects (Cenozoic sediment thicknesses) and other published parameters (densities and sediment porosity) used for calculations. Uncertainties given for these values correspond to possible errors on the crustal areas below the range (coming from the densities) and on the crustal areas lost by erosion (coming from the sediment porosity) (see Supplementary information S5 for more explanations).

Supplementary materials

Figure S1: Georeferenced structural map (in GeoTIFF format) of the Cenozoic deformation of the Tarim Basin and surrounding ranges (see Fig. 6 for abbreviation labels). All structures are represented, whether they are outcropping at the surface or hidden below the Cenozoic sediments of the basin. Structures rooted in the basement are represented in red, while structures rooted into a sedimentary decollement are displayed in orange (for structures developed above a Paleozoic decollement) or in yellow (for structures developed above a Cenozoic decollement).

Figure S2: Examples of seismic profiles and interpretations used to construct the regional balanced geological transects presented in Figures 7, 8, 9, 10, and S3 (see Fig. 6 for abbreviation labels). The location of these profiles is given in the top map insert (same legend as in Fig. 1).

Figure S3: Regional balanced geological transects across the Tarim Basin and surrounding ranges at a scale of 1:2,000,000 (see Fig. 6 for location and abbreviation labels). The main data used to construct these cross-sections are specified above each transect. References are listed in Supplementary information S4.

Information S4: Discussion about some structural interpretation issues.

Information S5: Methodology used to assess the shortening accommodated in the ranges surrounding the Tarim Basin from crustal budgets.

Figure S6: Simplified crustal-scale cross-sections used to assess the shortening accommodated across the ranges surrounding the Tarim Basin from crustal budgets (see Fig. 12 and Supplementary information S5 for methodology). Green solid lines in the top-centre map insert (same legend as in Fig. 11) locate these cross-sections, green dashed lines in between correspond to the initial pathway of the regional balanced geological transects (see also Figs. 1, 6 and 11) presented in Figures 7 and S3. Orange rectangles on the cross-sections correspond to the Moho locations published from deep geophysical data, with the associated references quoted to the right or to the left. Orange dashed rectangles are the out-of-trend Moho locations with the associated references marked with an asterisk. All these references are listed in Supplementary information S5. A_{range}: crustal area below the range, A_{sed}: area of the Cenozoic sediments coming from the range erosion (i.e. crustal area of the range lost by erosion), H_0: initial crustal thickness at the beginning of Cenozoic, L_1: present-day length of the range, L_0: initial crustal length at the beginning of Cenozoic. In this study, the Tarim block refers to the area comprised between the Paleozoic ophiolitic sutures located in the surrounding ranges, rather than to the present-day Tarim Basin only.

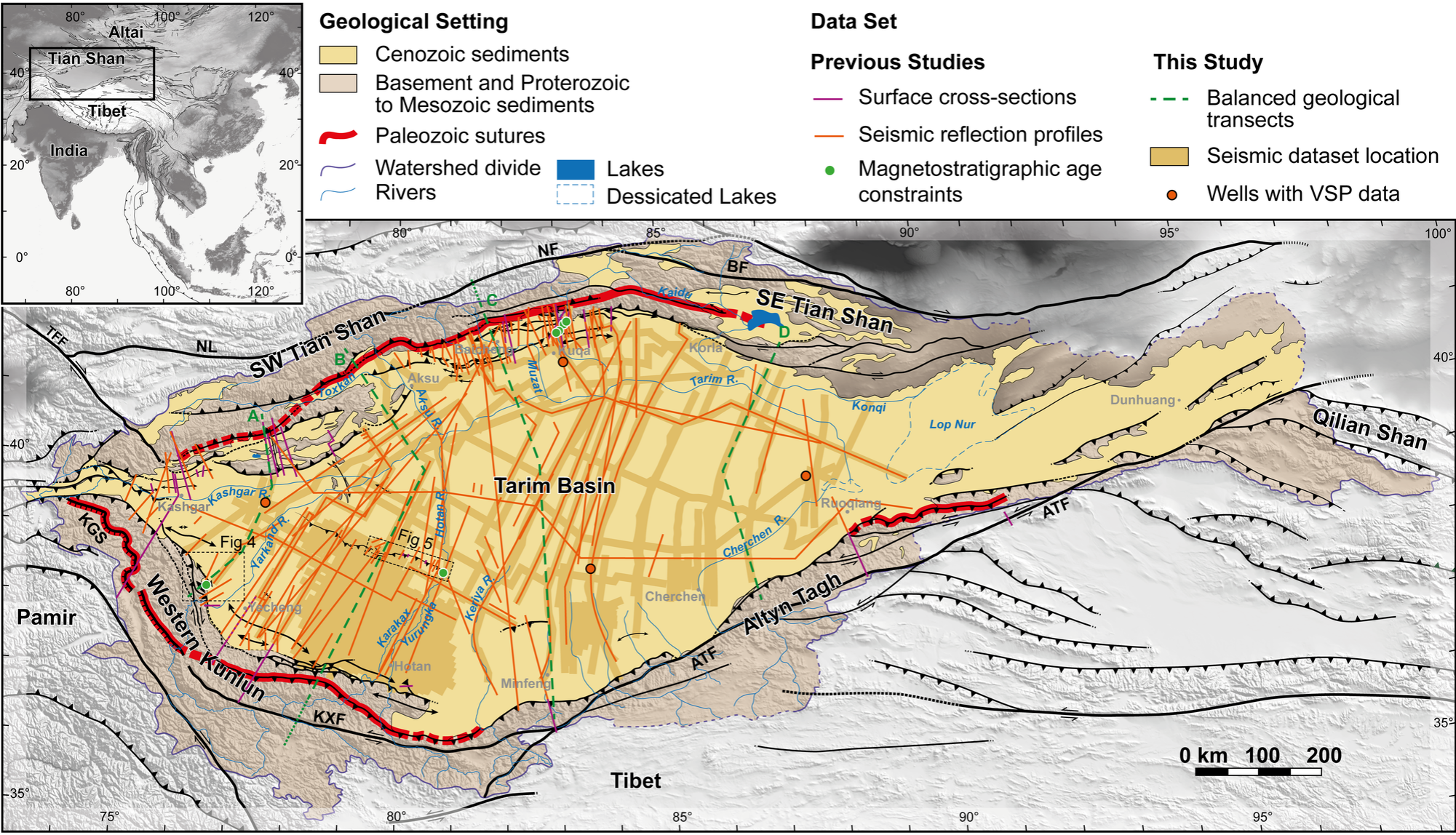

Allen et al., 1999; Blayney et al., 2019; Bosboom et al., 2014a; Burchfield et al., 1999; Chang et al., 2016a, 2017; Charreau et al., 2006, 2009; Chen et al., 2004; Cheng et al., 2016b; Cowgil, 2010; Fan et al., 2008; Fu et al., 2010; Guilbaud et al., 2017; Guo et al., 2016; He et al., 2005; He et al., 2016; Heermance et al., 2007, 2008; Huang et al., 2006, 2010; Hubert-Ferrari et al., 2007; Izquierdo-Llavall et al., 2018; Jia et al., 1998; Jiang et al., 2013; Jiang and Li, 2014; Jiang et al., 2018; Jin et al., 2008; Li et al., 1996; Li et al., 2002a; Li et al., 2012a; Li et al., 2012b; Li et al., 2013; Li et al., 2015c, 2015d, 2016c, 2016d, 2016e; Li et al., 2016b, 2018b; Lin et al., 2012b, 2012c; Lin et al., 2015a; Liu et al., 2015a; Lu et al., 2016; Matte et al., 1996; Neng et al., 2018; Pan et al., 2010; Peng et al., 2006; Qi et al., 2009; Qiu et al., 2011; Scharer et al., 2004; Sobel et al., 2006; Sun et al., 2009a, 2009b, 2017; Tang et al., 2014; Tang et al., 2017; Thompson et al., 2017; Tian et al., 2016; Tong et al., 2012; Turner et al., 2010; Wang et al., 2013; Wang and Wang, 2016; Wang et al., 2016b; Wang et al., 2017; Wei et al., 2013; Wen et al., 2017; Wu et al., 2014; Xie et al., 2017; Xu and Zhou, 2007; Yang et al., 2007a; Yang et al., 2007b; Yang et al., 2009; Yang et al., 2015; Yang et al. 2018b; Yin et al., 1998; Yin et al., 2002; Yu et al., 2014; Zeng et al., 2010; Zhang et al. 2014b; Zhao and Wang, 2016; Zheng et al., 2015

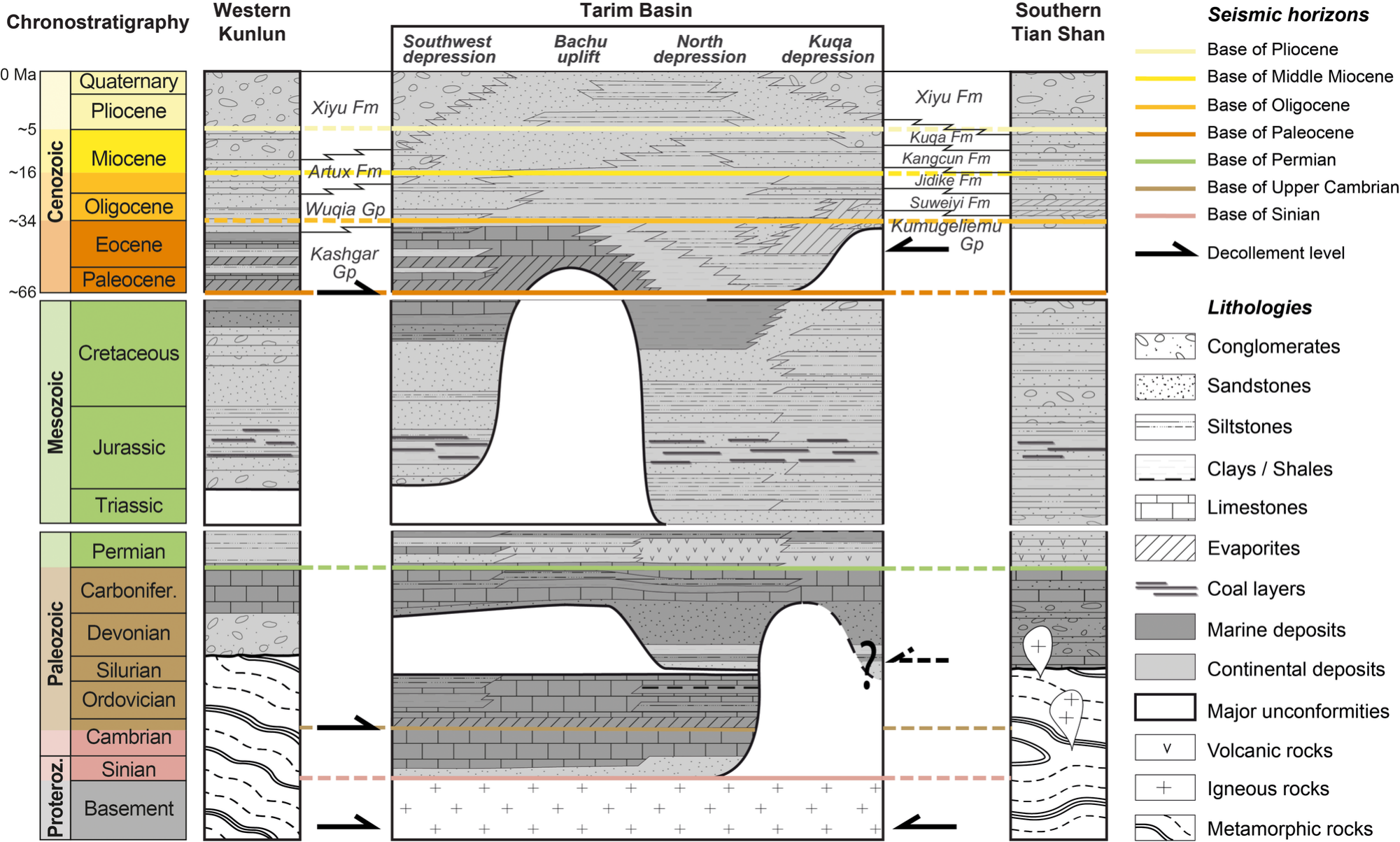
Chronostratigraphy
Western Kunlun
Tarim Basin
Southwest depression
Bachu uplift
North depression
Kuqa depression
Southern Tian Shan
0 Ma
~5
~16
~34
~66
Cenozoic
Quaternary
Pliocene
Miocene
Oligocene
Eocene
Paleocene
Mesozoic
Cretaceous
Jurassic
Triassic
Paleozoic
Permian
Carbonifer.
Devonian
Silurian
Ordovician
Cambrian
Proteroz.
Sinian
Basement
Xiyu Fm
Artux Fm
Wuqia Gp
Kashgar Gp
Xiyu Fm
Kuqa Fm
Kangcun Fm
Jidike Fm
Suweiyi Fm
Kumugeliemu Gp
?
Seismic horizons
Base of Pliocene
Base of Middle Miocene
Base of Oligocene
Base of Paleocene
Base of Permian
Base of Upper Cambrian
Base of Sinian
Decollement level
Lithologies
Conglomerates
Sandstones
Siltstones
Clays / Shales
Limestones
Evaporites
Coal layers
Marine deposits
Continental deposits
Major unconformities
Volcanic rocks
Igneous rocks
Metamorphic rocks

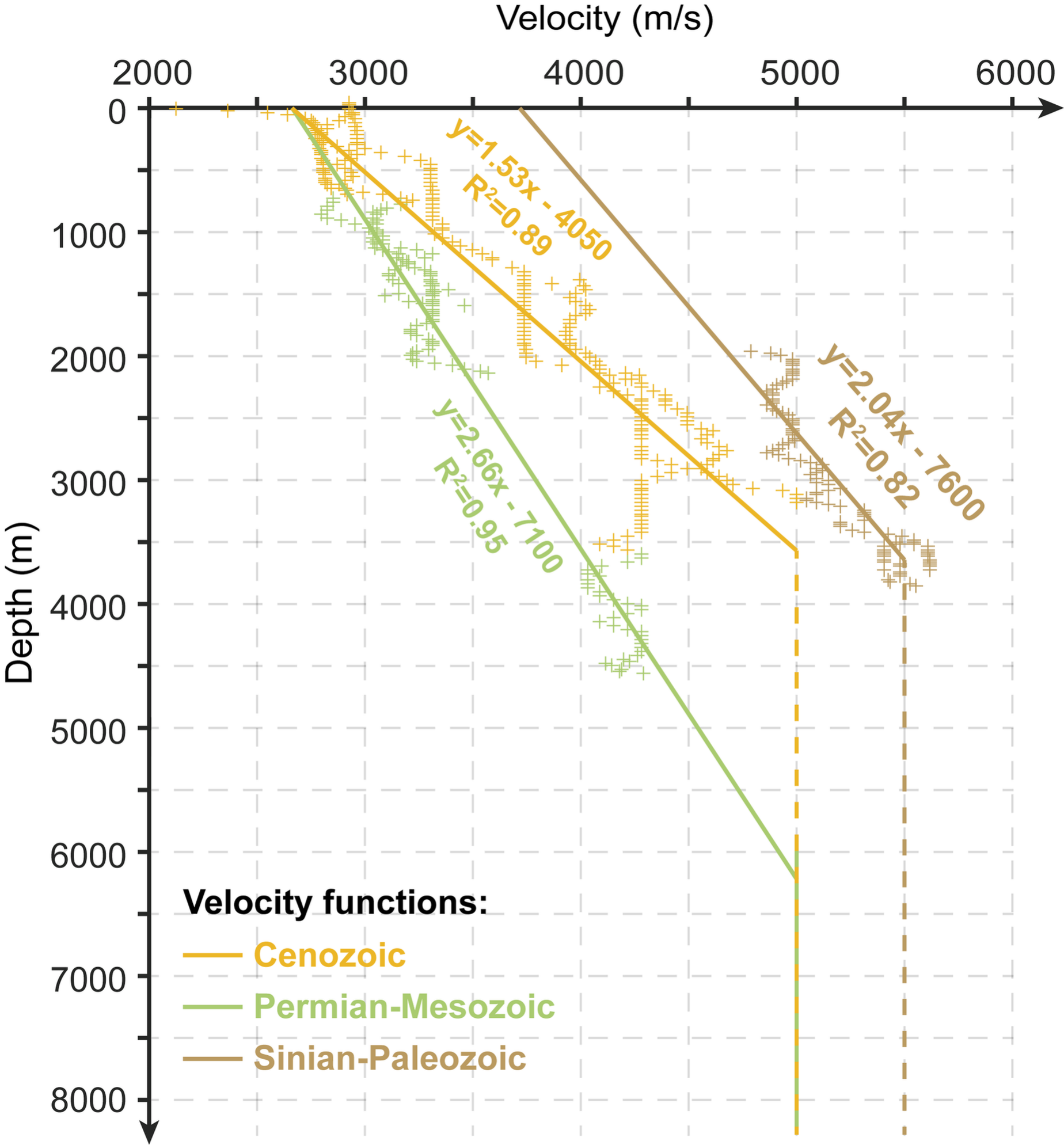
Velocity (m/s)
2000
3000
4000
5000
6000
0
1000
2000
3000
4000
5000
6000
7000
8000
Depth (m)
y=1.53x - 4050
R²=0.89
y=2.66x - 7100
R²=0.95
y=2.04x - 7600
R²=0.82
Velocity functions:
Cenozoic
Permian-Mesozoic
Sinian-Paleozoic

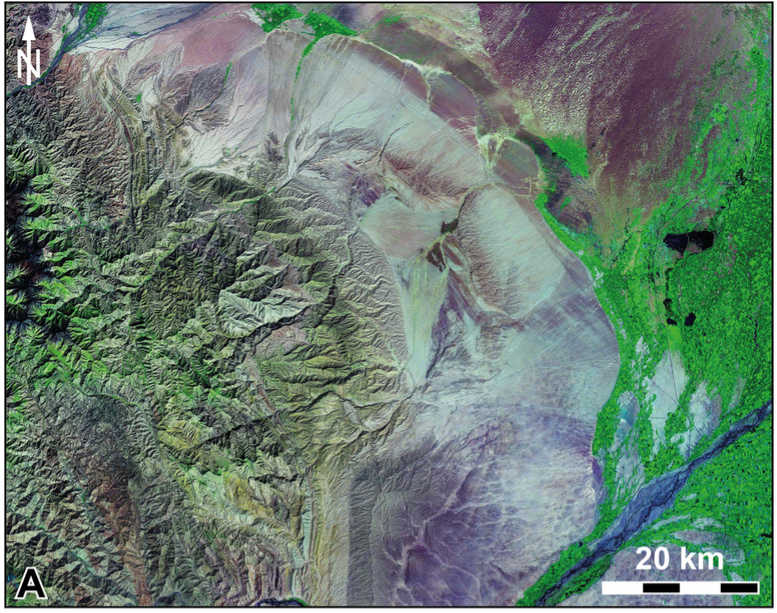

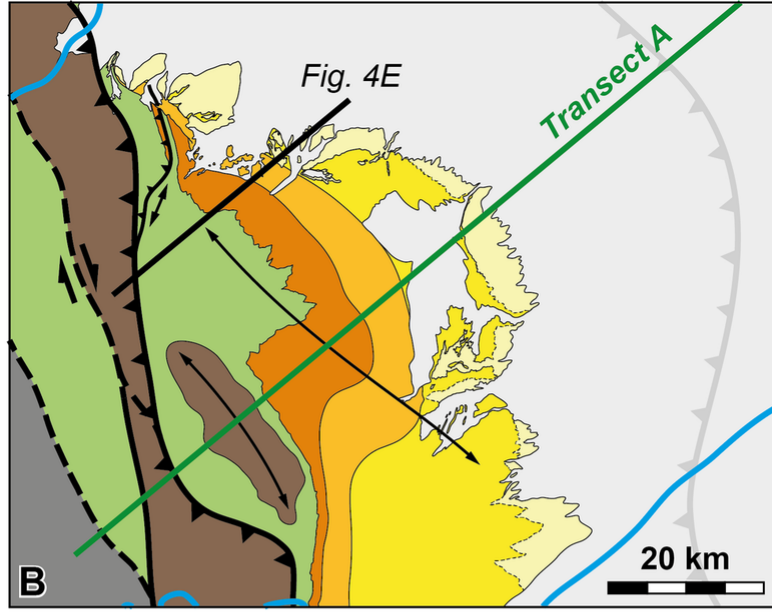

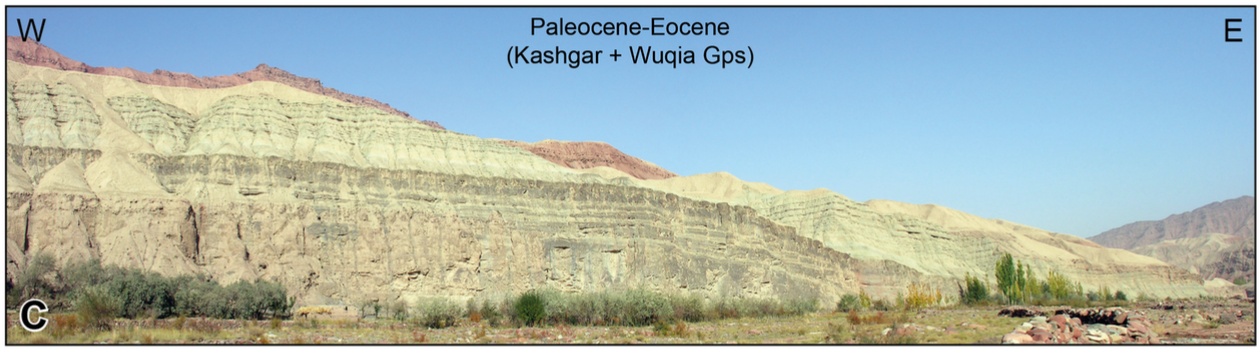

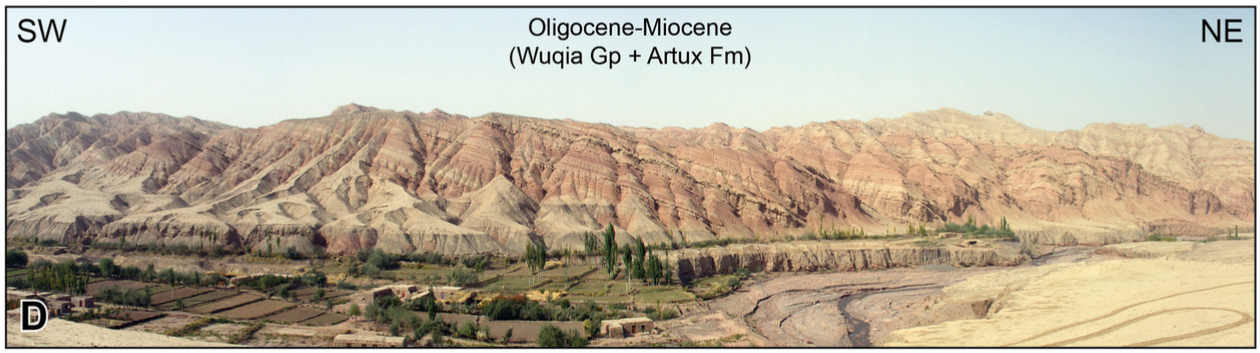

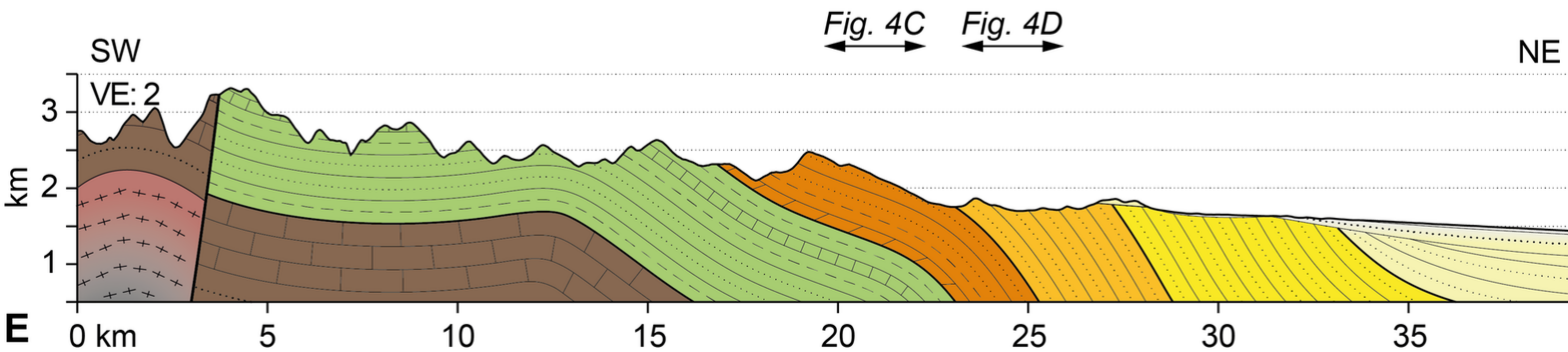

Devonian to Carboniferous
Sinian to Silurian meta-sediments
Proterozoic basement
Blind faults
Emergent faults
Quaternary (grey Xiyu Fm)
Pliocene (orange to blue-grey Artux and grey Xiyu Fms)
Oligocene - Miocene (light red Wuqia Gp + orange Artux Fm)
Paleocene - Eocene (bleu-grey Kashgar + dark red Wuqia Gps)
Permian - Mesozoic

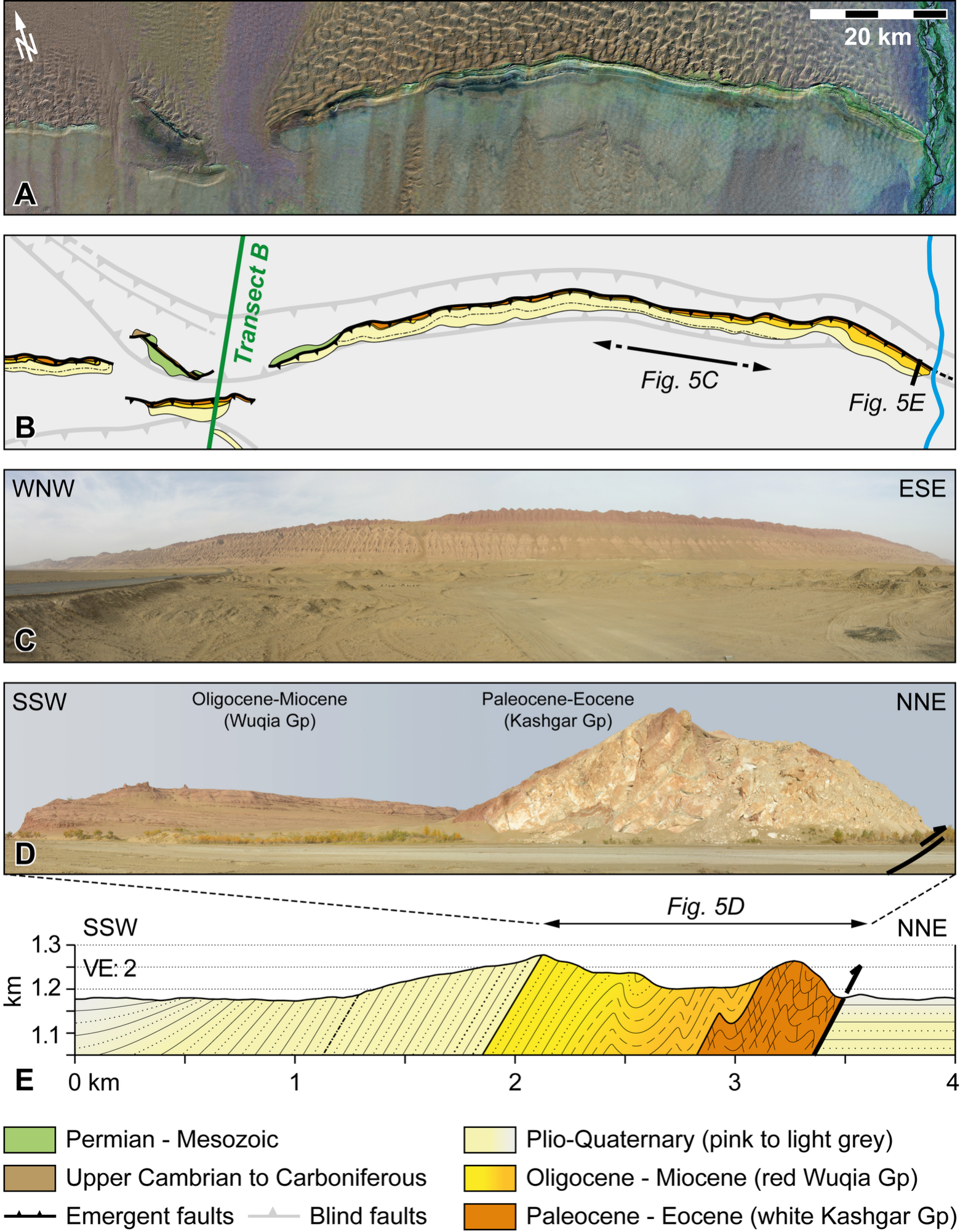
N
20 km
A
Transect B
B
Fig. 5C
Fig. 5E
WNW
ESE
C
SSW
Oligocene-Miocene
(Wuqia Gp)
Paleocene-Eocene
(Kashgar Gp)
NNE
D
Fig. 5D
SSW
NNE
VE: 2
km
1.3
1.2
1.1
E
0 km
1
2
3
4
Permian - Mesozoic
Upper Cambrian to Carboniferous
Emergent faults
Blind faults
Plio-Quaternary (pink to light grey)
Oligocene - Miocene (red Wuqia Gp)
Paleocene - Eocene (white Kashgar Gp)

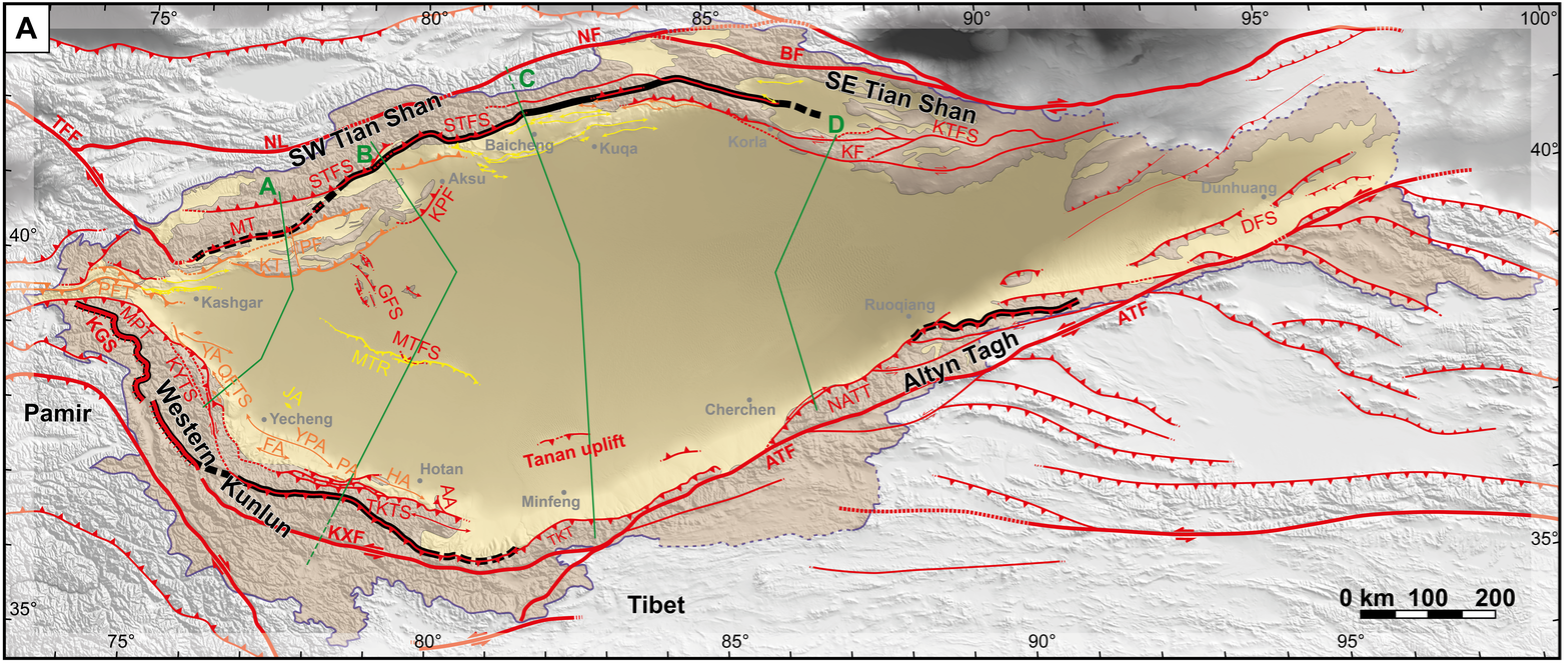

AA: Aqike Anticline, ATF: Altyn Tagh Fault, ATS: Aqia Thrust System, Bayan. B: Bayanbulak Basin, BF: Baluntay Fault, CFS: Cherchen Fault System, DFS: Dunhuang Fault System, FA: Fusha Anticline, GFS: Gudongshan Fault System, HA: Hotan Anticline, JA: Jiede Anticline, KAB: Kashgar-Artux Belt, KADF: Kashgar-Artux Deformation Front, KEB: Kepingtage Belt, KF: Korla Fault, KGS: Kongur Shan normal fault, Korla B: Korla Basin, KPB: Kalpin Belt, KPF: Kalpintagh Fault; KT: Kepingtage Thrust, KTFS: Kuruk Tagh Fault System, KUB + dep: Kuqa Belt + Kuqa depression, KUDF: Kuqa Deformation Front, KXF: Karakax Fault, KYTS: Kashgar-Yecheng Transfer System, LNFS: Lop Nur Fault System, MFS: Minfeng Fault System, MPT: Main Pamir Thrust, MT: Muziduke Thrust, MTFS and MTR: Mazar Tagh deep Fault System and emergent thrust Ramps, NATT: Northern Altyn Tagh Thrust, N dep.: North depression, NF: Narat Fault, NFS: Niya Fault System, NL: Nikolaev Line, PA: Pusikai Anticline, PF: Piqiang Fault, PFT: Pamir Frontal Thrust, QFTS: Qimugen Fold-Thrust System, RFS: Ruoqiang Fault System, SE dep.: Southeast depression, SFS: Selibuya Fault System, STFS: Southern Tian Shan Fault System, SW dep.: Southwest depression, TFF: Talas Ferghana Fault, TKT: Tam Karaul Thrust, TKTS: Tiklik Thrust System, TTS: Tumuxiuke Thrust System, WFTS: Wupoer Fold-Thrust System, WKFR: Western Kunlun Frontal blind Ramp, YPA: Yecheng-Pishan Anticline, YA: Yingisar Anticline

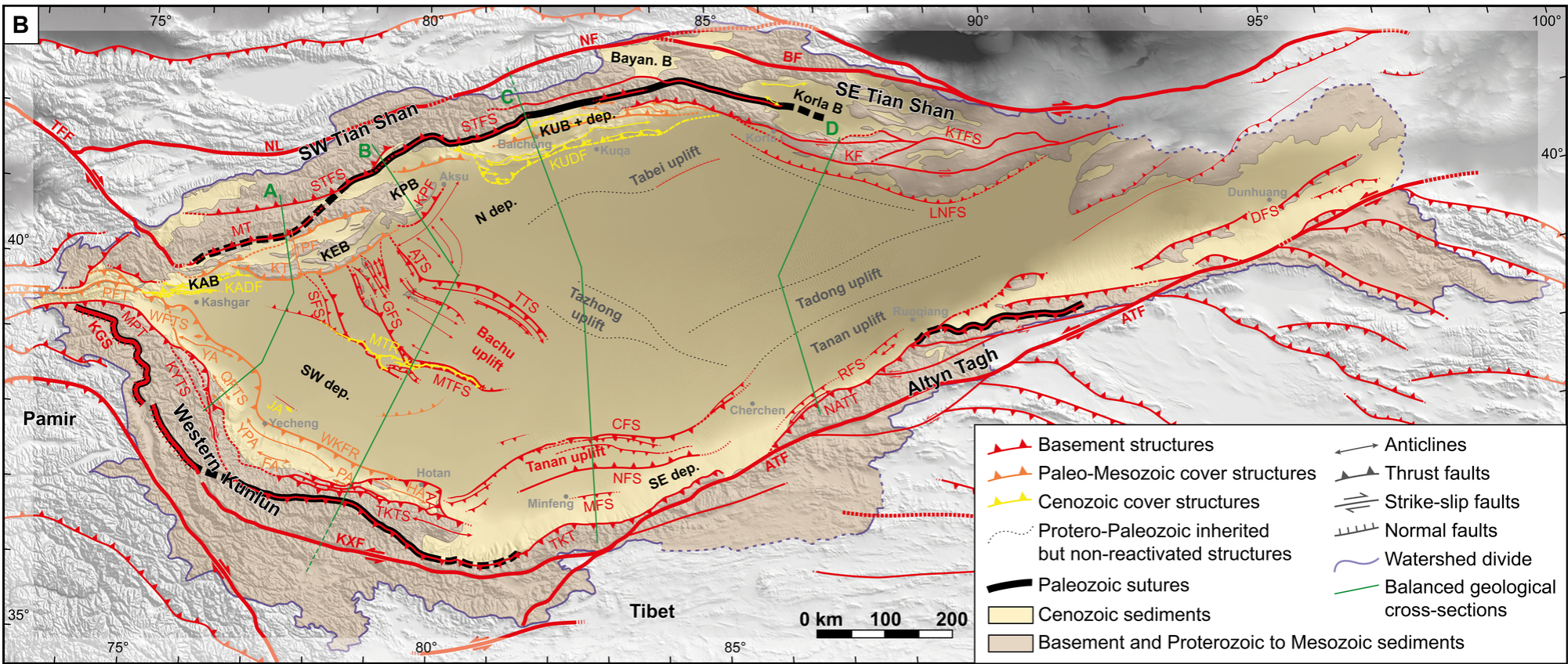

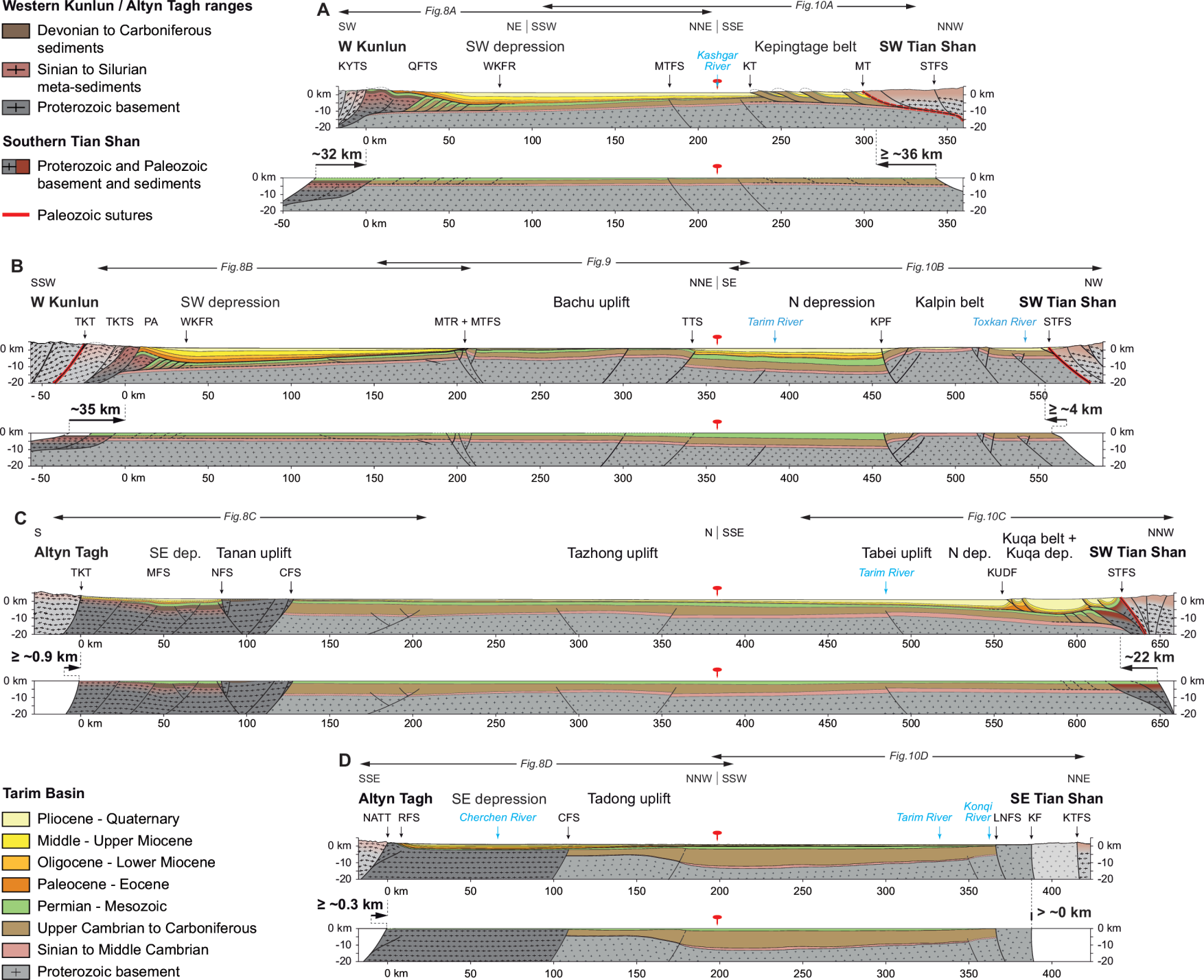
Western Kunlun / Altyn Tagh ranges
Devonian to Carboniferous sediments
Sinian to Silurian meta-sediments
Proterozoic basement
Southern Tian Shan
Proterozoic and Paleozoic basement and sediments
Paleozoic sutures
A
Fig.8A
Fig.10A
SW
NE | SSW
NNE | SSE
NNW
W Kunlun
SW depression
Kepingtage belt
SW Tian Shan
KYTS
QFTS
WKFR
MTFS
Kashgar River
KT
MT
STFS
~32 km
≥ ~36 km
B
Fig.8B
Fig.9
Fig.10B
SSW
NNE | SE
NW
W Kunlun
SW depression
Bachu uplift
N depression
Kalpin belt
SW Tian Shan
TKT
TKTS
PA
WKFR
MTR + MTFS
TTS
Tarim River
KPF
Toxkan River
STFS
~35 km
≥ ~4 km
C
Fig.8C
Fig.10C
S
N | SSE
NNW
Altyn Tagh
SE dep.
Tanan uplift
Tazhong uplift
Tabei uplift
N dep.
Kuqa belt + Kuqa dep.
SW Tian Shan
TKT
MFS
NFS
CFS
Tarim River
KUDF
STFS
≥ ~0.9 km
~22 km
D
Fig.8D
Fig.10D
SSE
NNW | SSW
NNE
Altyn Tagh
SE depression
Tadong uplift
SE Tian Shan
NATT
RFS
Cherchen River
CFS
Tarim River
Konqi River
LNFS
KF
KTFS
≥ ~0.3 km
> ~0 km
Tarim Basin
Pliocene - Quaternary
Middle - Upper Miocene
Oligocene - Lower Miocene
Paleocene - Eocene
Permian - Mesozoic
Upper Cambrian to Carboniferous
Sinian to Middle Cambrian
Proterozoic basement

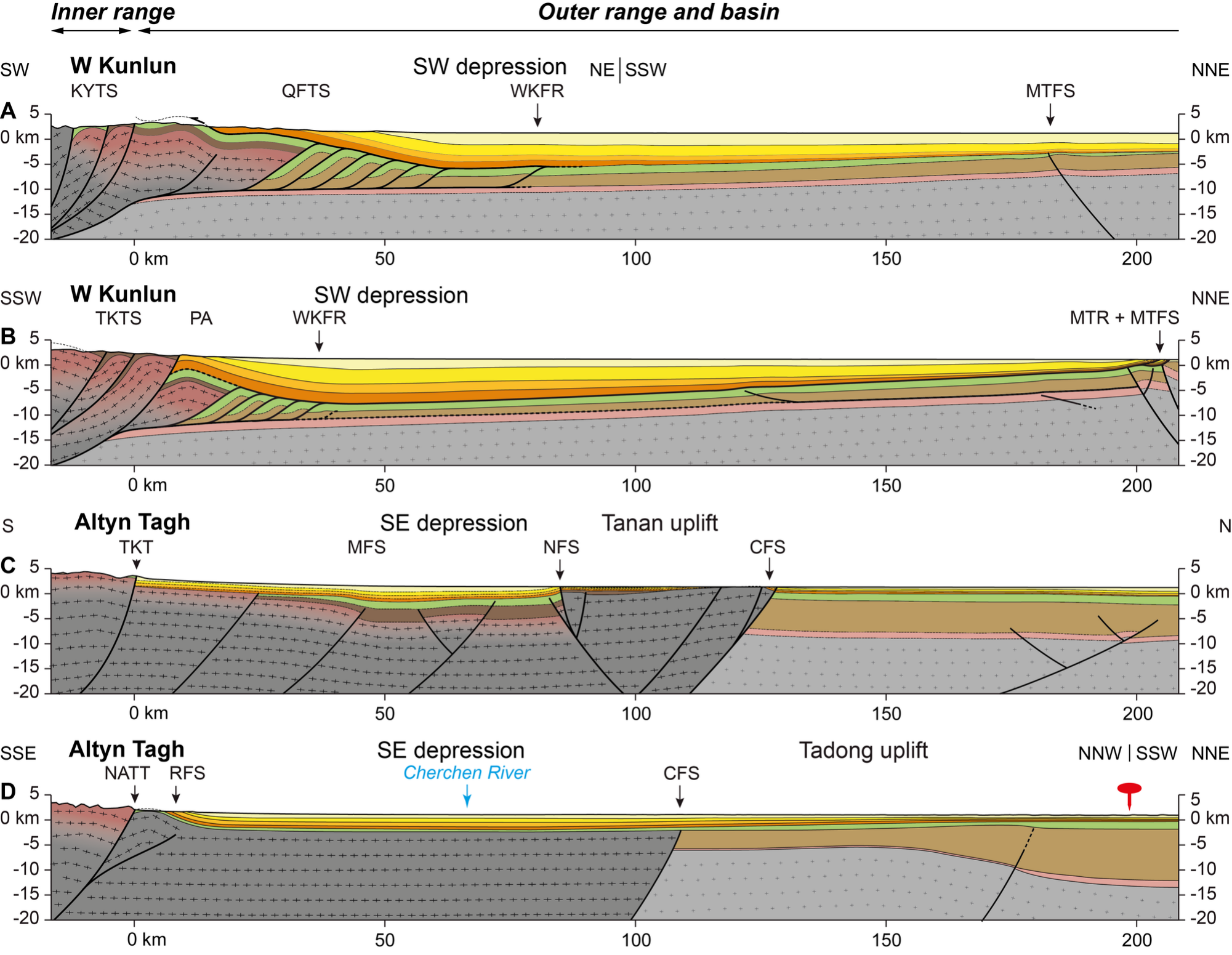
Inner range
Outer range and basin
SW
W Kunlun
KYTS
QFTS
SW depression
WKFR
NE | SSW
MTFS
NNE
A
5
0 km
-5
-10
-15
-20
0 km
50
100
150
200
SSW
W Kunlun
TKTS
PA
SW depression
WKFR
MTR + MTFS
NNE
B
S
Altyn Tagh
TKT
MFS
SE depression
NFS
Tanan uplift
CFS
N
C
SSE
Altyn Tagh
NATT
RFS
SE depression
Cherchen River
CFS
Tadong uplift
NNW | SSW
NNE
D
Western Kunlun / Altyn Tagh ranges
Proterozoic basement
Sinian to Silurian meta-sediments
Devonian to Carboniferous sediments
Tarim Basin
Sinian to Middle Cambrian
Permian - Mesozoic
Oligocene - Lower Miocene
Pliocene - Quaternary
Proterozoic basement
Upper Cambrian to Carboniferous
Paleocene - Eocene
Middle - Upper Miocene

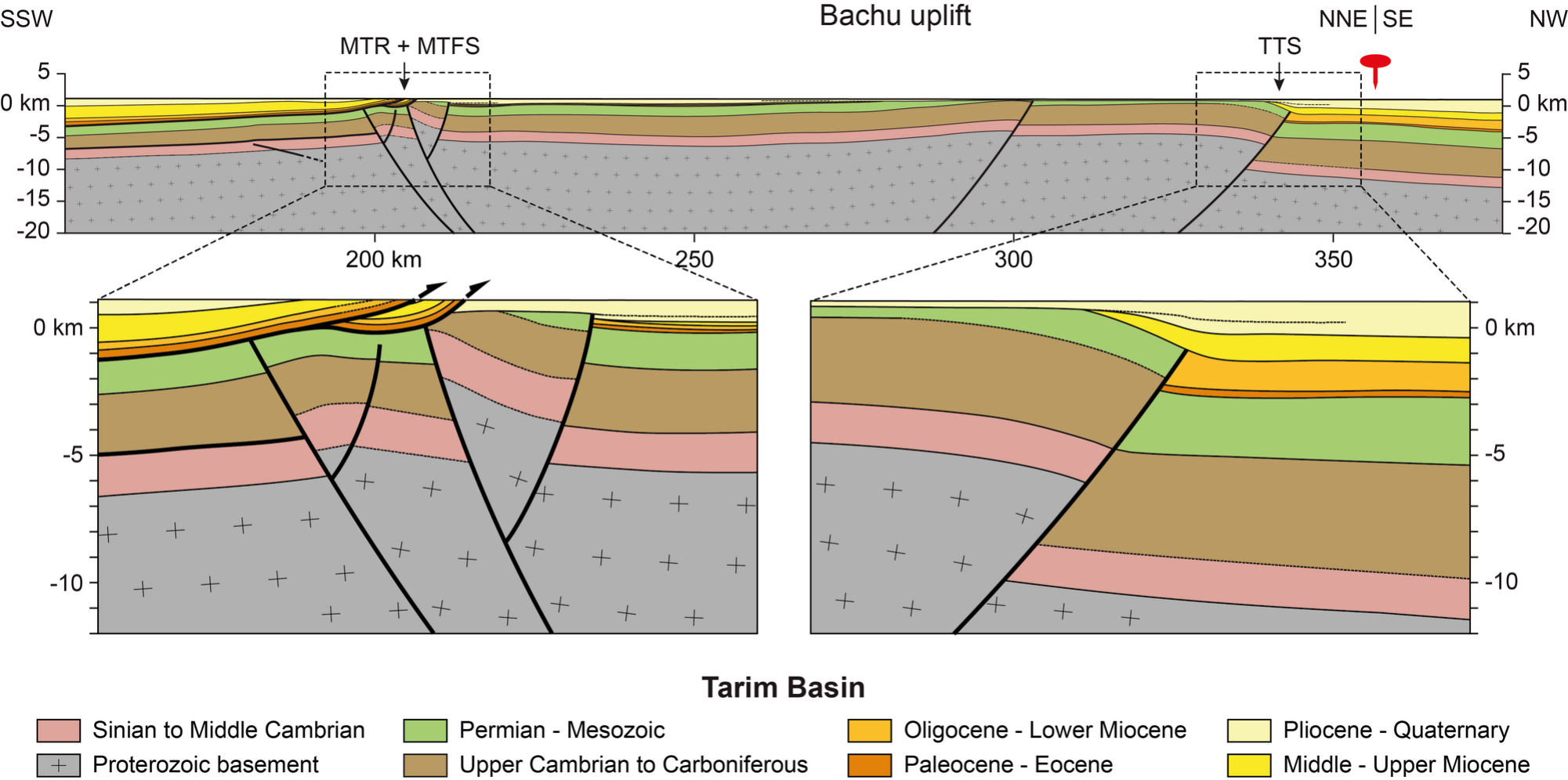
SSW
Bachu uplift
NNE | SE
NW
MTR + MTFS
TTS
5
0 km
-5
-10
-15
-20
200 km
250
300
350
0 km
-5
-10
Tarim Basin
Sinian to Middle Cambrian
Proterozoic basement
Permian - Mesozoic
Upper Cambrian to Carboniferous
Oligocene - Lower Miocene
Paleocene - Eocene
Pliocene - Quaternary
Middle - Upper Miocene

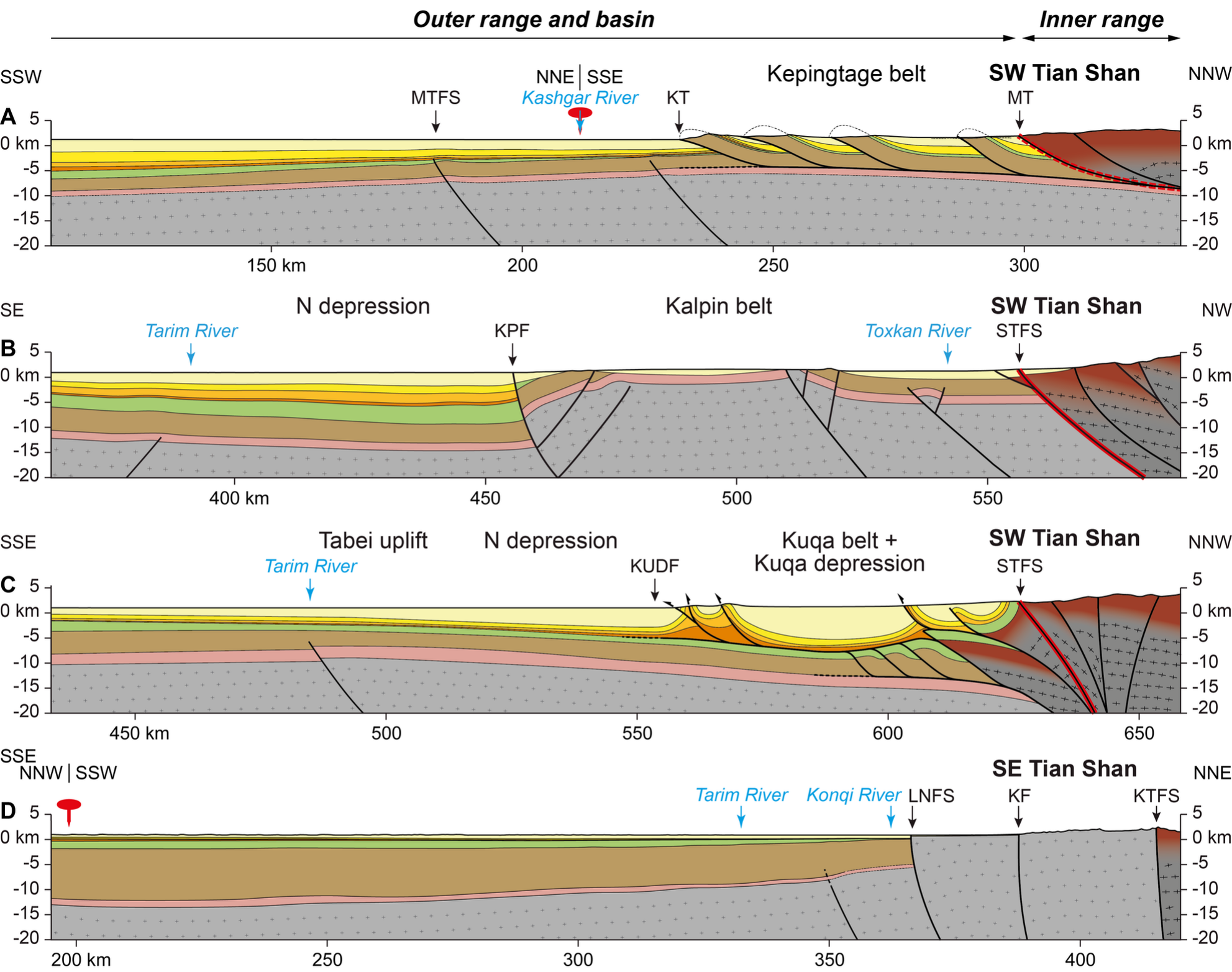
Outer range and basin
Inner range
SSW
NNE | SSE
Kepingtage belt
SW Tian Shan
NNW
MTFS
Kashgar River
KT
MT
A
5
0 km
-5
-10
-15
-20
150 km
200
250
300
SE
N depression
Kalpin belt
SW Tian Shan
NW
Tarim River
KPF
Toxkan River
STFS
B
400 km
450
500
550
SSE
Tabei uplift
N depression
Kuqa belt +
Kuqa depression
SW Tian Shan
NNW
Tarim River
KUDF
STFS
C
450 km
500
550
600
650
SSE
NNW | SSW
SE Tian Shan
NNE
Tarim River
Konqi River
LNFS
KF
KTFS
D
200 km
250
300
350
400
Southern Tian Shan
Proterozoic and Paleozoic basement and sediments
Paleozoic sutures
Tarim Basin
Sinian to Middle Cambrian
Proterozoic basement
Permian - Mesozoic
Upper Cambrian to Carboniferous
Oligocene - Lower Miocene
Paleocene - Eocene
Pliocene - Quaternary
Middle - Upper Miocene

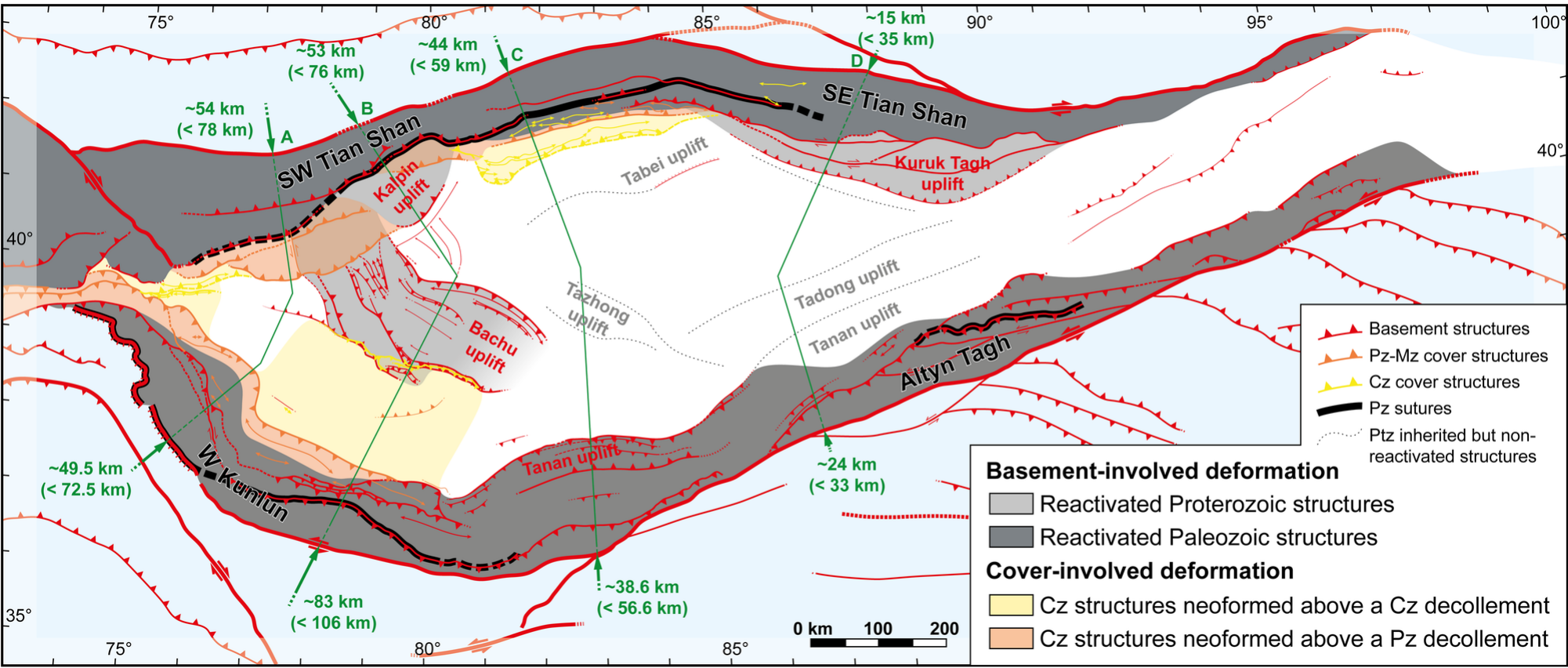
75°
80°
85°
90°
95°
100°
40°
35°
~54 km
(< 78 km)
A
~53 km
(< 76 km)
B
~44 km
(< 59 km)
C
~15 km
(< 35 km)
D
SW Tian Shan
SE Tian Shan
Kalpin
uplift
Tabei uplift
Kuruk Tagh
uplift
Bachu
uplift
Tazhong
uplift
Tadong uplift
Tanan uplift
Altyn Tagh
Tanan uplift
W Kunlun
~49.5 km
(< 72.5 km)
~83 km
(< 106 km)
~38.6 km
(< 56.6 km)
~24 km
(< 33 km)
0 km
100
200
Basement structures
Pz-Mz cover structures
Cz cover structures
Pz sutures
Ptz inherited but non-reactivated structures
Basement-involved deformation
Reactivated Proterozoic structures
Reactivated Paleozoic structures
Cover-involved deformation
Cz structures neoformed above a Cz decollement
Cz structures neoformed above a Pz decollement

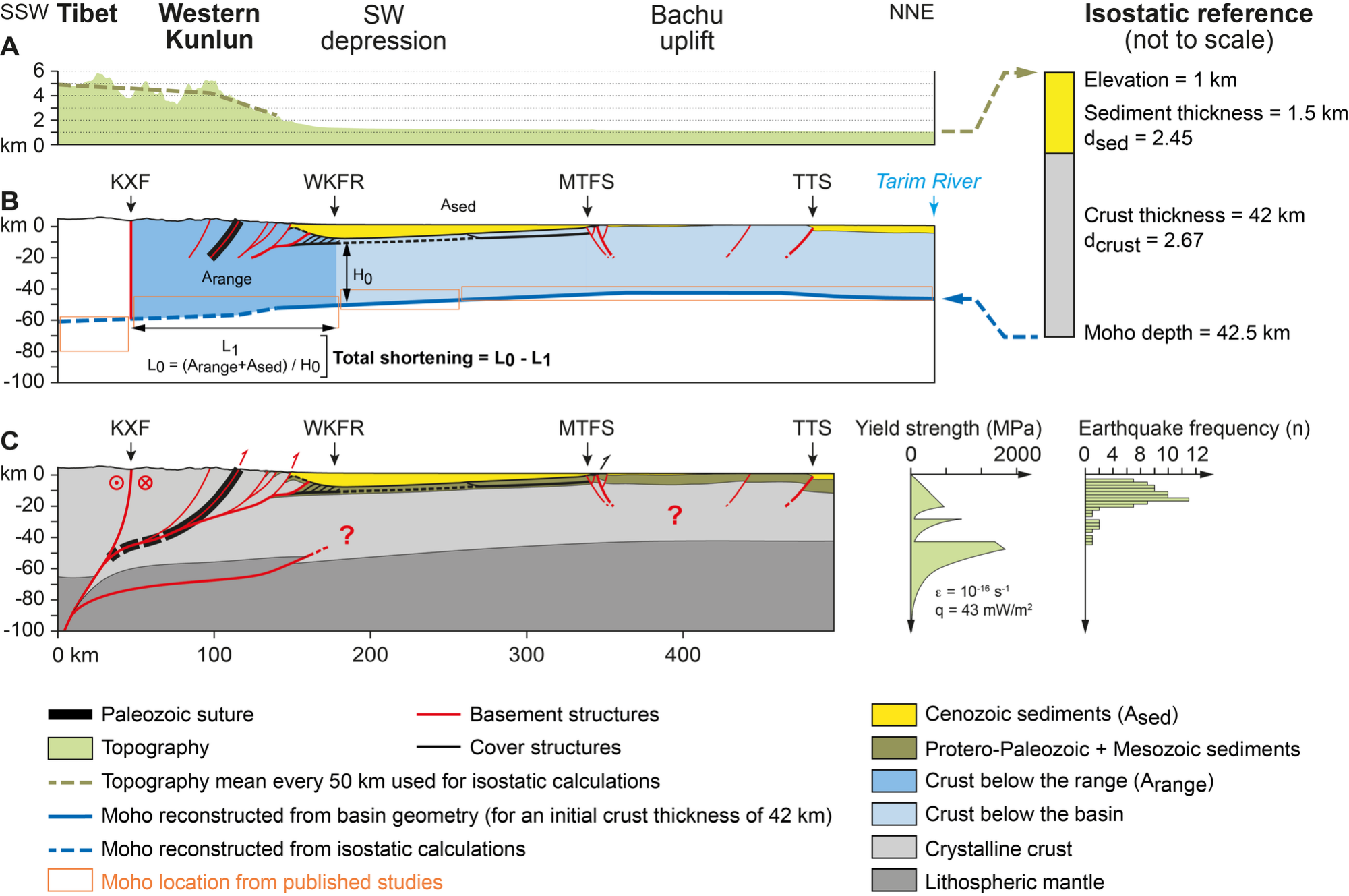
SSW Tibet
Western Kunlun
SW depression
Bachu uplift
NNE
A
6
4
2
km 0
Isostatic reference
(not to scale)
Elevation = 1 km
Sediment thickness = 1.5 km
d_{sed} = 2.45
Crust thickness = 42 km
d_{crust} = 2.67
Moho depth = 42.5 km
B
KXF
WKFR
MTFS
TTS
Tarim River
A_{sed}
A_{range}
H_0
L_1
$L_0 = (A_{range}+A_{sed}) / H_0$
Total shortening = $L_0 - L_1$
km 0
-20
-40
-60
-80
-100
C
KXF
WKFR
MTFS
TTS
Yield strength (MPa)
0
2000
Earthquake frequency (n)
0 4 8 10 12
$\varepsilon = 10^{-16}$ s^{-1}
q = 43 mW/m^2
km 0
-20
-40
-60
-80
-100
0 km
100
200
300
400
Paleozoic suture
Topography
Topography mean every 50 km used for isostatic calculations
Moho reconstructed from basin geometry (for an initial crust thickness of 42 km)
Moho reconstructed from isostatic calculations
Moho location from published studies
Basement structures
Cover structures
Cenozoic sediments (A_{sed})
Protero-Paleozoic + Mesozoic sediments
Crust below the range (A_{range})
Crust below the basin
Crystalline crust
Lithospheric mantle

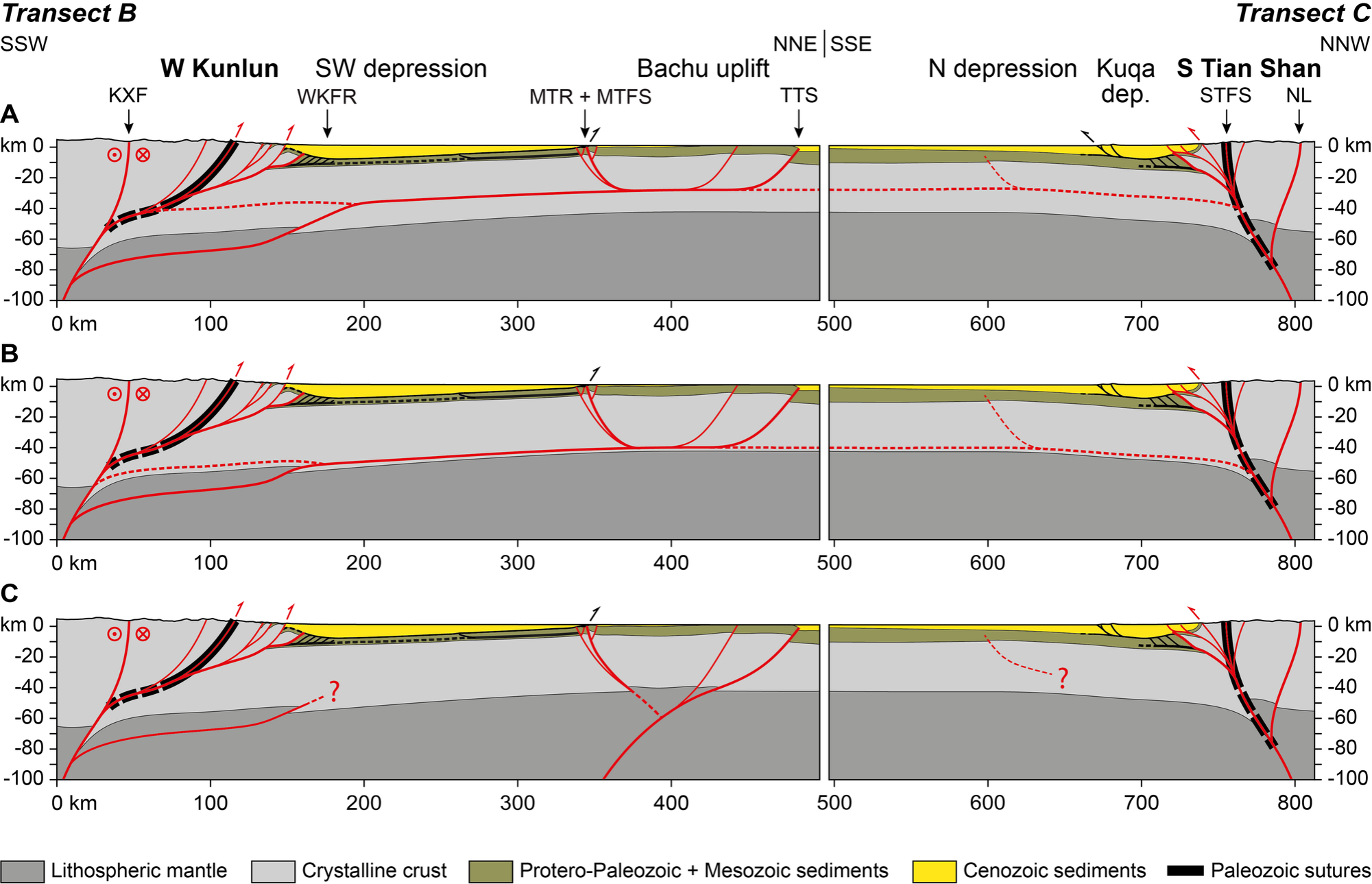
Transect B
Transect C
SSW
NNE
SSE
NNW
W Kunlun
SW depression
Bachu uplift
N depression
Kuqa dep.
S Tian Shan
KXF
WKFR
MTR + MTFS
TTS
STFS
NL
A
B
C
km 0
-20
-40
-60
-80
-100
0 km
100
200
300
400
500
600
700
800
?
Lithospheric mantle
Crystalline crust
Protero-Paleozoic + Mesozoic sediments
Cenozoic sediments
Paleozoic sutures

Range			Shortening (km)				
			1	2	3	4	5
			Entire range (crustal budg.)	Inner range (= 1 - 3)	Outer range (restor.)	Basin (restor.)	Total (= 1 + 4)
N Tibet	W Kunlun	*Transect A (A1)*	49 +23/-17.5	~17.5 +23/-17.5	~31.5 (inh. 9.5 + neo. 22)	~0.5	~49.5 +23/-17.5
		Transect B (B1)	78 ±23	~48 ±23	~30 (inh. 16.5 + neo. 13.5)	~5	~83 ±23
	Altyn Tagh	*Transect C (C1)*	38 ±18	~37.7 ±18	≥ ~0.3 (inh. 0.3+ neo. 0)	≥ ~0.6	~38.6 ±18
		Transect D (D1)	24 ±9	~23.7 ±9	≥ ~0.3 (inh. 0.3+ neo. 0)	0	24 ±9
S Tian Shan	SW Tian Shan	*Transect A (A2)*	54 +24/-18	~18 +24/-18	≥ ~36 (inh. 0+ neo. 36)	0	54 +24/-18
	SW Tian Shan	*Transect B (B2)*	53 ±23	/	≥ ~4 (inh. 4+ neo. 0)	0	53 ±23
	SW Tian Shan	*Transect C (C2)*	44 ±15	~22 ±15	~22 (inh. 19 + neo. 3)	0	44 ±15
	SE Tian Shan	*Transect D (D2)*	15 +20/-15	/	> ~0	0	15 +20/-15